SCALABLE MACHINING OF MICRO-FEATURES FOR ORTHOPEDIC AND TRIBOLOGICAL APPLICATIONS

A Thesis
Presented to
The Academic Faculty

by

Ryan Liu

In Partial Fulfillment
of the Requirements for the Degree
Master of Science in the
School of Mechanical Engineering

Georgia Institute of Technology
May 2016

SCALABLE MACHINING OF MICRO-FEATURES FOR ORTHOPEDIC AND TRIBOLOGICAL APPLICATIONS

Approved by:

Dr. Christopher Saldana, Advisor
Assistant Professor
School of Mechanical Engineering
Georgia Institute of Technology

Dr. Steven Liang
Morris M. Bryan, Jr. Professorship
School of Mechanical Engineering
Georgia Institute of Technology

Dr. Thomas Kurfess
Professor and HUSCO/Ramirez Distinguished Chair
School of Mechanical Engineering
Georgia Institute of Technology

To Professor Dennis Lieu

who took a chance on a Freshman and shared his love for research

ACKNOWLEDGEMENTS

LIST OF TABLES

LIST OF FIGURES

ABSTRACT

Micro-scale surface textures have found profound application in various industrial sectors, including the biomedical and tribological communities. While numerous manufacturing methods are available for the fabrication of these micro-features, advancements in high-precision machinery and piezoelectric actuation have allowed for the development of new and scalable processes for mechanical surface texturing based on modulation-assisted machining. The present study aims to understand the effects of micro-scale surface textures produced by modulation-assisted machining on surface performance in biomedical and tribological configurations. To accomplish this, a predictive geometric model was developed to simulate surfaces generated in multiple mechanical texturing orientations. Experimental studies were carried out to generate controlled surface textures over a range of characteristics in terms of feature size and morphology. The surface performance of the resulting textures in a biomedical implant application were tested for osseointegration capability with *in vivo* and *in vitro* tests. For these tests, a bilateral rat tibia model and precursor osteoblast MC3T3-E1 cell culture were used, respectively. Surface performance of the micro-scale surface textures in a tribological application was evaluated using a pin-on-disk wear testing configuration. The results of both studies show promising findings that demonstrate the beneficial effects of surface textures produced by modulation-assisted machining.

CHAPTER 1

INTRODUCTION

High precision control of manufactured surfaces has gained tremendous interest in recent years. The fabrication of precise, micro-scale surface features has been enabled in niche applications over the past several decades with technologies such as micro-electrical discharge and laser machining, and today there is a continually increasing need for the manufacture of precise micro-features for performance system designs. These precise micro-features – or surface textures – have found widespread applications in areas such as micro fluidics, medical components, and frictional interfaces [1-5]. Textures often allow for ultra-precise surface geometries and increased surface areas that are leveraged for their applications. In the field of orthopedic implants, implant loosening is a primary cause for revision surgeries and total implant failure [6-9]. Textured surfaces can increase the wettability of implanted materials, which encourages biological fluid contact with implant surfaces and allows for additional mechanical interlocking due to increased bone in-growth [3, 10-12], In severe tribological applications, textures can act as lubricant retention cavities that decrease friction forces and reduces heat generation at sliding interfaces [1, 13-18]. This is of particular interest in the automotive industry, where percentage point increases in engine efficiency can translate to large decreases in greenhouse gas generation worldwide. Applications of surface textures in these disciplines are a prime focus of the present study.

While manufacturing methods such as laser surface texturing [19, 20], chemical etching [21], and sintering [22-24] have been established as effective means of creating highly controlled surface modifications, high upfront capital costs and inability to scale

1

the processes have limited their potential applications [25]. In the context of orthopedic implant development, grit blasting has been established as a scalable method of surface modification [3, 26-31], however these blasting techniques are secondary processes that require implants to be removed from the primary processing machine for batch-mode processing. This limits the potential process efficiency. Additionally, the process cannot independently control microstructure and topography of the final surfaces, which limits the level of optimization achievable for bone integration.

The present study establishes modulation-assisted texturing (MAT) as a controllable manufacturing method that may serve as an alternative to the existing texturing technologies when scalability and economics are a concern. The modulation-based process has been shown to produce micron-scale surface features without the need for secondary machinery. Furthermore, the modulation-created textures in this study are shown to have beneficial effects on wear and frictional properties of materials. While the successful manufacturing of these surfaces have broad applicability in the service performance of load-bearing members such as power transmission and bearing systems, this present study investigates application of textures in studies of wear and frictional interfaces under conformal contact. The study also investigates the applications of MAT-created surface textures in bone implant development by evaluating the *in vitro* and *in vivo* bone integration of textured samples when compared to controls. This integrated study creates the framework necessary to create higher fidelity simulations and experiments in the future, as well as optimization of surface feature design.

1.1 Problem statement

The capability of MAT for surface texturing in tribological and orthopedic systems applications and its corresponding effects on surface performance in these domains are

not well understood. The purpose of the present study is to establish MAT as a predictable manufacturing process for generation of controllable micro-scale surface features. The present study evaluates: (1) the applicability of MAT as an in-line manufacturing method to enhance implant-bone integration and (2) the effects of MAT on frictional and wear properties of interfaces under conformal contact.

1.2 Thesis organization

This thesis document is organized into the following sections: introduction, background, experimental and simulation methods, results and discussion, and conclusion. The validity of the MAT process is established by first incorporating a theoretical framework into a computer simulation for visualization and prediction of the surface features. The simulation is then compared to physical experiments to show the applicability of the simulation in predicting surface geometries and demonstrates the conformity of manufactured surface textures. MAT is then used to create samples for bone implants tested using *in vitro* and *in vivo* protocols to evaluate bone-implant integration. The MAT process is also used to texture samples for pin-on-disk friction and wear testing to evaluate tribological properties. Chapter 2 provides a brief review of existing surface texturing methods and their applications in increasing implant-bone integration and improving tribological properties. MAT methods are introduced and the governing equations are provided. Chapter 3 provides the experimental and simulation configurations. Chapter 4 provides the results and accompanying discussion of each experiment. Finally, Chapter 5 presents key findings from the thesis and proposes recommendations for future studies.

CHAPTER 2

BACKGROUND

Continuing research in micro-manufacturing processing has spurred associated improvements in terms of tooling, process time, and dimensional accuracy. Key industrial processes that have been used to create these micro-features are provided in the review below, with particular emphasis placed on mechanical material removal processes. This chapter provides a brief overview of these micro-texturing methods currently available and focuses on texturing of metal surfaces for industrial applications.

2.1 Surface texturing methods

Manufacturing of surface micro-textures can be categorized into four main groups: chemical-based, energy-based, deposition-based, and mechanical-based methods for fabrication. This section is organized into these four large groups and emphasizes a process called modulation-assisted texturing (MAT). This surface texturing method leverages advances in actuator and high-precision machinery to modernize traditional, mechanical manufacturing processes. While each texture manufacturing method has unique advantages and disadvantages, MAT serves as an inexpensive and scalable alternative to existing technologies while simultaneously offering high levels of micro-scale feature accuracy.

Advancements in the semiconductor and microelectromechanical systems (MEMS) industries have led to the development and refinement of a number of chemical-based microfabrication techniques. Microfabrication methods are used to manufacture mechanical and electrical devices that are used in a variety of applications such as sensors

and displays. These techniques use chemical and electrical means categorized by rapid parallel processing and can include deposition (i.e. chemical vapor deposition, physical vapor deposition), patterning (photolithography), and etching among other techniques [21]. These microfabrication techniques can achieve components with nanometer and micrometer feature sizes and have been shown to be useful in the miniaturization of micro-devices such as in the fields of integrated circuits, optical devices, and nano-sensors; but disadvantages exist and vary from process to process and include relatively high capital investment, material limitations, and geometric scalability issues [25].

Energy-based surface modification methods, including laser surface and electron beam texturing, have found applications in the manufacturing of components such as micro-hydrodynamic bearings and mechanical seals, and have shown the ability to controllably create surface micro-depressions of diameter 150 μm with depths of about 8-10 μm [19, 20]. A primary advantage of these processes is that they do not require physical masks (as in grit blasting) and are far more controllable in terms of final texture morphology. The process has shown close conformance with analytical models, but suffers from issues inherent to the manufacturing process, including heat affected zones that adversely influence surficial material properties, poor vertical control of feature geometry and large investments in equipment and machining environments [32].

In addition to chemical and energy-based means for creating surface textures, deposition techniques also have been used to controllably add material to the surface of workpieces. In powder metallurgy, metallic powder is locally compacted and sintered or thermally sprayed to coat external surfaces. Compaction and subsequent sintering allows for the formation of surface textures on difficult or impossible to machine workpieces, and often allows for cost savings due to conservation of raw materials [24]. Sintering

5

temperatures do not need to reach material melting temperatures and instead rely on the diffusion of atoms to create bonds. Further, because temperature and cooling rates may be moderated during the powder metallurgy process, this allows for a degree of design and control of material grain size and uniformity (and therefore material properties) that often does not exist in alternative processes. The accuracy and precision of the process are largely determined by the metallic powder size, which can be as small as 5 microns [23]. In thermal spray processing, molten material is sprayed onto the surface of a material. A limited degree of control is possible in thermal spraying through the use of a physical mask. Further, overall coating thickness, surface porosity, and surface roughness are controllable by adjustment of the spray parameters [22].

Mechanical micro-texturing methods involve the application of deformation and/or material removal to controllably impart features on work material surfaces. These processes have inherent advantages over alternative methods in terms of scalability, as the associated manufacturing costs generally do not scale with the quantity of features produced, as well as relatively lower initial start-up costs. Traditionally, bulk deformation (e.g., forming, extrusion) processes have had limited capability to create controlled micro-scale surface features [24], however recent advances have led to increases in micro-scale precision and topography control. The mechanical process of knurling has been shown to be an effective method of texturing large (m^2) areas by deforming surfaces and causing materials to flow into the recesses of knurling tools and have typically been used for the macroscopic texturing of frictional interfaces for non-slip components (i.e. handgrips) or low-precision components (i.e. press fitting metal and plastic parts) [33]. In the micro-feature community, knurling has been limited by its lack of adaptability to workpiece contours and its relatively larger feature sizes: the smallest commercially

6

available tools with 80 TPI yield textures of approximately 450 μm in length [34]. Innovation in knurling has allowed for the miniaturization of the surface features, reaching minimum feature sizes with dimensions in the hundreds of microns [35, 36], however minimum feature sizes remain larger than about 100 μm [37]. In addition to knurling's relatively larger feature size compared to many of the aforementioned fabrication processes, knurling also suffers from the lack of uniformity of fabricated micro-textures, with micro-knurled features differing from expected feature sizes by about 10%, which increases with increasing tool wear [38, 39]. Relative to other fabrication processes, knurling has also been found to induce surface stress concentrations that require subsequent processing prior to functional use [40]. Advances in micro-mold manufacturing tools and equipment spurred the development of processes such as micro-powder injection molding and micro-hot embossing, both capable of achieving precision-scale manufacturing tolerances and address the size and controllability limitations of knurling [41, 42]. Advances in micro-mold manufacturing tools and equipment spurred the development of processes such as micro-powder injection molding and micro-hot embossing, both capable of achieving precision-scale manufacturing tolerances [41, 42]. Micro-scale indenters, for instance, have been shown to be capable of producing feature dimensions in the range of 10 μm and thicknesses of 25 μm, as well as dimensional tolerances better than 0.5% of these characteristic feature sizes [43]. Micro-scale indentation tools have also been used to create pits on the sub-micron scale [44], but these generally require equipment and tools atypical of standard machine shops to reach these levels [45]. The dimensional accuracy of micro-indentation is also reliant on input material homogeneity at much higher levels than the other processes previously discussed [47]. Surface topography also can be controlled using

abrasive grit-blasting methods, primarily to control surface finish and burr formation. In this process, air blast systems or centrifugal blast wheels accelerate shot media to impact work material surfaces. The individual impacts cause mechanical deformation at the surface, resulting in both localized compressive stresses and the creation of quasi-spherical surficial dimples. While not a deterministic process, masks may be used to direct media and treatment to specific areas of the work surface. For the deformations created, sand blasting has been shown to generate overlapping surficial dimples in both cast iron [48] and silicon carbide [49] with diameters ranging from 40 to 120 µm (depending on media and mask used), and 2 to 10 µm in depth. Modeling of sand blast dynamics can be extrapolated from studies of shot peening, with representative models of single shot impacts [50, 51] and multi-shot impacts [52].

For mechanical micro-texturing based methods, precision metal cutting processes also offer inherent scalability for control of surface topography [53, 54]. Material removal in machining generally occurs by concentrated shear when a single- or multiple-point cutting tool enters a material and shears metal chips from the surface of the workpiece. Controllable machining parameters of cutting speed, feed, and depth of cut determine the subsequent material geometry and surface finish. Scaling down of the cutting process in the micron-size regime has been realized in micro-milling and micro-drilling applications which can be used to produce features in the 1 to 500 µm characteristic size range [55]. For example, micro-milling has been used in the creation of micron-scale grooves, cavities, and 3D geometries which have found applications in the optics, micro-fluidics, and consumer electronics industries [1-5]. Masuzawa offers an excellent review of key technologies and inherent limitations of state-of-the-art micromachining processes [55].

8

The present study expands on the use of machining-based processing to control surface topography through the use of a specialized electromechanical device for facilitating fine-scale motion control of cutting tools. Modulation-assisted machining (MAM), also referred to as vibration or oscillatory machining, refers to a class of processes wherein tool motion is directly controlled by an external actuator (e.g., piezoelectric, magnetostrictive, cam-driven). MAM is capable of facilitating a number of enhancements including deterministic chip control, enhanced tool-workpiece interfacial lubrication, reductions in tool wear, enhanced material removal rates [56, 57]. The origin of MAM for surface topography control, henceforth referred to as modulation-assisted texturing (MAT) in the present study, dates to an early paper in 1984 that theorized of the ability to machine or indent workpieces with oscillating micro-features [58]. In 1995, a specialized cutting system driven by a piezoelectric actuator was used to demonstrate manufacture of discrete surface features that qualitatively matched theoretical geometries [59]. Greco et al. improved this model to allow for increased controllability of surface textures on concave, convex, and flat surfaces. He used a fast-tool servo system to create textures of depth 2-50 µm and 100-550 µm diameter with errors of 11% for aluminum and 90% for hardened steel [60]. Kurniawan et al. [61] found similar results using a piezoelectric actuator with texture depth errors of 10.1% and 48.0% for aluminum and mild steel, respectively. An excellent review provided by Brehl et al. outlines key developments in the use of these technologies [62]. The multitude of studies to-date show the relative controllability of surface textures produced by this method, but also showcase the processes limitations that necessitate continued development.

2.2 Surface texture applications

The controlled surface texturing of engineering materials has found applications in areas such as microfluidics, medical components, and frictional interfaces [1-5]. The ensuing sections review use of micro-textured samples in orthopedic and tribological applications.

2.2.1 Orthopedic performance effects

The significant growth seen in the biomedical implant sector over the previous few decades has led to the proliferation of novel implant materials, designs, and surface coatings with the overall goal of implantation success and overall patient health and satisfaction [63, 64]. Osseointegration refers to the "direct bone-to-implant interface without interposition of non-bone tissue" as first introduced by Branemark in his early longitudinal dental implant paper [65]. After the localized trauma caused during incorporation of implants, osseointegration involves osteoclasts, which are recruited to the bone surface for resorbing of micro-damaged bone tissue. Osteoblasts then deposit new bone tissue to repair damaged tissue and also to optimize bone loading for the new mechanical environment. A number of excellent literature reviews exist that cover literature within dental implant systems [66], surface topography effects on osseointegration [3], and the functional assessments of osseointegration [2]. These reviews provide a more thorough understanding of the current research regarding bone implant surface modifications and supplements the discussion below. The successful osseointegration of implants is dependent on various parameters such as surface textures, roughness, and wettability. This section reviews the effects of these key parameters on overall implant success and focuses more thoroughly on the literature of implant surface pore design. The extensive literature on the osseointegration of various pore geometries

and the design trends that can be extrapolated from the studies are used to inform the implant designs used in the present study.

Structural integrity of implant fixations is strongly related to the ability to resist the compressive, shear, and tensile forces seen at bone-implant interfaces. Mechanical interlocking of bone tissue into the surface of the implant on microscopic and macroscopic scales can be used to stabilize implants and resist pull-out forces. Many groups have aimed to increase mechanical interlocking by the addition of surface textures [3, 10-12], and have been modeled by Hansson et al. to describe functional relationships between textures and interfacial stresses [67]. While it has been shown that the addition of surface textures increases the bone-implant contact area, which increases the torque needed for removal [68], it has also been shown that increased implant surface area does not always stabilize the implant [69]. Further, increases in surface area have been shown to increase levels of material leaching from implanted surfaces into the body [70], although this finding has proven insignificant with studies showing oxide layer stability in titanium [6, 71].

Control of surface roughness, on the other hand, has been proven as an effective method of adhering osteoblasts and osteosarcoma cells [26], however the precise effects of roughness on osseointegration has shown to vary among studies. Sandblasting to a surface roughness of 1.5 µm Ra for instance has been shown to outperform Ra values of 1 µm and 2.2 µm [27], but Boyan et al. shows that an Ra value of 3-7 µm outperforms roughness values of less than 1 µm Ra [28]. While these studies have found promising osseointegration results in the 1-7 µm range, a number of studies have found that roughness above about 5 µm may increase the rates of peri-implantitis, which often causes issues with implant stabilization in the future [72, 73]. Regardless of the ideal

macro-scale roughness, a number of research groups have investigated the effects of nanoscale surface roughness on osteoblast differentiation and proliferation and showed that nanoscale roughness could be leveraged to have additive effects when conjoined with macro-scale roughness [3, 29-31].

Increasing surface energy has been shown to enhance key osseointegration factors such as cell adhesion, proliferation, and differentiation [74]. Surface energy quantifies the amount of disrupted intermolecular bonds of a material. In the context of metals, increased grain boundary quantity and mis-orientation angles increase the material's surface energy, which in turn increases its wettability and hydrophilic nature (surface energy, wettability, and hydrophilicity are used interchangeably in the literature). Although the optimal levels of wettability remain unclear, most studies have found that increased surface energy increases the levels of material osseointegration when compared to surfaces characterized with low surface energy [74, 75]; however, increases in surface energy have also been linked to the proliferation of macrophages on implant surfaces, which increases bone re-absorption [76]. These trends are detailed in a comprehensive review on implant surface energy, which shows the recent studies that primarily evidence the positive effects of increased surface energy on implant integration [77].

A large number of surface topography manufacturing methods and designs have been used in the manufacturing of orthopedic implants, including laser texturing [78], abrasive blasting [79], etching [80, 81], micro-machining [35, 82-85], and electro-discharge machining [86-88]. Jemat et al. [89] and Vologin et al. [79] surveyed the aforementioned methods of modifying dental implants surfaces, as well as plasma-based coating, anodizing, and SLA/SLS.

Of particular interest in the context of this prior research are the effects of pores on osseointegration. Semi-spherical recesses, typically created by etching, have been shown to increase implant success, however also serve as a controlled variable that informs ideal feature depths, densities, and cross-sectional area. Though one comprehensive study that spans all practical pore sizes was not found, a number of studies suggest that semispherical pores of about 200 μm in diameter allowed for the highest levels of osseointegration as measured by peri-implant bone volume and density when compared to pores that range from about 50 to 300 μm [90-92]. This finding is supported by recent studies that showed optimal pore sizes for maximum bone ingrowth to be between 100 – 400 μm in diameter [93, 94]. These studies also determined a minimum pore size of 50 μm to prevent the ingrowth of fibrous tissue. It has been found, however, that while larger pores improve the speed and depth of mineralized tissues, the large geometries may impair mechanical properties [95], which naturally leads to an evaluation of smaller-scale pore sizes. Perez et al. summarizes the differences in physiological responses to macro-scale pores (pores>50 μm) and micro-scale pores (pores<50 μm): while macro-pores determine vascular bone growth, micro-pores more heavily influence cell adhesion prior to bone growth [96] and have also shown beneficial osseointegration results [67, 97]. Both pore sizes affect overall implant integration, but studies have suggested that macro-pore sizes have larger effects on overall implant success when compared to the results of micro-pores [80, 98]. In this regard, it has been found that the pore sizes recommended from the literature are on par with the geometries that are machinable via MAT. Further, surface texturing by MAT was postulated to be well-applicable to surface topography control of a ball and socket hip joint [99], which validates the use of MAT as an implant texturing method.

Because MAT surface textures have not been directly evaluated in previous studies, texture design parameters were extrapolated from the analogous studies detailed above. While these studies often gave conflicting evidence (i.e. differences in optimal pore size), the sheer volume of literature helps inform texture design. A number of studies evaluated ideal pore diameters manufactured through processes such as laser etching or grit blasting. The studies found that diameters between 50 – 300 μm allowed for maximum bone ingrowth by being large enough to encourage complete bone matrix mineralization and to prevent bridging, while being small enough to discourage un-mineralized bone to partially fill pores [80, 93, 94, 98, 100]. While MAT surface textures do not have discrete surface pores, it is theorized that a continuous groove may follow the same design parameters, and that groove width should be limited to the same 50 – 300 μm range. Target surface roughness measurements of 1 – 3 μm Ra were established, as they have been found to increase osseointegration factors [26-28]. This is accomplished by removing as much of the mirror-finished material surface. This process may also play a role in increasing material surface energy, which has been shown to encourage healing [79] and discourages bone reabsorption [76]. Finally, the quantity of features on the material surface was maximized to increase mechanical interlocking [67]. Simultaneously, these design parameters must be balanced with physical manufacturing limitations, such as power-amplifier roll-off behavior, practical tool geometries, and burr formation.

2.2.2 Tribological performance effects

The improvement of frictional and wear properties of sliding interfaces can reduce energy lost due to friction and can increase the longevity of components for performance systems involving moving parts (i.e. aerospace, automotive, energy) [101-104]. Many

variables influence the friction and wear properties of interfaces and, for a constant surface and lubricant, performance is largely determined by characteristics of lubrication such as layer thickness. The lubrication layer thickness is directly affected by normal force and sliding speed. Excessively low sliding speeds cause lubricants to fail to adequately separate sliding materials, whereas excessively high speeds lead to energy losses due to hydrodynamic friction. This balance is further influenced by normal forces at the surface, with higher normal forces generally leading to faster sliding speeds needed for minimal frictional response. The regime corresponding to minimum frictional forces and superior wear performance is referred to as elasto-hydrodynamic lubrication [102]. Much research has been devoted to both theoretical and empirical determination of the elasto-hydrodynamic lubrication regime for material, surface topography, lubrication, load, and speed combinations [105-111]. Among these, the effects of controlled surface topography on frictional and wear properties of materials are most relevant.

Recent studies have found that the presence of micro-scale surface features can enhance the frictional and wear performance of sliding interfaces. Micro-scale surface textures can serve as lubrication reservoirs as well as can collect wear debris that causes undesirable galling and surface-related material deformations [1, 13-18]. Shen et al. provides a numerical optimization method for converging on texture shape and shows that optimization can reduce frictional forces by 65-80% (dependent on lubrication regime) [112]. In spite of the findings, Hsu et al. brings to attention that though benefits have been seen by these previous groups, a comprehensive understanding of the underlying science of surface feature design had not been systematically studied, in terms of the effects of texture size, shape, pitch, and pattern on hydrodynamic lubrication regimes [113].

15

A number of studies have investigated the ability for various texturing methods to enhance surface tribological performance. One method is to use lithography and electrochemical etching to create 'undulated surfaces,' which have been shown to continually remove oxide debris from frictional surfaces and decrease metallic friction and wear [114-116]. Pellet pressing has also been used to generate textures on steel surfaces with reduced friction coefficients and wear rates due to increased localized hydrodynamic pressure and corresponding lubricant load-carrying capacity [48]. Further, wear debris was once again found to exit the contact region and be retained within the surface textures, this also contributing to enhanced wear performance. Many groups have investigated the use of laser surface texturing (LST) as a means of creating surface contours that improve tribological performance. Wang et al. finds that surface pores of diameter 150 µm and depth of 8-10 µm increases the critical load that marks the transition between the hydrodynamic and mixed lubrication regimes by about 20%. This increase in load translates to a wider hydrodynamic lubrication region with low coefficient of friction, and higher load carrying capacity [117]. This was confirmed by Borghi et al. in studies of textured and untextured nitrided steel for engine performance measured by a pin-on-disk tribometer [13]. For hydrodynamic, mixed, and boundary lubrication regimes with circular textures, micro-scale texturing has been linked to reduced friction (~75%), and an extended hydrodynamic regime on the Stribeck curve. Analogous dry (unlubricated) tests, however, only showed a decrease in friction of about 10% compared to the untextured state. A number of groups have discussed the effects LST has on lubrication regimes [32, 49], and Etsion et al. also provided an excellent review of the tribological modeling efforts and empirical results of LST and a number of other surface texturing methods [19].

The tribological properties of MAT surface textures were first evaluated in 1984 by Schneider [58]. The study used a modulating, rolling indenter to texture surfaces for improved wear resistance, contact stiffness, and hydrodynamic sealing. In a study that is revisited in 1997 [118], Schneider showed increased wear resistance of 1.5-4 times for piston rings, sliding sleeves, twisting rings, and blade guideways. He found static and dynamic friction coefficients decrease by 20-25%, which is on par with findings with LST surfaces. Most impressively, he provided long duration observations of a vibration-textured guide and revealed an absence of scratching, scoring, or seizing on the textured surfaces. Levitin et al. used a similar modulation-assisted surface texturing system to find not only extended frictional paths prior to seizing, but also decreases of wear volume by about 85% [119]. When implemented on a ball and socket joint, the surface textures corresponded to decreases in frictional torque of 25-35% [99]. These promising results led to the continued development of modulation-created textures for frictional interfaces under Greco et al. with the so-called 'vibromechanical texturing' process. This process for fabricating textures of diameter 100-550 μm and depth 2-50 μm on flat, outer cylinder, and inner cylinder surfaces, was developed, and the group theorized that such textures could have profound effects on tribological performance [60, 120]. Textures of size 100 μm x 100 μm and 240 μm x 100 μm underwent rolling contact fatigue performance testing in the elasto-hydrodynamic lubrication regime, and exhibited decreased fatigue life of the material by 50 and 80% for the two texture sizes, respectively. Though the preliminary results were not promising, a second set of textures at shallower depth (15 μm) were tested by Ghandi et al. [121] in both brass 360 and Al6061-T6, showing reductions in wear tracks by about 30%.

Based on the studies of Greco et al. and Ghandi et al. [60, 120, 121], machined texture depths around 15 μm have shown positive results, however a full understanding of texture depth and its effects on lubrication regime has not been accomplished. In the present study, pin-on-disk tribological tests were performed to evaluate the effects of surface texture depth on the coefficient of dynamic friction and wear track depth. Based on the test results, a Stribeck curve was established to compare the various textured surfaces with an untextured control surface.

2.3 Modulation-assisted texturing

Modulation-assisted machining (MAM) describes a class of manufacturing processes wherein controlled modulation is superposed onto the standard linear movement of conventional tooling. This superposition has been implemented in a number of machining operations including turning [122, 123], milling [124, 125], grinding [53] and drilling [56, 126]. Modulation can be applied along a single axis, two axes (elliptical vibration) [127, 128] or three axes [129]. For modulation aligned in a single direction, the orientations can be applied in the direction of the cutting velocity (e.g., velocity-direction) or in the direction of the cutting feed (e.g., feed-direction), as shown in Figure 1 [130, 131]. For machining processes occurring at industrial conditions, the latter of these two orientations is of greater interest as the required modulation capabilities (e.g., frequency and amplitude) required for separating the tool from the workpiece are decoupled from machining speed and coupled to machining feed, simplifying the required motion platforms.
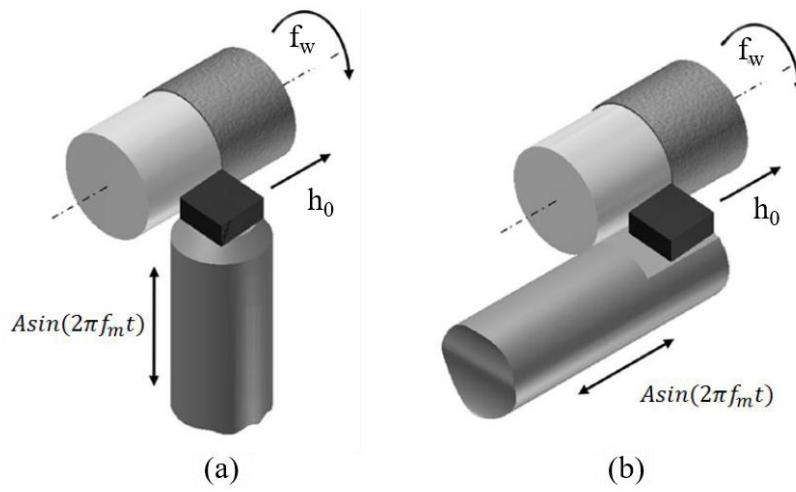
Figure 1: MAM turning configurations in (a) velocity direction and (b) feed direction

Modulation-assisted texturing (MAT) refers to use of MAM in controlled surface texturing configurations. Feed-direction MAT can be classified into that occurring in a plunging orientation or a sliding orientation. Mann et al. provided the fundamental equations of tool motion and derived spatial length approximations for the engagement of the cutting tool with the workpiece surface [57] and found that regions of discrete (interrupted) cutting could be determined by consideration of the relationships between machining conditions (e.g., feed, spindle frequency) and modulation conditions (e.g., modulation amplitude, modulation frequency) [130]. This model was experimentally validated in terms of the resulting chip morphologies [56, 132]. Suzuki et al. modeled the dynamic forces seen at the tool due to the interactions and also confirmed the phase calculations provided in the previous studies [133]. In addition to models for describing material response, the effects of the controllable parameters on surface topography have been introduced in previous works. For example, surface characteristics including inter-

texture distance and texture density have been related to modulation parameters [60, 134]. Further models used to describe surfaces produced by elliptical MAT can be used to describe the resulting surface in single-direction MAT, as in Ref. [135].

In comparison to that regarding plunging-type MAT configurations, the extant literature pertaining to modeling and implementation of sliding-type MAT is somewhat sparser. Schneider first proposed an analogous process in 1984 and referred to this as process as 'vibro-rolling', but did not implement analytical models mathematically to describe the surface state in this process [58]. This process was revisited by Bulatov et al. in 1997 in a study of tribological performance parameters and states a relationship between tool modulation frequency and texture morphology [118], but once again did not publish a predictive model for texture creation. A numerical model to describe the surface state in sliding-type MAT was provided by Mann et al. in 2013 [136] and Gandhi et al. in 2015 [137]. In this regard, the equations of motion were used to simulate the toolpath in a turning-type configuration and were incorporated into a geometric model that evaluates the effects of modulation phase angle on the resulting texture morphology.

In this study, plunging-type and sliding-type MAT operations (e.g., feed-direction modulation configurations) are considered. This section provides equations of motion for cutting tools that are used to calculate the expected geometric dimensions of the resulting surface textures under ideal cutting conditions. These models assume pure geometric subtraction of material and do not consider complications such as elastic/inelastic deformation, chatter, tool wear, and burr formation inherent to real-world processes. Terminology are provided in Table 1 for the plunging- and sliding-type MAT operations.

Table 1: MAM variables and definitions

	Symbol	Definition	Units
Input Variables	A	Amplitude	μm
	λ	Modulation wavelength	μm
	Δ	Modulation axis offset from material surface	μm
	f_m	Modulation frequency	Hz
	f_w	Workpiece rotation frequency	revs/s
	h_0	Feed	mm/rev
	a_p	Depth of cut	μm
Workpiece Dimensions	R	Nominal radius	mm
Positions	θ	Angle of workpiece rotation	Radians
	r	Radial position	mm
	x	Circumferential position	μm
	y	Normal position	μm
Outputs	L_d	Texture length	μm
	L_c	Distance between textures	μm
	D	Texture depth	μm
	w	Texture width	μm
	L_s	Sliding texture length	μm
	φ	Phase shift	Radians

2.3.1 Plunging-type MAT configurations

Two plunging-type MAT configurations – outer diameter plunging and face plunging – are mathematically modeled in this section. The resulting nature of the material removal behavior for both processes result in the formation of discrete surface features, however, the toolpaths for each are unique. The kinematic equations of motion are provided for the toolpaths and key geometric measurements are derived for both of the plunging-type MAT configurations.

Outer diameter plunging-type MAT configurations

A schematic of the outer diameter, plunging-type MAT is provided in Figure 2. In this orientation, an oscillating tool with amplitude A and frequency f_m feeds axially towards the untextured end of the workpiece at feed h_0, similar to a standard turning operation. While feed remains constant, depth-of-cut (a_p) continually changes as the tool enters and exits the workpiece. Because modulation occurs in a direction normal to the surface velocity, the cutting speed does not determine the required amplitude needed to separate the tool from the workpiece. The tool's tip shape determines the cross sectional profile (and area) of textures. The length of textures is determined by the surface speed (which is a function of radial position (r), modulation frequency (f_m), and spindle frequency (f_w), and the texture depth is determined by the modulation amplitude (A) and modulation axis offset (Δ). The cutting tip location modulates sinusoidally and can be described with A, Δ, and spatial wavelength λ. λ is a function of f_m and f_w, and is defined in Equation (1). Figure 3 shows a 2D representation of the outer-diameter, plunging-type MAT process. In this schematic, a tool modulates vertically, while the work moves from right to left.

$$\lambda = 2\pi R(f_w/f_m) \tag{1}$$
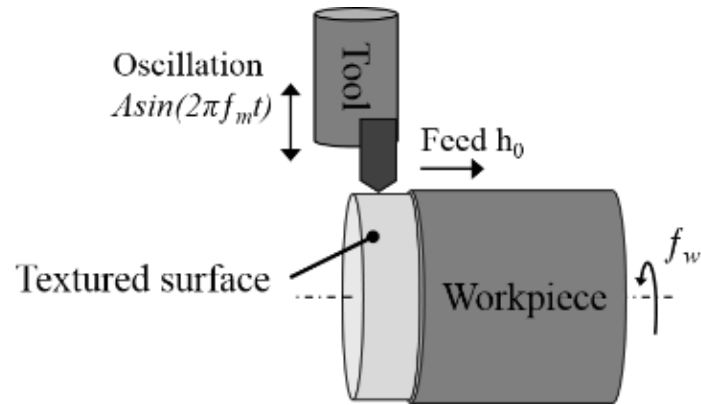
Figure 2: Outer diameter plunging-type MAT configuration schematic
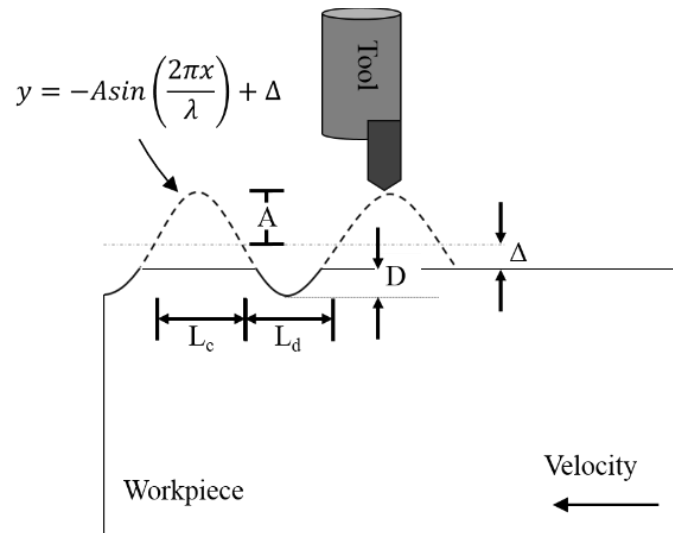
Figure 3: Plunging-type MAT configuration 2D representation and definition of variables

Equations (2) and (3) below describe the tip modulation with respect to position (x), workpiece angle (θ), and time (t).

$$y(x) = -Asin(2\pi x/\lambda) + \Delta \qquad (2)$$

Setting $x = R\theta$, the previous equation can be rewritten:

$$y(\theta) = -A\sin(2\pi R\theta/\lambda) + \Delta \qquad (3)$$

As workpiece angle θ is equivalent to $2\pi f_w t$, circumferential position x is defined as $x = R(2\pi f_w)t$. Substituting this circumferential position equation back into Equation (2), the tip modulation is rewritten as a function of time:

$$y(t) = -A\sin(4\pi^2 R f_w t/\lambda) + \Delta \qquad (4)$$

Texture geometry evaluation

The texture length and distance between texture L_d and L_c as defined in Figure 3 can be found by setting $y(x) = 0$ and solving for the length between the first 3 solutions x_1, x_2, x_3 in the sinusoidal function defined by Equation (2): $-A\sin(2\pi x/\lambda) + \Delta = 0$. Letting temporary variable $\theta_1 = 2\pi x/\lambda$, it can be found that $\theta_1 = \arcsin(\Delta/A)$, leading to the solution for x_1 when solving for x:

$$x_1 = (\lambda/2\pi)\arcsin(\Delta/A) \qquad (5)$$

As sine waves have solutions of period π, $\theta_2 = \pi - \theta_1$ and $\theta_3 = -\pi - \theta_1$ and solutions for x_2 and x_3 can be found:

$$x_2 = (\lambda/2\pi)(\pi - \arcsin(\Delta/A)) \qquad (6)$$

$$x_3 = (\lambda/2\pi)(-\pi - \arcsin(\Delta/A)) \qquad (7)$$

L_d is the length of each texture and is defined as the position where the cutting edge leaves the workpiece surface minus the position where the cutting edge enters the surface. These positions correspond with x_2 and x_1, with $L_d = x_2 - x_1$. Thus:

$$L_d = (\lambda/2\pi)(\pi - 2\arcsin((\Delta/A))) \qquad (8)$$

24

L_c is the distance between textures and is defined as the position where the cutting edge enters the workpiece surface subtracted by the position where it next enters the surface. These positions correspond with x_1 and x_2, with $L_c = x_1 - x_3$. Thus:

$$L_c = (\lambda/2\pi)(2 \arcsin((\Delta/A) + \pi)) \tag{9}$$

Texture depth (D) is defined as the maximum depth over the length of the texture (see Figure 3) and is solved for in Equation (10):

$$D = A - \Delta \tag{10}$$

The texture width (w) is defined in Figure 4, which shows the texture depth and width for an arbitrary tool with tip shape equation $g(z')$ and minimum value equal to zero. Width can be found by solving for the position z on the tool when $g(z') = D$ and finding the difference between solutions. Note that z' is used in place of z to signify that coordinates belong to local tool coordinates, as opposed to global workpiece coordinates. This methodology is presented below, with width w solved for in Equation (11).

$g(z') = D$

Find
$\quad S = \{z'_i | i = 1 \, n\}$
$\qquad$ s.t.
$\qquad\qquad \forall z' \in S$

$$w = |S_1 - S_n| \tag{11}$$
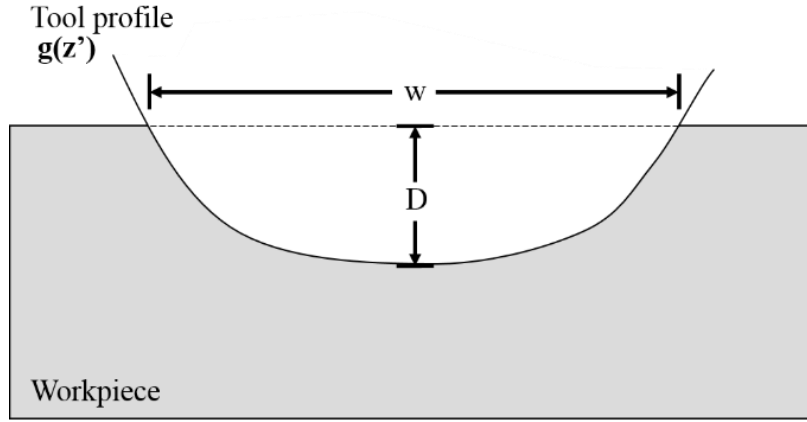
Figure 4: Width definition on texture profile using an arbitrary tool shape for plunging-type MAT configurations

Face plunging-type MAT configurations

Face plunging-type MAT involves creation of surface textures on the face of the workpiece. A schematic of the face plunging-type MAT operation is provided in Figure 5 and the 2D representation of this process is once again provided in Figure 3. In this configuration, the oscillating tool feeds radially towards the center of the workpiece similar to a standard facing operation. While the inputs that define the system are the same for both face and outer diameter plunging, the tool in face plunging follows an Archimedean spiral toolpath as it is fed towards the center of the workpiece at feed (h_0) (Figure 6). As a result, the relative velocity between the cutter tip and the workpiece decreases as the instantaneous radius, r, decreases. An equation for r is given below, where R is the major radius of the workpiece:

$$r = R - h_0(\theta/(2\pi)) \tag{12}$$

Axial position is given as follow and resembles Equation (3):

$$z(\theta) = -A\sin(2\pi R\theta/\lambda) + \Delta \qquad (13)$$

Knowing that $\theta = 2\pi f_w t$, a substitution is made into Equation (13), yielding axial tool tip position as a function of time:

$$z(t) = -A\sin(4\pi^2 f_w tR/\lambda) + \Delta \qquad (14)$$
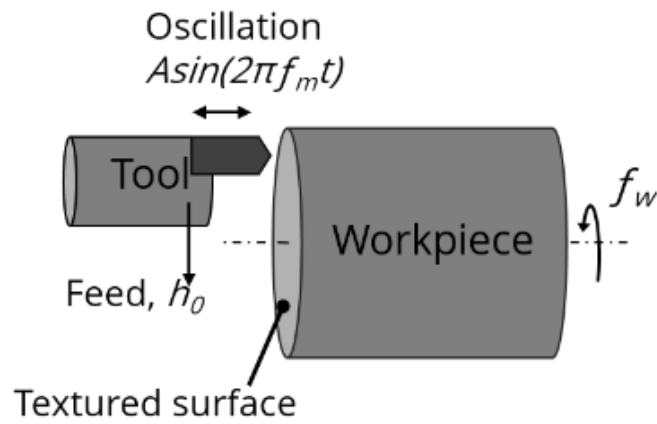
Figure 5: Face plunging-type MAT configuration schematic
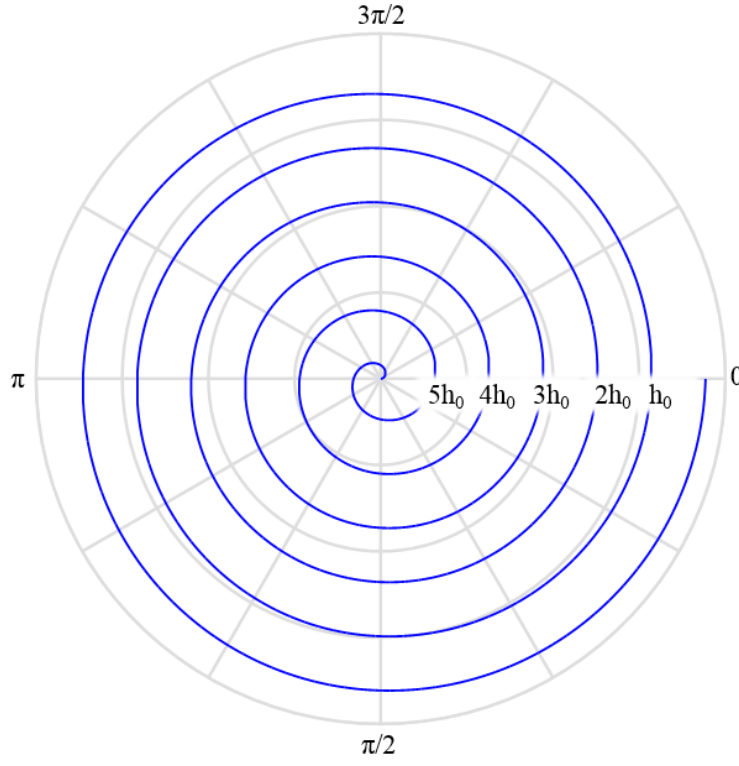
Figure 6: Cross sectional view of toolpath for face plunging-type MAT operation

Texture geometry evaluation

Solutions for texture geometries can be adopted from solutions found in the outer diameter plunging section above. By recognizing that the difference between Equation (2) and (13) is that x is replaced by $R\theta$, the substitution $x = R\theta$ can be made in Equations (5) - (7) to find the solutions of the inverse sine function:

$$\theta_1 = \lambda/(2\pi R) \arcsin(\Delta/A) \tag{15}$$

$$\theta_2 = [\lambda/(2\pi R)][\pi - \arcsin(\Delta/A)] \tag{16}$$

$$\theta_3 = [\lambda/(2\pi R)][-\pi - \arcsin(\Delta/A)] \tag{17}$$

Similar to the calculation performed in Equation (8), the solutions of the inverse sine function in Equations (15) - (17) are used to determine texture length and spacing. As these solutions are for angular position, the difference in angular position is multiplied by the average radial position to find the texture length:

$$L_d = \bar{r}(\theta_2 - \theta_1) \tag{18}$$

The $\bar{r}$ is defined as the average radius across the span of the texture and is provided in Equation (19):

$$\bar{r} = (r_1 + r_2)/2 \tag{19}$$

Using Equation (12), $r_1 = R - h_0(\theta_1/2\pi)$ and $r_2 = R - h_0(\theta_2/2\pi)$, which can be substituted into Equation (19) to find the average radial position over the span of the texture in terms of angular position:

$$\bar{r} = R - h_0(\theta_1 + \theta_2)/4\pi \tag{20}$$

Equation (20) is substituted into Equation (18) to solve for texture length. θ_1 and θ_2 are defined in Equations (15) and (16).

$$L_d = [4\pi R(\theta_2 - \theta_1) - w_0(\theta_2^2 - \theta_1^2)]/4\pi \tag{21}$$

The distance between textures is found similarly to the derivation of texture length. Distance between textures is defined in the following equation:

$$L_c = \bar{r}(\theta_3 - \theta_1) \tag{22}$$

Seeing that Equations (18) and (22) differ only by substituting θ_3 for θ_2, θ_3 is substituted for θ_2 in Equation (23), with θ_1 and θ_3 defined in Equations (16) and (17).

$$L_d = [4\pi R(\theta_3 - \theta_1) - h_0(\theta_3^2 - \theta_1^2)]/4\pi \tag{23}$$

Texture depth and width are calculated identically to the solutions given above for outer diameter plunging-type MAT in Equations (10) and (11).

2.3.2 Sliding-type MAT configurations

Similar to plunging-type MAT detailed above, the cutting tool once again modulates in a sinusoidal toolpath in sliding-type MAT configurations and can be described with amplitude A, wavelength λ, modulation axis offset Δ. Unlike plunging, however, sliding operations maintain the tool-workpiece contact during the entire machining process. Figure 7 shows a schematic of a sliding operation. Sliding-type MAT maintains a constant tool depth in turning, however varies the feed of the tool as it travels along the surface of the workpiece. In this regard, the modulation is oriented parallel to the main axis of rotation, again resulting in decoupling of the effect of cutting speed on the sinusoidal motion of the tool. As with plunging-type MAT, the cross-sectional profile of the toolpath is determined by the tool shape and its interaction with the work surface. Figure 8 shows a possible sliding toolpath on the outer diameter of a cylindrical workpiece. In this sliding operation, texturing occurs at angular workpiece positions between zero and 2π, and have a distance of feed (h_0) between consecutive toolpaths. Figure 9 shows a 2D representation of the outer diameter of this cylindrical surface. This figure shows two tool traces of a modulating tool and shows how consecutive toolpaths may intersect depending on the machining and modulation conditions.
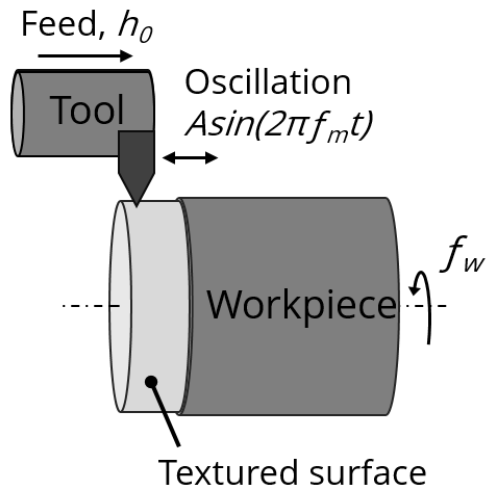
Figure 7: Sliding-type MAT configuration schematic
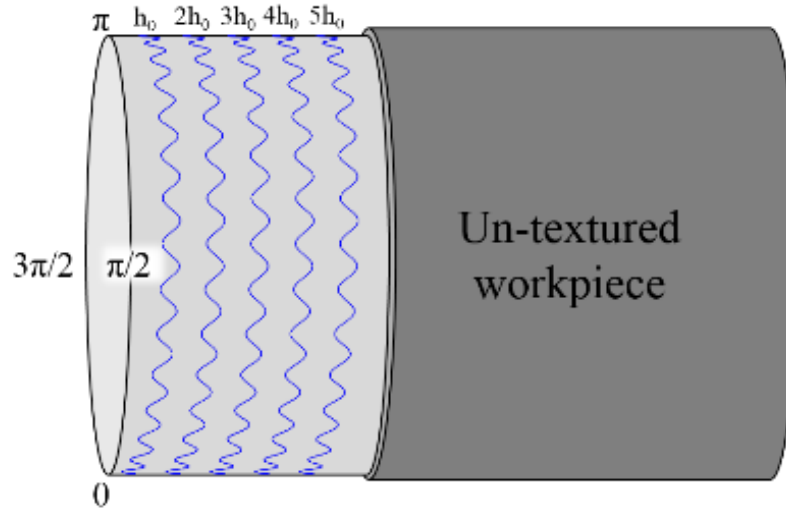
Figure 8: 3D representation of sliding-type MAT texture
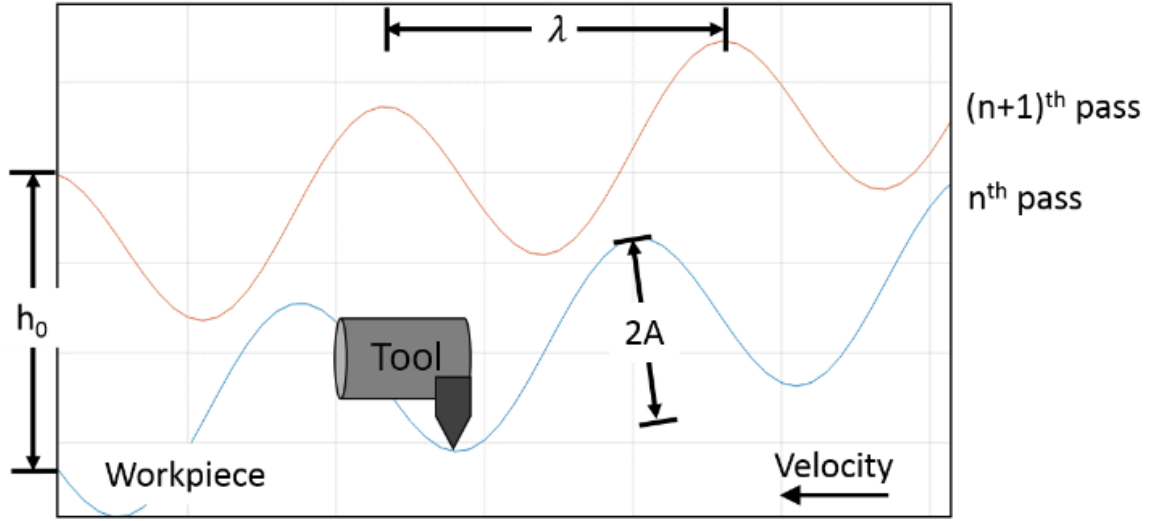
Figure 9: Sliding-type MAT texture 2D representation

The tip position of the cutting tool is dependent on the constant axial feed and the superposed modulation. The modulation position is defined similarly to that in Equation (2):

$$z(x) = -A\sin(2\pi x/\lambda) \qquad (24)$$

Combining $x = R\theta$, where R is the major diameter of the cylindrical workpiece, and $\theta = 2\pi f_w t$, it is found that $x = 2\pi R f_w t$. The modulation position can be rewritten to be expressed in terms of θ and t in Equations (25) and (26), respectively:

$$z(\theta) = -A\sin(2\pi R\theta/\lambda) \qquad (25)$$

$$z(t) = -A\sin(4\pi^2 R f_w t/\lambda) \qquad (26)$$

Equation (26) can be rewritten to account for axial feed $(-h_0 f_w t)$ to yield tip position with respect to time:

$$z(t) = -h_0 f_w t - A\sin(4\pi^2 R f_w t/\lambda) \qquad (27)$$

32

Solving for t in the equation $x = 2\pi R f_w t$ and substituting $t = x/(2\pi R f_w)$ into Equation (27) yields cutter tip position with respect to circumferential position:

$$z(x) = -h_0 x/(2\pi R) - A\sin(2\pi x/\lambda) \qquad (28)$$

Substituting $x = R\theta$ into Equation (28) yields a cutter tip position equation with angular position as a variable:

$$z(\theta) = -h_0\theta/(2\pi) - A\sin(2\pi R\theta/\lambda) \qquad (29)$$

The phase difference (φ) between two consecutive toolpaths determines the type of texture created, and is calculated in Equation (30):

$$\varphi = 2\pi(\frac{f_m}{f_w} - INT[\frac{f_m}{f_w}]) \qquad (30)$$

where *'INT'* denotes the nearest integer less than or equal to the element that follows in brackets. For the domain of all real numbers, the phase is limited to $0 \leq \varphi < 2\pi$.

Surface texture geometry evaluation

The length between intersecting toolpaths determines the resulting surface texture geometry and can be found with two different methods. The first method consists of solving for the distance between the intersections of consecutive toolpaths, while the second recognizes that a specific number of surface features are evenly spaced over a full workpiece rotation. Knowing the workpiece circumference and the number of surface features allows for calculations of feature geometries.

Solving for the intersection of consecutive toolpaths occurs when the position of the tool equals the position of the tool after a full rotation, and is expressed mathematically in Equation (31).

$$\sin(2\pi x/\lambda) = \sin(2\pi(x + 2\pi R)/\lambda) + h_0(2\pi R) \qquad (31)$$

33

Using the trigonometric identity $sin(x + y) = sin(x)cos(y) + cos(x)sin(y)$, Equation (31) can be expressed as Equation (32):

$$sin(2\pi x/\lambda) = sin(2\pi x/\lambda)cos(4\pi^2 R/\lambda) + cos(2\pi x/\lambda)sin(4\pi^2 R/\lambda)$$
$$+ 2h_0\pi R \tag{32}$$

Rearranging Equation (32) yields Equation (33).

$$sin(2\pi x/\lambda)[1 - cos(4\pi^2 R/\lambda)] - cos(2\pi x/\lambda)sin(4\pi^2 R/\lambda) = 2h_0\pi R \tag{33}$$

To simplify Equation (33), let $\theta, A, B,$ and C equal the following values, leading to the simplified Equation (34):

$\theta = 2\pi x/\lambda$

$A = 1 - cos(4\pi^2 R/\lambda)$

$B = sin(4\pi^2 R/\lambda)$

$C = 2h_0\pi R$

$$Asin(\theta) - Bcos(\theta) = C \tag{34}$$

Using trigonometry to solve for θ yields Equation (34):

$$\theta = \arctan\left[(2AB \pm \sqrt{4A^2B^2 - 4(A^2 - C^2)(B^2 - C^2)}/(2(A^2 - C^2))\right]$$
$$+ n\pi \tag{35}$$

Solving for x in the substitution $\theta = 2\pi x/\lambda$ from Equation (34) gives the two circumferential positions intersection points x_1, x_2:

$$x_1, x_2 = (\lambda/2\pi)\arctan(2AB$$
$$\pm\sqrt{4A^2B^2 - 4(A^2 - C^2)(B^2 - C^2)}/(2(A^2 - C^2))) \tag{36}$$

The length of the surface texture (L_s) is equal to the quantity $(x_2 - x_1)$

Equation (37) provides a more general solution set for the intersection points for feature n, as opposed to the solutions provided in Equation (36) which solves only for the first two intersection points:

$$x_{2n-1}, x_{2n} = (\lambda/2\pi)(\arctan(2AB$$
$$\pm \sqrt{4A^2B^2 - 4(A^2 - C^2)(B^2 - C^2)/(2(A^2 - C^2)))} \quad (37)$$
$$+ (n-1)\pi)$$

For feature number n, the texture length L_s is equal to $(x_{2n} - x_{2n-1})$:

$$L_s = x_{2n} - x_{2n-1} \quad (38)$$

While Equations (1) - (38) have solved for the explicit locations of intersection points which is beneficial for modeling purposes, the texture geometry calculations can be simplified by recognizing that a specific number of surface textures span the circumference of the workpiece. Figure 10 provides four phase shift possibilities and defines length and width for each of these cases. For all cases except for the complete, in-phase condition ($\varphi = 0$), length (L_s) of textures is defined as the maximum horizontal length from one local extreme to a local extreme of the opposite sign on a consecutive trace. This definition is made clearer in panels (a) − (c) of Figure 10, where separate phase shifts provide multiple examples of width and length calculations. The in-phase condition does not have a length, because texture length is considered infinite. The definition of the width of a texture is more straightforward, and is defined as the maximum vertical distance between a toolpath and a subsequent toolpath.
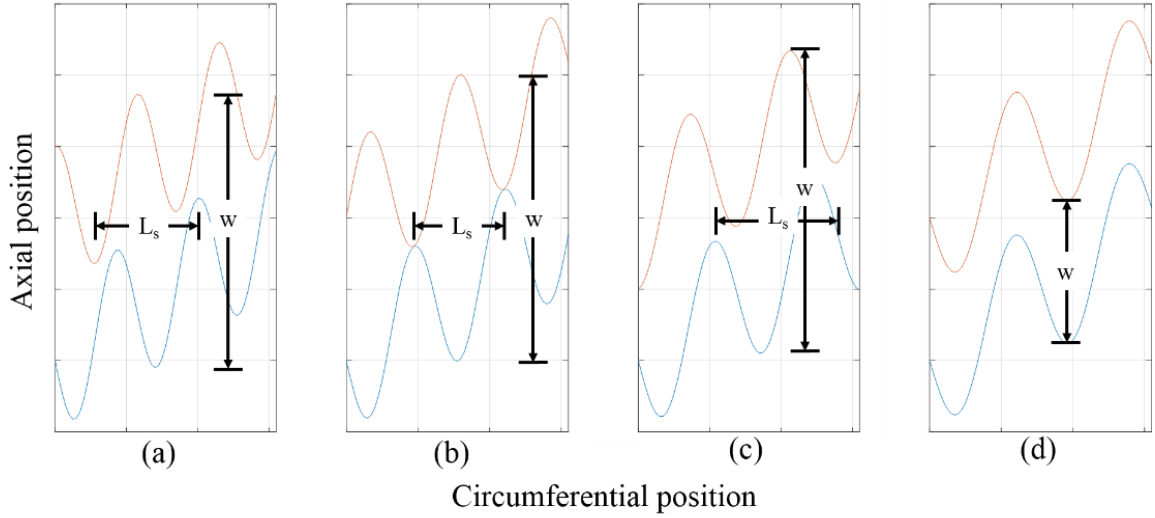
Figure 10: Length (L_s) and width (w) definitions of textures of different phase shift: (a) $3\pi/2$, (b) π, (c) $\pi/2$, (d) 0.

Length of texture (L_s) is calculated by adding the sinusoidal wavelength to the percentage of the wavelength that is offset. Knowing that $\lambda = 2\pi R(f_w/f_m)$, the length of the sliding texture is calculated in Equation (39) for all cases except for completely in-phase conditions, where *INT* once again denotes the integer value of the fraction in parentheses:

$$L_s = 2\pi R \left(\frac{f_w}{f_m}\right) + \left(\frac{f_m}{f_w} - INT\left[\frac{f_m}{f_w}\right] - 0.5\right)\lambda \qquad (39)$$

Width (w) is defined for out-of-phase conditions as the maximum vertical measurement on the surface texture (Figure 10).

$$w = 2A + h_0 \qquad (40)$$

For complete in-phase conditions, the width is defined as the distance between consecutive passes, which is the tool feed (Figure 10).

36

$$w = h_0 \tag{41}$$

The height of the surface texture depends on the profile of tool with a generic tool tip equation $g(x')$ with a minimum of zero. Equations (42) and (43) calculate the feature height values. The inequality conditions exist because maximum texture height is limited to the tool's depth-of-cut. As before, x' is used in place of x to indicate the use of a local coordinate system located on the tool itself.

$$h = g\left(\frac{w}{2}\right) \qquad \text{for } g\left(\frac{w}{2}\right) < |\delta| \tag{42}$$

$$h = \delta \qquad \text{for } g\left(\frac{w}{2}\right) > |\delta| \tag{43}$$

Additional considerations

An understanding of modulation characteristics and resulting toolpaths helps inform the macroscopic texture morphologies. Similar to how phase shift can create features of various shapes, Figure 11 shows the conditions necessary to achieve cutting that intersects with consecutive tool passes. From a holistic level, the minimum amplitude to feed ratio needed occurs at $\varphi = \pi$. As the phase deviates from this ideal condition and approaches the two extremes ($\varphi = [0, 2\pi]$), the A/h_0 ratio increases at an increasing rate. The practical consequence of this is that to reach intersection conditions, parameters near $\varphi = \pi$ should be chosen as small variations in phase only necessitate small deviations in the necessary A/h_0 ratio. At the two extremes, small variations in phase require drastically different A/h_0 ratios and failure to intersect becomes more readily apparent.
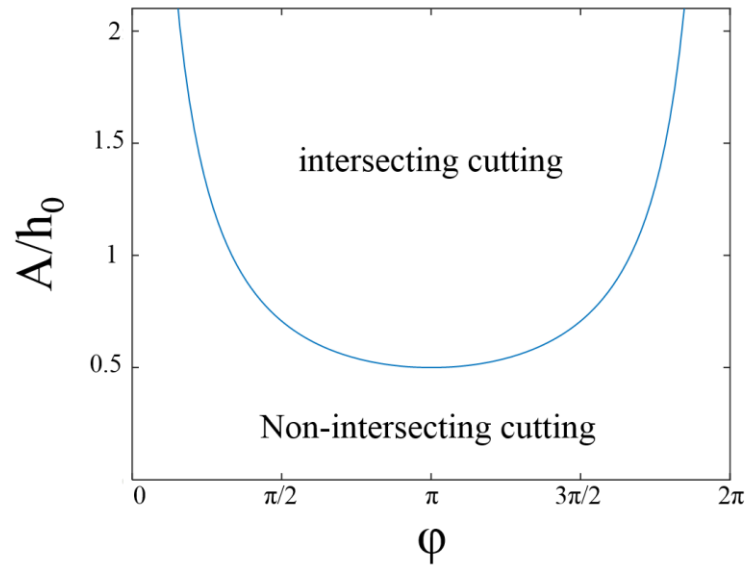
Figure 11: Intersection conditions for sliding-type MAT textures

CHAPTER 3

MATERIALS AND METHODS

This chapter provides an explanation of the experimental systems used for manufacturing, characterizing and testing the textured surfaces. Samples were produced for: (1) validation of surface generation models for micro-feature fabrication, (2) testing of bio-integration, and (3) friction and wear performance testing. The methods outlined here are intended to allow for full repeatability of experiments.

3.1 MAT experimental system

An Okuma Spaceturn LB2000 2-axis computer-numerical control (CNC) turning center was used for all experiments. The machine uses a TRIM MicroSol 690XT water-based flood coolant and was limited to 5000 RPM during all experiments. Machining procedures were written with g-code to maximize controllability between experiments. A number of control electronics were used for both controlling the modulation unit and measuring dynamic parameters. An AFG3021B waveform generator capable of outputting sinusoidal waveforms of frequency 1 μs to 1 ks with voltage between 0 and 7.5 V was used in conjunction with an M4 Sciences PA11033A power amplifier that amplified incoming signals by 20V/V. The resulting sinusoidal voltage output is amplified to between 0 and 150 V. Tool modulation was driven by an electro-mechanical tool holder (TriboMAM, M4 Sciences), which consists of a piezo-electric stack that translates voltage differences into stack displacement. This piezo-electric stack is decoupled from off-axis machining forces by a linear bearing [138]. Figure 12 shows the modulation actuator system and its supporting fixture. The steel plates (left) are stacked

39

and screwed into the turret on the lathe (right). The piezo actuator was measured to have a capacitance of 40 µF.
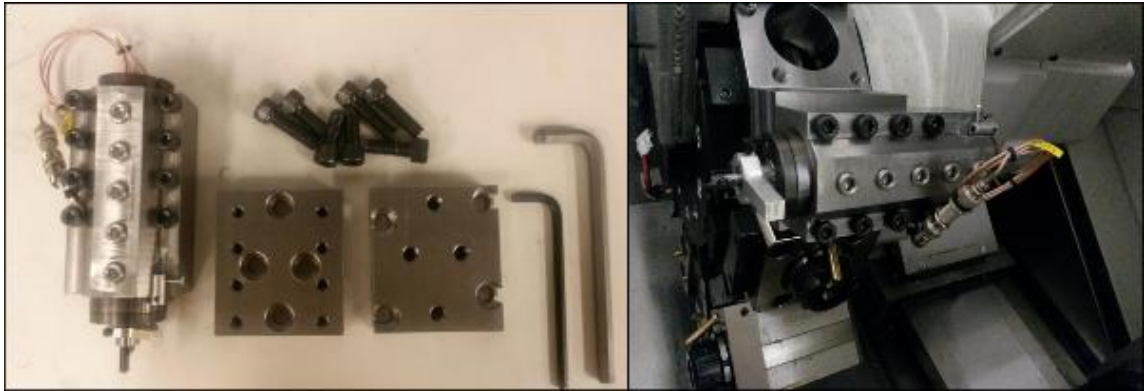
Figure 12: MAT mounting system both disassembled (left), and assembled on the lathe (right)

Prior to MAT, all samples were made from Brass 360 and prepared to mirror-finish conditions by taking 0.254 mm deep roughing cuts using a TNMG432K roughing insert with 1/32" nose radius constant surface speed 112 m/min and feed 0.003 mm/rev; followed by a 0.127 mm depth of cut finishing pass using a Kennametal 3659967 PCD turning insert style CCGW with a 0.4 mm nose radius, 34 m/min constant surface speed and 0.003 mm/rev feed. The manufacturing conditions for the MAT surface textured samples are provided in Table 2. An Iscar MITR 8-MT1-0.05 threading insert [139] with 0.05 mm nose radius and 60 degree point was used for all sliding experiments. This insert is depicted in Figure 13. The roughing and finishing tool was set using an automatic touch-off probe and verified with a micrometer. Because of fixturing constraints, y-axis mode was used for the modulation unit. While y-axis mode allows for an additional axis

of movement, it precludes the use of the automatic touch-off probe. As a result, an electronic touch-off technique was used, which measures the resistance between the finished workpiece and the MAT cutting tool (with DC voltage set to the desired offset that is to be used in subsequent testing). The MAT tool was brought closer to the workpiece in increments of 0.003 mm until a sharp decrease in electrical resistance was seen. This position was set as the z-zero location. A Zygo NewView 200 interferometer was used to observe that cutting did not occur when tools were set to zero depth-of-cut, yet revealed shallow grooves when depth-of-cut was set to -0.003 mm. It should be noted that the piezoelectric actuator had a time constant of about 5.7 seconds, meaning that to reach 99.3% of steady state displacement, DC voltage must be run for about 28.5 seconds. The MATLAB code for analyzing displacement after the onset of DC voltage is provided in Appendix A: charging_Tc_finder.m.

Figure 13: An Iscar MITR 8-MT1-0.05 threading tool with Tmax-r=1.23 mm, R=0.05 mm, and I=5.75 mm [139]

Table 2: Manufacturing conditions for sliding-type MAT textures

Sample Description (φ)	f_m (Hz)	V_{pp} (V)	V_{off} (V)	a_p (mm)	Diameter (mm)	h_0 (mm/rev)	f_w (Hz)
1 ($\varphi = 0$)	100.00	112	75	0.064	7.62	0.064	1
2 ($\varphi = \pi/2$)	100.25	112	75	0.064	7.62	0.064	1
3 ($\varphi = \pi$)	100.50	112	75	0.064	7.62	0.064	1
4 ($\varphi = 3\pi/2$)	100.75	112	75	0.064	7.62	0.064	1

3.1.2 Instrument verification

Machine and sensor data was recorded using an NI PCI 4472 data acquisition system. A LabVIEW program was used to collect data in terms of spindle speed, modulation displacement, and force data. Roughing and finishing tool position was verified by turning surfaces and using a Nikon Microphot-FX microscope to confirm that the distance between machined grooves matches the desired machine feed. Tools were visually inspected before each test for quality (i.e. built-up edge, chipped faces, excessive wear, etc.) and replaced if deemed inadequate.

The power amplifier's performance envelope was characterized by attaching a bi-directional capacitor to the amplifier and determining the maximum allowable output frequency for a given output peak-to-peak voltage. This was performed using both a 40 µF capacitor whose capacitance matches that of the MAT device and a 10 µF capacitor. The behavior is shown in Figure 14 and provides information regarding the range of frequency and voltage that can be output from the amplifier without encountering current limiting conditions. Though both capacitors exhibit roll-off behavior, as expected, the 40 µF capacitor begins to current limit at lower V_{pp} and frequencies than the 10 µF capacitor. At 200 Hz, the 10 µF capacitor has full range of V_{pp} while the 40 µF system is

limited to about 50 V$_{pp}$. A capacitive displacement sensor system was used to evaluate the MAT system's motion capabilities. This system consisted of a Capacitec 200 series capacitance probe and a grounded aluminum target (Figure 15). The probe was positioned to have an initial voltage output of ~5 V, corresponding to half of full range. Figure 16 shows the linear relationship between DC voltage and actuator displacement, with $Displacement = 0.0006 * V_{dc} - 0.0009$. These data were taken with the MAT unit clamped in a machining vise and displacement was allowed to reach steady state over 28 seconds (5 time constants). This figure shows that, in addition to the largely predictable relationship between DC voltage and actuator displacement, the maximum MAT displacement is 90 μm at maximum DC voltage.
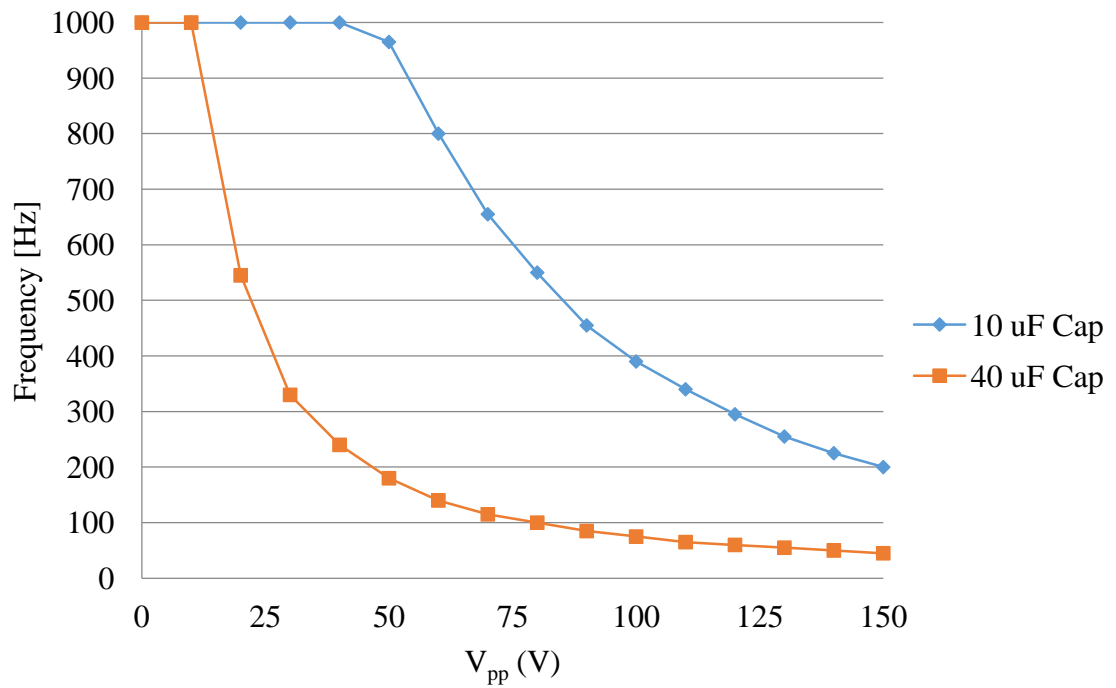
Figure 14: Characterization of IC amplifier peak-to-peak voltage (V_{pp}) verses frequency (f_m) when loaded with a 10 and 40 μF capacitor. All tests were run at 75 V offset voltage (V_{off})
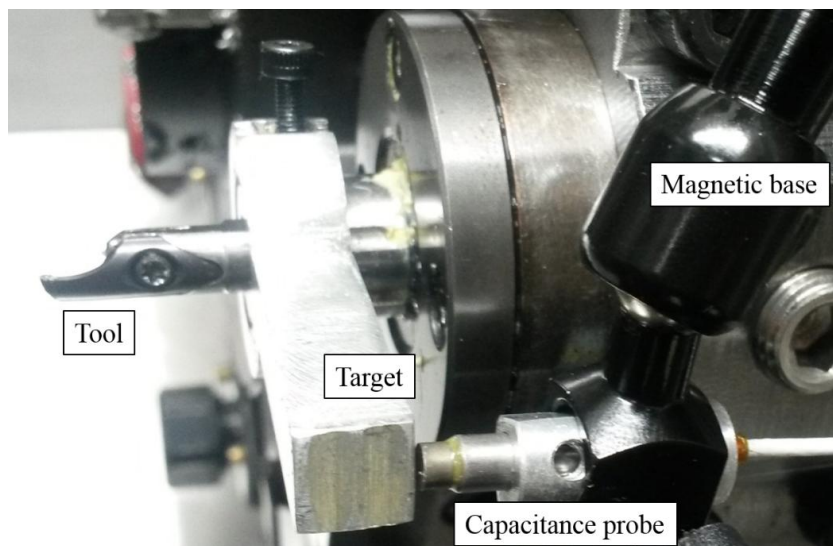
Figure 15: MAT displacement acquisition system using fixed aluminum target and capacitance probe
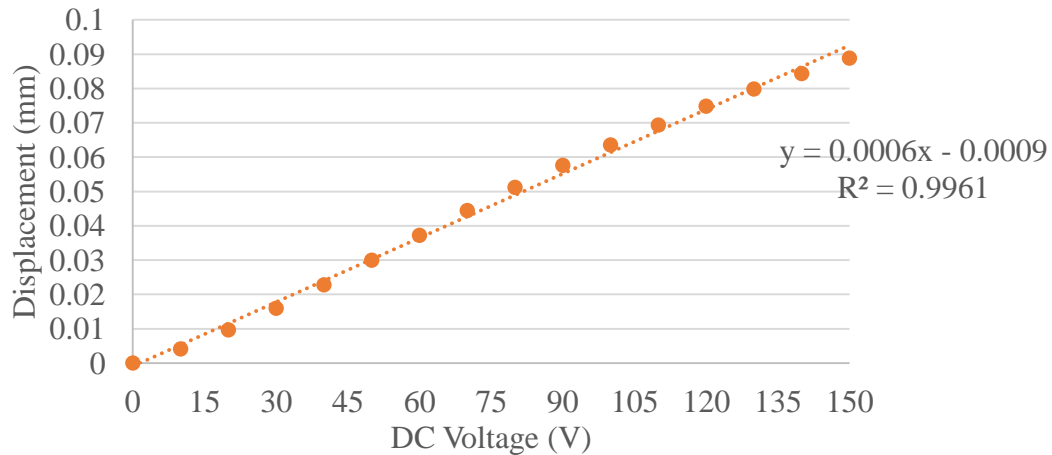
Figure 16: MAT device voltage vs. displacement graph

In a similar fashion, the relationship between peak-to-peak voltage (V_{pp}), modulation frequency (f_m), and modulation amplitude (A) was established. Mean amplitude was measured using a least-squares sinewave fit that. Figure 17 shows the modulation amplitude for an array of frequencies as a function of V_{pp}. Power-limited performance of the amplifier prevented modulation frequencies above 50 Hz from spanning the full range of actuator displacement. For the 100 Hz and 200 Hz curves (at voltages less than 80 V_{pp}), the modulation amplitude is equivalent to that at lower frequency, while higher frequencies either give smaller or larger amplitudes. Figure 18 shows modulation amplitude as a function of modulation frequency for several peak-to-peak input voltages. This figure once again shows that large modulation amplitudes may only be reached using low frequency and large V_{pp}. It also more clearly shows the non-linearity of response for modulation frequencies in excess of 200 Hz.

45
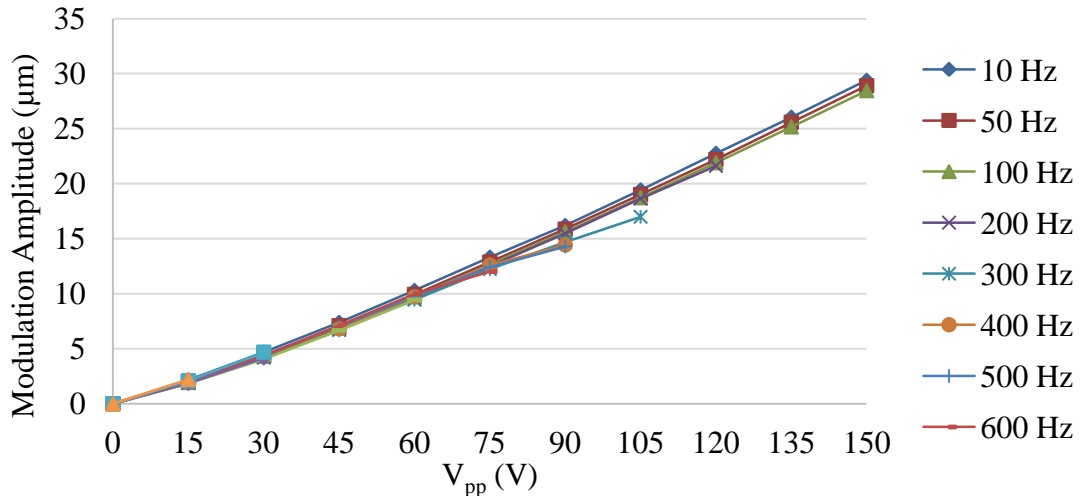
Figure 17: Modulation amplitude verse peak-to-peak input voltage, at different modulation frequencies
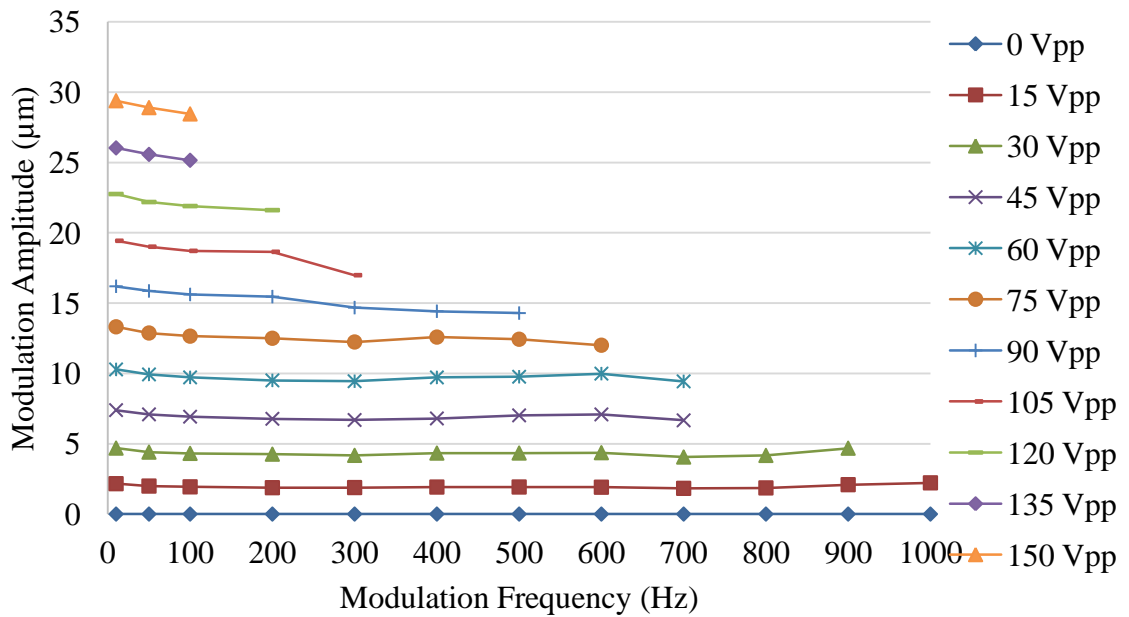
Figure 18: Modulation amplitude verses modulation frequency at different peak-to-peak input voltages

46

Data processing and analysis was performed with modified versions of MATLAB scripts that were previously developed [140] and are provided in full in Appendix A. Cycle-dependent frequency was calculated by linearly interpolating nearest zero values and using a least-squares regression to find the temporal locations of zero values (MAMlathe_freqdist_finder.m). Every second data point was discarded to maintain only one zero crossing per sinewave period before calculating $f = 1/T$, where T is the measured sinewave period. Amplitude for each modulation cycle was calculated by a least squares fit of the data (MAMlathe_Asave_finder.m). A MATLAB sliding simulation was developed and was used to evaluate the effects of parameter variation on final texture morphology. The 3D model allows for macroscopic evaluation of textures (i.e. visual comparisons) and geometric measurements of width, length, and height data at user-determined resolution. These simulations allow for the input parameters f_m, f_w, δ, A, h_0, and the geometry of the tool, and can be found in Appendix A.

3.2 Orthopedic testing configuration

The final textures were manufactured with a sliding-type MAT orientation, using the same Iscar MITR 8-MT 1-0.05 threading insert used in the sliding experiments. Prior to texturing passes, all samples were turned with a TNMG432K roughing tool and a CCGW 3659967 PCD finishing tool. For both *in vitro* and *in vivo* samples, roughing passes were taken at 0.0025 mm/rev, 112 m/min, and 0.254 mm depth of cut, while finishing passes were accomplished at 0.0025 mm/rev, 34 m/min, and 0.127 mm depth of cut. The samples were made from grade 2 commercially pure titanium and were manufactured to

have two distinct surface conditions: a complete in-phase texture and a complete out-of-phase texture.

3.2.1 *In vitro* studies

A series of *in vitro* experiments were performed to elucidate effects of surface texture on osseointegration compared to conventional smooth and sandblasted controls. This study investigates biological function in two stages. The first stage evaluates the amount of cell adhesion found on each of the experimental surfaces and the second stage measures the amount of differentiation after the addition of osteogenic media. These two measures constitute the previous two steps of bone remodeling that are precursors to bone matrix deposition.

<u>Samples design</u>

The specific samples that were tested are detailed in each of the experimental sections below. Four groups of samples were manufactured from 5/8" titanium rods. Samples were machined to have dimensions of 1 x 1 x 0.5 cm with specified radius of curvature. The 0.5 cm dimension is the maximum distance from the curved face to the largest flat face, and the radius of curvature is equal to 0.25" for all experiments except for Experiment 1. Figure 19 shows the steps undertaken to manufacture the specimens for *in vitro* testing. Control sandblasted samples, which constitute the conventional surface processing method, were processed by applying 170 Grit Glass Beads at 80 PSI for 10 minutes. Control smooth samples were produced under the same finishing conditions as the textured samples.

Figure 19: *In vitro* sample manufacturing procedure. (1) turn cylindrical stock to specified diameter, (2) texture rod (if using MAT process) and part from stock, (3) use end mill to face and slot part, (4) use wire EDM to cut two curved samples from each workpiece.

The surface textured samples studied were a completely in-phase sample ($\varphi = 0$) and a completely out-of-phase sample ($\varphi = \pi$). Both of these samples were machined at a depth of cut of 0.056 mm, feed of 0.071 mm/rev, spindle frequency of 1.4 Hz, and modulation voltage of $V_{pp} = 112$ V. The modulation frequency was set to 219.8 Hz for the in-phase condition, while a frequency of 220.5 Hz was used for the out-of-phase condition. Table 3 summarizes the machining and modulation parameters used for sample creation and

Table 4 shows the corresponding measurements of the machined samples. Figure 20 provides optical images of the textured samples. The shape and size of the resulting textures were measured using a Nikon Microphot-FX microscope with at least 5 measurements for each sample. After fabrication, samples were cleaned an ultrasonic shaker for 10 minutes and were rinsed with acetone and distilled water prior to autoclaving.
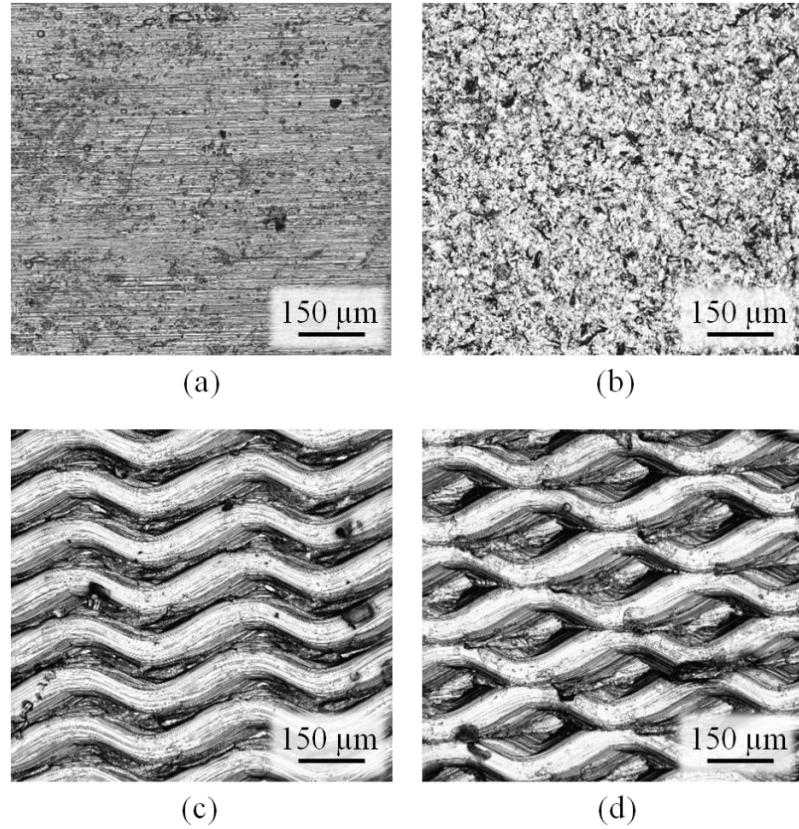
Figure 20: Light microscopy image of *in vitro* test samples (a) smooth, (b) sandblasted, (c) in-phase sliding sample, (d) out-of-phase sliding sample

Table 3: Manufacturing conditions of *in vitro* samples

Sample Description	f_m (Hz)	V_{pp} (V)	V_{off} (V)	a_p (mm)	Curvature (inches)	h_0 (mm/rev)	f_w
TT1 (smooth)				0.254	0.25	0.003	112 m/min
TT2 (sandblast)				0.254	0.25	0.003	112 m/min
TT3 (MAM φ = 0)	219.8	112	75	0.056	0.25	0.071	1.4 Hz
TT4 (MAM φ = π)	220.5	112	75	0.056	0.25	0.071	1.4 Hz

Table 4: *In vitro* sample measurements

Sample Description	# samples	Average Ra (µm) ± σ	Length (µm) ± σ	Width (µm) ± σ	Height (µm) ± σ
TT1 (smooth)	10	0.28 ± 0.02			
TT2 (sandblast)	10	0.64 ± 0.08			
TT3 (MAM φ = 0)	10			72.09 ± 3.98	15.22 ± 0.89
TT4 (MAM φ = π)	10		251.29 ± 3.96	108.30 ± 0.96	25.13 ± 1.09

Experimental procedures

In vitro experiments were used to understand the effects that MAT surface textures have on osseointegration. Live / dead viability assays were performed in Experiments 1-4. Experiment 1 was designed to determine a sample radius of curvature that is acceptable for cell seeding. After finding a sufficient radius of curvature, Experiment 2 was conducted to compare the viability of an untextured control verses a textured sample as a preliminary proof-of-concept study. Experiment 3 provided a live / dead study on anodized samples to qualitatively show texture viability. Experiment 4 involved quantitative measurement of cell adhesion on the surfaces of each of the control and textured surfaces, and Experiment 5 was conducted to evaluate the ALP and DNA content on the experimental surfaces. Cell adhesion and viability was evaluated through live / dead assays, and are evaluated both qualitatively and quantitatively. Pre-osteoblastic differentiation is evaluated by measuring alkaline phosphatase (ALP) activity and DNA levels after adding osteogenic media and were quantitatively compared.

Adhesion, differentiation, and proliferation studies used to quantify the cell growth on surfaces are typically performed in tissue culture wells on flat surfaces. Fabricated surfaces in this present study are inherently cylindrical and, thus, the effect of curvature on cell adhesion was studied in Experiment 1. Three specimens were turned to a radius of curvature of 0.2", 0.2625", and 0.325". In this experiment, the osteoblast precursor MC3T3-E1 was seeded at 32,000 cells/cm^2 into individual well suspension culture plates with sufficient medium to submerge test samples. Live / dead assays were performed after 48 hours of seeding and were stained with Calcein, which illuminates live cells in green. Dead cells were stained using an ethidium homodimer assay, which illuminates dead cells in red. The resulting light microscopy images are a composite of green and red, and also show the cellular morphology for both assays. The rocking conditions typically performed for labeling purposes were omitted for all *in vitro* samples due to low interfacial shear strength observed on samples.

After establishing a radius of curvature that allow for adequate cell adhesion, a radius of curvature of 0.25" was used for all subsequent *in vitro* studies. A second experiment was performed to compare the viability of cells on an untextured control (TT1) to an in-phase MAT sample (TT3). The sample preparation and experimental procedures were otherwise identical to that of Experiment 1.

A full visualization of the adherence of cells to textured surfaces was made possible by anodizing samples in Experiment 3. This anodization process thickens the titanium oxide layer, which has been shown in literature to improve osteoblast adhesion to Ti [141, 142] and aids in the visualization of live / dead test results. Anodization, however, is not performed in any other experiment as to avoid confounding the raw effects of MAM texturing on osseointegration. Type 2 anodization of one sample per test

group was performed by Danco Anodizing. Figure 21 shows the surfaces of each sample post anodization. Notice the rounding of features and the micro-pits that are formed on the sample surfaces – the untextured and sandblasted samples are virtually indistinguishable. This rounding is inherent to the anodization process, but allows for cell adherence on surface features to be clearly seen.
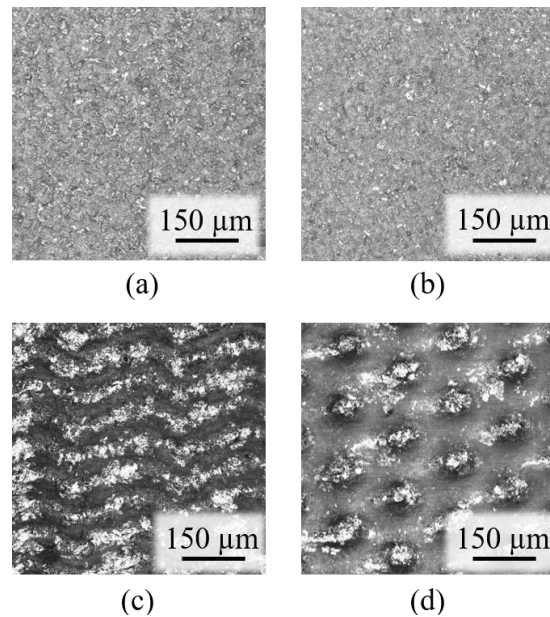
Figure 21: Light microscopy image of <u>anodized</u> i*n vitro* test samples (a) smooth, (b) sandblasted, (c) in-phase sliding sample, (d) out-of-phase sliding sample

Quantifying cell adhesion was performed in Experiment 4 using the same procedures as above, however instead of performing a live / dead assay, cells were trypsinized from sample surfaces and neutralized. In this study, all four test groups (n=10 / group) were seeded with cells and cultured for one week. Cells were counted on a hemocytometer in four separate locations in batches of 250. Counting the cells that were

removed from specimen surfaces circumvented cell crowding issues inherent to counting cells on live / dead images and provided more accurate quantification. Note that samples were in suspension culture plates, which prevented attachment of cells outside of the desired textured area.

The level of osteoblast differentiation was quantified in Experiment 5 by assaying for ALP and DNA content. These pre-osteoblastic differentiation experiments were performed using the same samples in Experiment 4 with n = 5 / group. Samples were initially frozen in lysis buffer before the addition of osteogenic media, which triggered differentiation in live cells. Typically, to measure ALP and DNA content, it is first necessary to have a fully confluent monolayer before adding osteogenic media that promotes differentiation. Because of the lack of confluence on all samples, however, ALP and DNA content was normalized to the number of cells, which accommodates the differences in cell seeding and attachment. After one week of differentiation, an ALP and DNA assay in control medium were utilized and analyzed in a Powerwave XS Plate reader to investigate whether surface texture encouraged differentiation.

3.2.2 *In vivo* studies

In addition to the *in vitro* experiments, *in vivo* experiments were also performed to study the effects of surface modification on osseointegration. This study investigated osseointegration on a macroscopic level by comparing bone volume density values from μCT scans and measuring implant pull-out strength. For this purpose, a rat medial tibial metaphysis *in vivo* model was utilized for bilateral implantation of implants. These studies were performed in male Sprague Dawley rats with starting weight of about 300 g. As with the *in vitro* studies, the *in vivo* studies were designed to have four test groups with n=8 for each group, resulting in a total of 32 implants and 16 animals used.

In the present study, commercially pure titanium implants were fabricated into 2 mm diameter implants from 1/8" rods. Figure 22 shows a schematic of the textured implant design and the textured region for these samples. A 0.40 mm through-hole was drilled through the larger end of each implant to facilitate fixturing for pull-out testing. After the diameter reduction, MAT textured samples were machined with a 0.056 mm depth of cut, 0.071 mm/rev, 4 Hz spindle speed, and 112 V_{pp} peak-to-peak modulation voltage. In-phase samples were machined with 100 Hz modulation frequency and out-of-phase samples were machined with 102 Hz modulation frequency. A finishing pass with the PCD tool with zero depth of cut was performed to minimize the residual surficial burrs. Sandblasted samples were processed using 170 grit glass beads at 80 PSI for 10 minutes.
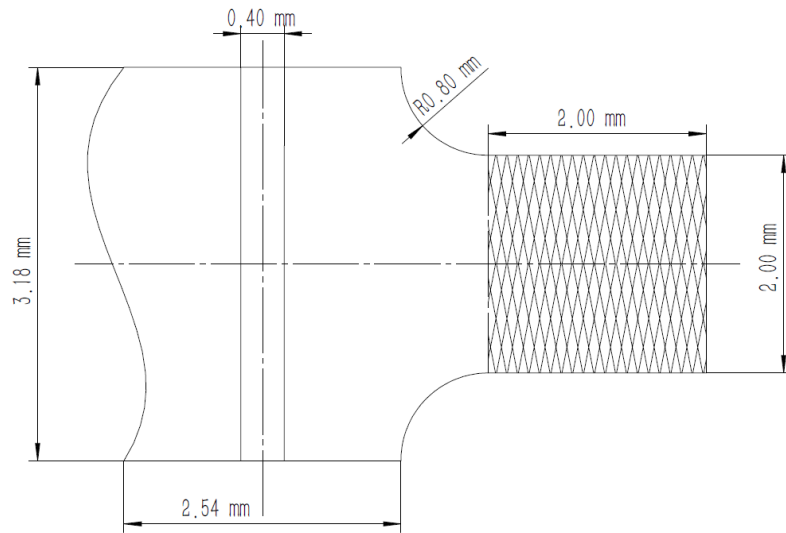
Figure 22: Schematic of textured implant for *in vivo* studies

Figure 23 shows representative images of the resulting machined implants. The implant on the bottom right shows an implant that has been milled to have 0.1" stickout. The implant on the top left is an implant that has not been milled to size. Table 5 summarizes the manufacturing conditions used to create the four test conditions, Figure 24 shows microscopy scans of representative samples and Table 6 shows the roughness and geometric measurements of the micro-textures found on each sample. After fabrication, all samples were cleaned in an ultrasonic shaker for 10 minutes and rinsed with acetone and distilled water prior to autoclaving.

Figure 23: Representative test samples used in *in vivo* testing. Top right sample does not have the final side milling step, which shortens the implant to the sample seen on the bottom left
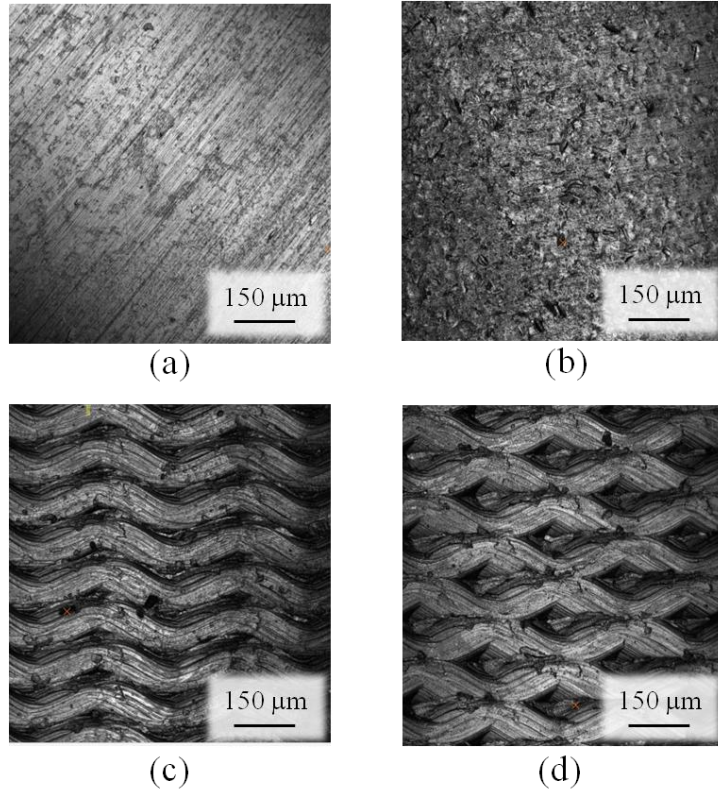
Figure 24: Light microscopy image of *in vivo* test samples (a) smooth, (b) sandblasted, (c) in-phase sliding sample, (d) out-of-phase sliding sample

Table 5: Manufacturing conditions of *in vivo* samples

Sample Description	f_m (Hz)	V_{pp} (V)	V_{off} (V)	a_p (mm)	Diameter (mm)	h_0 (mm/rev)	f_w
TT1 (smooth)				0.254	2.00	0.003	112 m/min
TT2 (sandblast)				0.254	2.00	0.003	112 m/min
TT3 (MAM φ = 0)	100.0	112	75	0.056	2.00	0.071	4 Hz
TT4 (MAM φ = π)	102.0	112	75	0.056	2.00	0.071	4 Hz

Table 6: *In vivo* sample measurements

Sample Description	# samples	Average Ra (μm) ± σ	Length (μm) ± σ	Width (μm) ± σ	Height (μm) ± σ
T1 (smooth)	8	0.28 ± 0.01			
T2 (sandblast)	8	0.49 ± 0.06			
T3 (MAM φ = 0)	8			70.79 ± 1.74	13.37 ± 0.85
T4 (MAM φ = π)	8		232.89 ± 5.87	106.32 ± 2.79	24.26 ± 0.65

Experimental procedures

Samples were implanted into animals over two days on November 18 and 19, 2016 in Georgia Institute of Technology's Physiological Research Laboratory and remained in animals for 4 weeks. 17 Sprague Dawley rats were used, with one rat that was lost during post-operative procedures. A strict aseptic protocol was followed, with one surgeon, one sterile assist doing animal preparation, and one non-sterile assist aiding in the general tasks in the operation room. Pre-operative procedures were as follows. 5% isoflurane with 100 cc/min O_2 was delivered to rats until found unconscious. Puralube vet ointment by Dechra was applied to eyes. The back of the head was shaved and sterilized with methanol before injection of 0.8 mg/kg buprenorphine. Ears were tagged for identification. Both legs were shaved and sterilization pads were attached to feet before sterilization with 2% dermachlor solution (chlorhexidine gluconate by Henry Schein) and methanol wipes. Post-operative procedures were as follows. Feet sterilization pads were removed. Wiping down of incision sites with H_2O_2.

Implants are located on the medial proximal portion of the tibia, medial of the tibial tuberosity and distal to the medial condyle. Figure 25 shows an image of the desired

implant location and a µCT reconstruction of the location after the implant was removed. A medical syringe was twisted into the desired hole location to create a small chamfer before using a 2 mm cobalt steel drill bit to drill the implant hole. After four weeks of recovery, animals were euthanized with CO_2 before excision of implants. Implants intended for mechanical testing were wrapped in gauze soaked in phosphate-buffered saline (PBS) before being stored in a -20C freezer. Fixed samples remained for longer than 48 hours to ensure sufficient fixation.
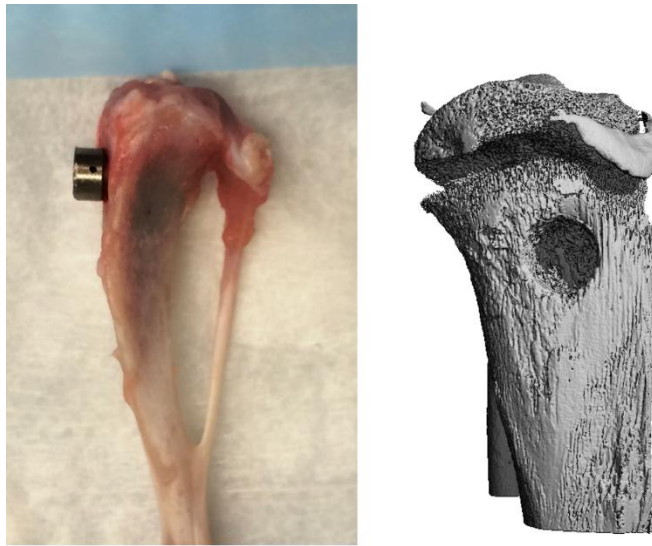
Figure 25: Target location of implant placement. Left: picture of explanted tibia. Right: µCT reconstruction of drilled hole

Characterization equipment and procedures

All *in vivo* samples were scanned in a Zeiss Metrotom 800 micro-computed tomography (µCT) machine at 80 V, 100 µA, 667 ms integration time, 8x gain, 3 image averaging and 1x1 binning. Scans were performed at an x position (distance from x-ray source to object)

of 60.0000 mm. This leads to a voxel size of 11.95 µm and spot size of 8 µm. All scans lengths were 1:44 hours, and frozen (non-fixed) samples were thawed for no longer than four hours. A sample holder (Figure 26) was made to orient implants vertically to minimize the voxel size at the specified distance, and also to reduce the amount of beam hardening artifact. 8-bit RGB image data were exported from the µCT and imported into SCANCO Medical microCT evaluation software for 3D analysis. A contoured volume of interest (VOI) of diameter 2.2 mm (10% larger than the implant diameter) was selected before segmentation of bone around the implant. Figure 27 shows the contour generation (top) and the segmentation process (bottom). In the contour selection, a green ring was drawn around the implant for the VOI selection, and thresholding distinguishes bone from voids during the segmentation process. Bone volume to total volume measurements were calculated from averaging the percent bone to total volume of exported µCT images for every slice of each scanned sample.
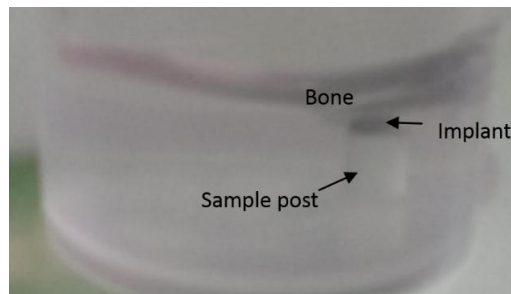
Figure 26: µCT Sample holder
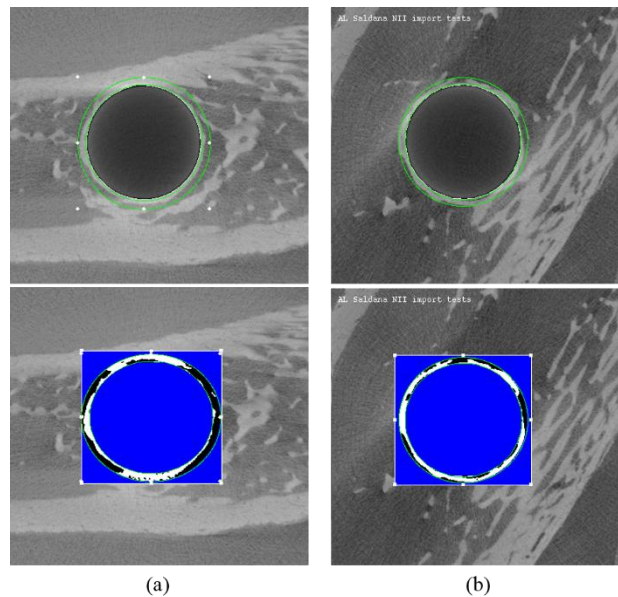
Figure 27: Greyscale slice with contoured VOI (green, above) and segmentation of bone around implant (white, below) for samples (a) 255R / T1, and (b) 256L / T4

Pullout testing

Six samples per group (total of 24 samples) underwent mechanical pull-out testing. Because these samples were not fixed and remain frozen to prevent tissue degradation, each of the samples went through exactly two freeze-thaw cycles. While any number of freeze-thaw cycles may be not preferred, the current inability to maintain -20C temperatures within the μCT scanner necessitates this freeze cycling. Similar to during scanning, samples were thawed at room temperature before pull-out testing. Pull-out testing was performed with a Bose EnduraTEC ELF 3200 uniaxial testing system using an Interface force transducer (model SMT 1-22) with a capacity of 22 lbf. Figure 28 shows an image of a sample being tested in the testing system. A piano wire was threaded through the through hole of the implant and clamped to the force transducer (not pictured, above). While the bone is fixed at the bottom of a metal cylinder, the piano pulls the

implant directly upwards through the center of the cylinder. Samples were preloaded to 0.5 N before pull-out testing was performed with a 10 Hz sampling rate with a pull-out rate of 0.02 mm/s. Data was saved and inspected for abnormalities, before measurements of maximum forces in MATLAB.
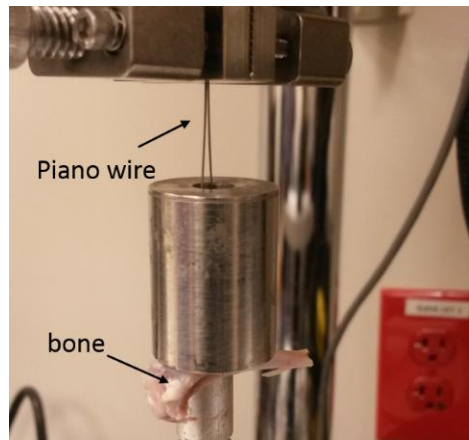
Figure 28: Mechanical pull-out testing system

3.3 Tribological testing configuration

Tribological tests were used to explore the effects of varying texture geometry on the frictional and wear properties of textured samples. Frictional properties were quantified by estimating the coefficient of friction (μ) and wear performance was determined by measuring wear volume. Tested specimens were fabricated from Aluminum 6061-T6 cylinders 25.4 mm in diameter and 9.525 mm thick. The tools as described above were used for roughing (0.005 mm/rev, 244 m/min, and 0.254 mm depth of cut) and finishing (0.005 mm/rev, 366 m/min, and 0.254 mm depth of cut) the test samples. For surface texturing, the modulation unit was set in a face-plunging MAT texturing orientation and

fed into the work face at a diameter of 17.78 mm to create the textured pass. An Iscar MIFR 8-1.60-0.80 carbide face grooving tool was used for texturing operations on all samples. Figure 29 provides a drawing of the insert and the accompanying dimensions [137, 139]. The manufacturing conditions used are provided in Table 7 and the measured surface roughness and texture geometry (e.g., depth, length, width) for each sample are provided in Table 8 in summarized form. Three texture depths of 7 µm, 12 µm, and 18 µm at 30 textures/rev were chosen because they span the useful range of modulation depths available without encountering geometric tooling constraints [138]. At 7 µm depth, a second group of samples was made with 50 textures/rev to understand the effect of texture density.
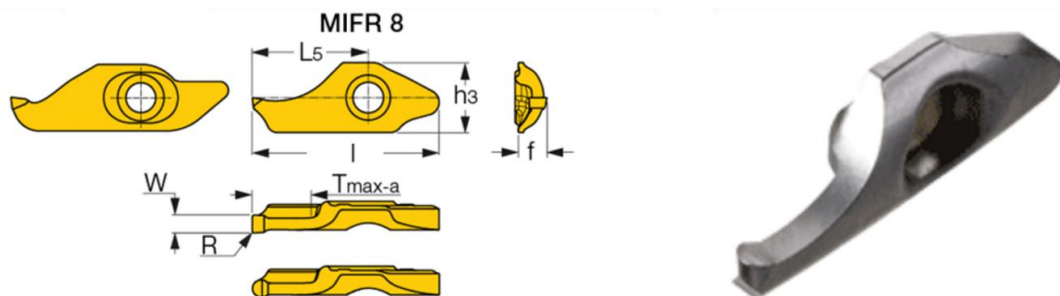
Figure 29: An Iscar MIFR 8-1.60-0.80 carbide face grooving tool with I=17.7 mm, W=1.60 mm, R=0.80 mm, f=2.6 mm, h3=6.5mm, Tmax=5.50mm, L5=11.00mm [139]

Table 7: Manufacturing conditions used for Al6061-T6 samples

Sample Description	f_m (Hz)	V_{pp} (V)	V_{off} (V)	a_p (mm)	h_0 (mm/rev)	f_w (Hz)
Untextured				0.254	0.005	366 m/min
7 µm	100	60	75			2
7 µm	60	60	75			2
12 µm	60	93	75			2
18 µm	60	136	75			2

Table 8: Summary of sample measurements

Sample Description	# samples	Average Ra (µm)	STD Ra (µm)	Average texture depth (µm)	STD texture depth (µm)	Average texture Length (mm)	STD texture Length (mm)	Average texture Width (mm)	STD texture Width (mm)
Untextured	9	0.018	0.003	no textures					
7 µm, 100 Hz	9	0.018	0.002	6.78	0.58	0.54	0.07	0.20	0.03
7 µm, 60 Hz	9	0.020	0.003	7.20	1.41	1.04	0.13	0.23	0.03
12 µm, 60 Hz	9	0.019	0.002	12.13	1.08	0.99	0.08	0.28	0.02
18 µm, 60 Hz	9	0.019	0.004	18.28	1.71	1.02	0.05	0.34	0.02

All samples were rinsed in acetone prior to characterization and wear testing. Surface roughness was measured using an Alpha-Step IQ Surface Profiler with 5000 µm scan length at 50 µm/s and sampling rate of 50 Hz and stylus force of 5.78 mg. Stereoscopic scans were performed on all samples using a Zygo NewView 200 interferometer to measure the texture depth of each sample with representative scans shown in Figure 30 and Figure 31. For interferometer scans, the flat plane was averaged and set to position z=0. A 5-point moving average was used to filter noise prior to using the global minimum value as the texture depth. 5 textures were measured per sample. Texture length and width measurements were measured using a Nikon Microphot-FX microscope with 4 length and width pairs measured per sample.
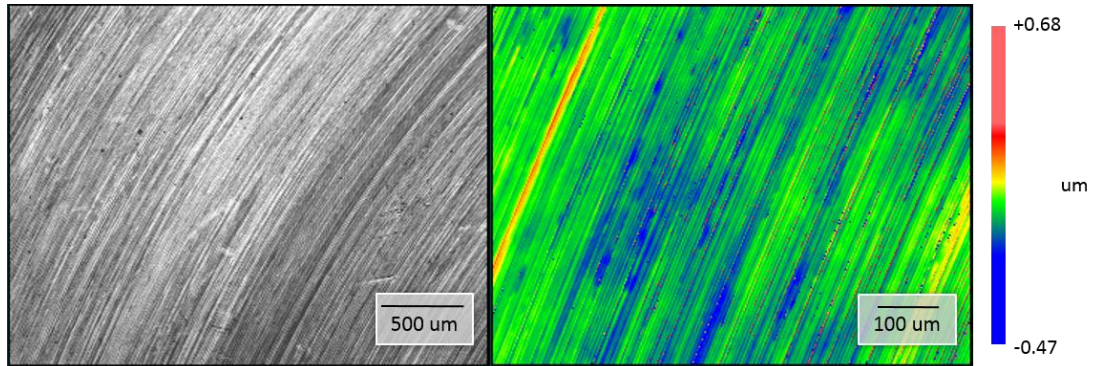
Figure 30: Stereoscopic scans of smooth samples in Al6061-T6. Samples are created at constant surface speed CSS = 34 m/min, h_0 = 0.003 mm/rev
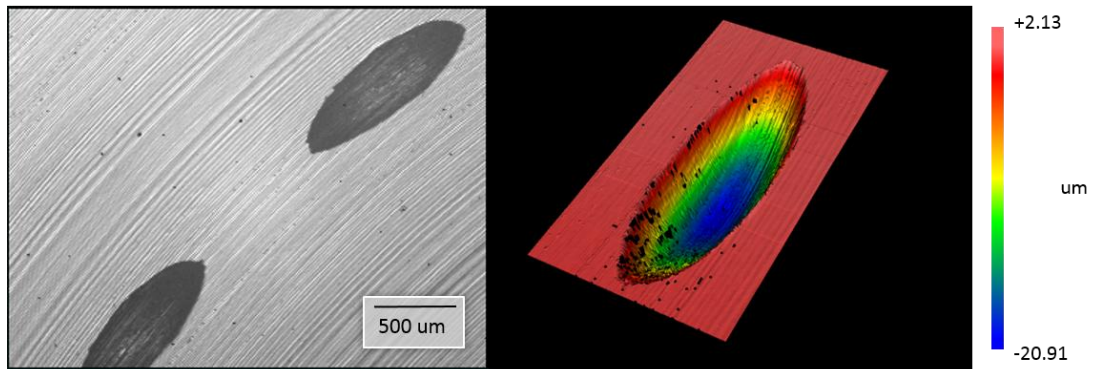
Figure 31: Representative stereoscopic scans of textured sample in Al6061-T6. This particular sample uses the following parameters: f_m = 60 Hz, f_w = 2 Hz, V_{pp} = 90 V

A pin-on-disk, rotary tribometer was used to characterize the friction and wear properties of test specimens and is pictured in Figure 32. The tribometer runs on a BLWRPG173S-24V-4000-R4.9 brushless DC planetary gearmotor, which is rated to 1.47 N-m up to a maximum speed of 500 RPM, which is more than 40x the torque that is expected to be seen during testing. A 2 mm diameter high speed steel pin (hardness C68) was precision ground and used for testing. Loads of varying weights may be placed on top of the pin to serve as normal loads during testing. In the present study, a 1 kg load

was placed atop a 2 mm steel wear pin. The 2 mm diameter pin resulted in a contact pressure of 3.12 MPa, assuming conformal contact conditions hold. Samples were tested at 100, 200, 300, and 400 RPM, this corresponding to surface speeds of 5.59, 11.17, 16.76, and 22.34 m/min, respectively. Sliding distance was maintained constant at 1000 meters for all trials, leading to test times that varied from 44 minutes (400 RPM) to 179 minutes (100 RPM). These test parameters are provided in Table 9. 0.5 mL of synthetic poly alpha-olefin oil (Synton PAO 40) lubrication were used to lubricate the wear area prior to testing and no additional lubricant was added during the duration of the test. The steel pin was visually examined and re-ground after each trial. The tribometer uses a KFG series general-purpose strain gauge and SCXI-1520 Universal Strain Gauge module to measure tangential forces during wear testing at a rate of 1 Hz. The coefficient of dynamic friction was determined by the ratio of the frictional force (tangential force) and the normal force (the mass placed on top of the wear pin). After wear testing, an optical microscope was used to visually inspect wear track width for all samples. The actual wear volume was found by using a Taylor-Hobson Talysurf surface profilometer to measure the wear profiles.
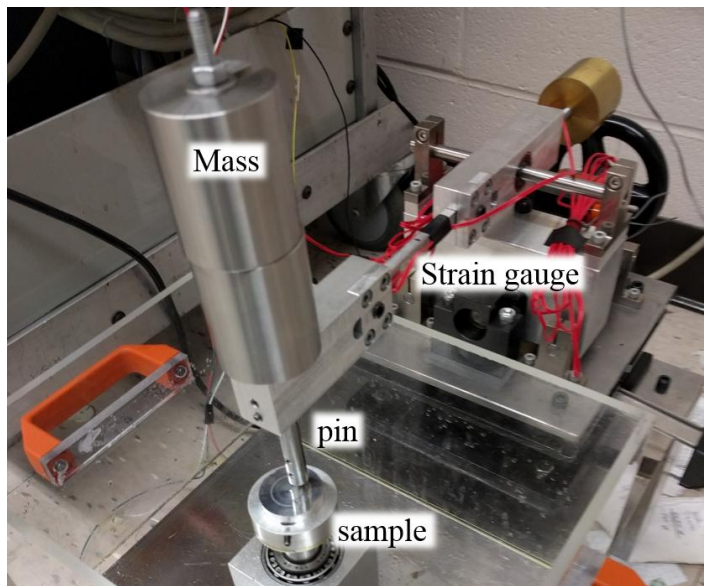
Figure 32: Pin-on-disk tribometer

Table 9: Test conditions for pin-on-disk wear testing

Sliding Distance (m)	RPM	Load (kg)	Contact pressure (MPa)	Pin diameter (cm)	Surface velocity (m/min)	Test time (min)
1000	100	1	3.123	2	5.59	179.03
1000	200	1	3.123	2	11.17	89.51
1000	300	1	3.123	2	16.76	59.68
1000	400	1	3.123	2	22.34	44.76

CHAPTER 4

RESULTS AND DISCUSSION

This chapter summarizes results of simulations and experiments designed to investigate the use of modulation-assisted texturing for orthopedic and tribological applications. First, results of simulations for sliding-type MAT texturing configurations are presented. Second, experiments for exploring effects of sliding-type MAT textures on osseointegration performance in orthopedic fixation applications is presented and discussed. Last, experiments for investigating the effects of plunging-type MAM textures on tribological performance are summarized.

4.1 Sliding-type MAT configuration simulation and experimentation

In this section, a MATLAB model is used to understand the surface generation process in sliding-type MAT. The effects of controllable modulation and machining parameter inputs on texture morphology are presented. The simulated data are then compared to experimental results of texturing experiments.

4.1.1 Sliding-type MAT simulation results

The nature of the surfaces generated in sliding-type MAT share similarities to those produced in conventional threading operations. In a conventional threading operation, important determinants of surface topography include tool radius, feed, and depth-of-cut. The controlled manipulation of these variables changes thread characteristics including lead, included angle, thread angle, and thread depth. Controllable machining parameters such as surface speed, driven by spindle frequency and workpiece diameter, affect surface topography. The sliding-type textures simulated in this present study are not only

affected by these same variables, but are also affected by the modulation frequency and modulation amplitude used in the MAT device platform.

Figure 33 summarizes the effects of changing the ratio of modulation amplitude to machining feed on the resulting machining toolpaths. Each panel is represented as an unraveled cylindrical workpiece, wherein the x-axis is the circumferential position of the workpiece and the y-axis is the axial position along the length of the workpiece. In a conventional machining operation, the toolpaths are present in the form of parallel sloped lines which represent the helical pattern formed along the work surface whose offsets are determined by the machine feed h_0. In modulation-assisted machining, a sinusoidal signal is superimposed on these feed lines depending on the modulation conditions used. The modulation conditions shown in the figure correspond to a rotational frequency of $f_w = 1$ Hz and a modulation frequency of $f_m = 50.5$ Hz, yielding a perfectly out-of-phase condition given by $\varphi = \pi$. From left to right in the figure, the ratio of the machining feed to the modulation amplitude increases from $A/h_0 = 1/8$ to $A/h_0 = 2$. From the figure, it is clear that increasing the A/h_0 ratio brings the peaks of the sinusoidal toolpath closer together and that consecutive machining passes intersect at $A/h_0 = 1/2$. The resulting surface topography is highly dependent on the tooling geometry and depth-of-cut used in surface texturing. Below each panel are corresponding three-dimensional images that provide a view of the predicted surface topography considering a tool with radius of $R = 0.50$ mm and a depth-of-cut of $a_p = 58.1$ μm. From the surface topography simulations, increasing the A/h_0 ratio causes interaction of multiple toolpaths and the creation of more complex surface features.
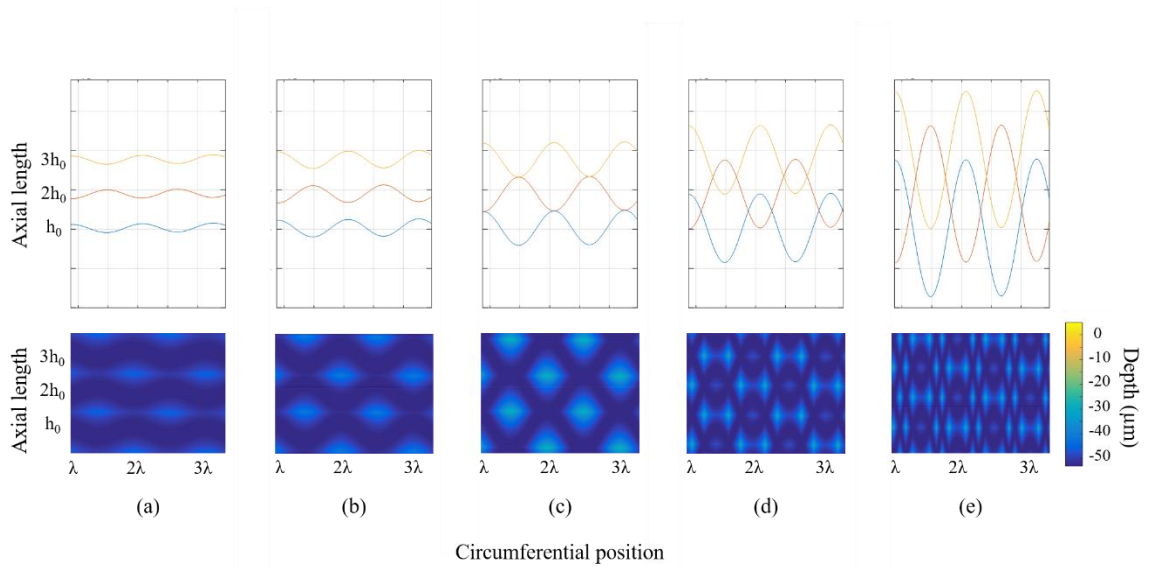
Figure 33: Effects of amplitude/feed on tool paths (top) and resulting 3D textures (bottom). $h_0=2A$ is the intersection condition. (a) $A/h_0=1/8$, (b) $A/h_0=1/4$, (c) $A/h_0=1/2$, (d) $A/h_0=1/1$, (e) $A/h_0=1/0.5$; A varies while h_0 remains constant at 43.5 μm, $f_m=50.5$ Hz, $f_w=1$ Hz, d=7.62 mm, $a_p=58.1$ μm

Complementary to the coupled effects of machining feed and modulation amplitude on toolpaths and resulting surface topography, the ratio of the modulation frequency (f_m) and spindle frequency (f_w) control the phase offset of each toolpath and the final texture morphology. Figure 34 summarizes the effects of phase shift φ (e.g., variable f_m/f_w) when $h_0=2A$. The plots once again represent the surface of an unraveled cylinder with the tool tracing continuously along the workpiece surface. The ratio f_m/f_w decreases from 51 to 50 Hz (left to right) in increments of 0.25 Hz. The corresponding phase shift in the panels is given by φ = [0, 3π/2, π, π/2, 0]. At a phase shift of φ = 0, the toolpaths are perfectly in-phase. The resulting topography is a set of parallel, but wavy grooves on the work surface. At intermediate phase shift values of φ = [3π/2, π/2] the toolpaths are neither perfectly in-phase or out-of-phase, resulting in a surface topography

70

of diagonal micro-features whose pitch relative to the work surface is determined by the absolute value of the phase angle. Finally, at a phase shift of $\varphi = \pi$ the toolpaths are perfectly out-of-phase resulting in the intersection of consecutive tool passes at relative peaks and valleys of the sinusoidal motion. The subsequent surface topography is given by the intersection of out-of-phase grooves on the work surface, this resulting in discrete micro-features protruding from the work surface.
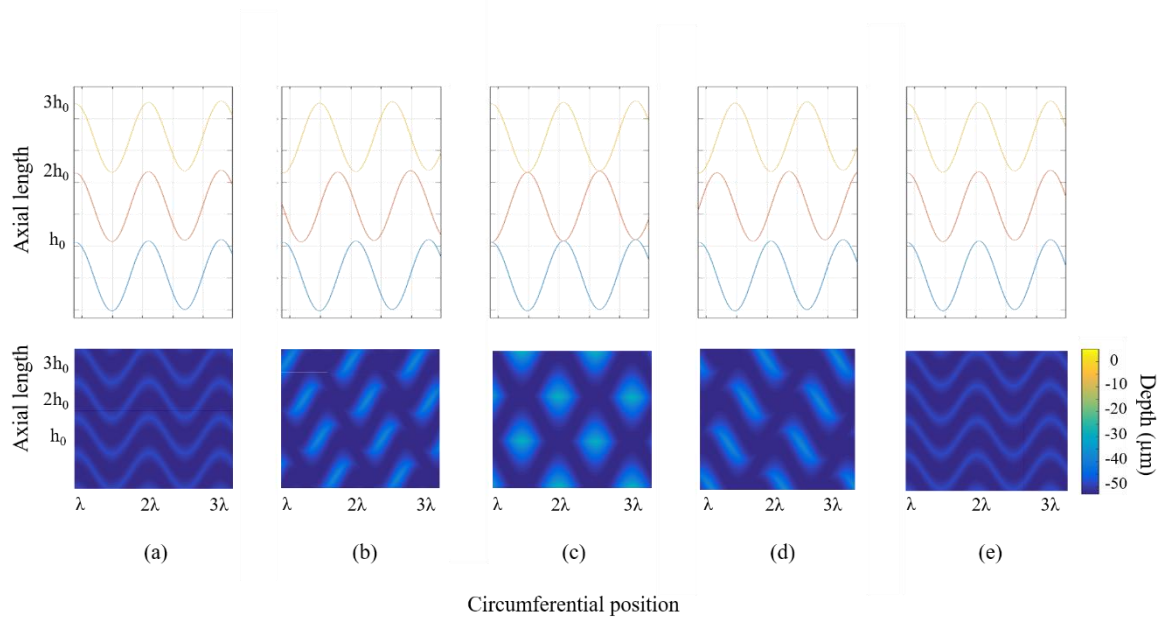
Figure 34: Effects of phase change on toolpaths and resulting 3D textures when $h_0 = 2A$. (a) $\varphi=0$ ($f_m=51$ Hz), (b) $\varphi=3\pi/2$ ($f_m=50.75$ Hz), (c) $\varphi=\pi$ ($f_m=50.5$ Hz), (d) $\varphi=\pi/2$ ($f_m=50.25$ Hz), (e) $\varphi=0$ ($f_m=50$ Hz); $f_w=1$ Hz, $A=21.75$ μm, $h_0=43.5$ μm, $d=7.62$ mm, $a_p=58.1$ μm

In addition to the effects of the ratio of the modulation frequency (f_m) and spindle frequency (f_w) on phase offset and surface texture morphology, the absolute value of f_m/f_w also determines the relative size of the surface features. Figure 35 shows the effects that varying the ratio f_m/f_w have on feature size for perfectly out-of-phase conditions given by $\varphi = \pi$. In the figure, the ratio f_m/f_w is varied by a factor of approximately 4 by

71

increasing f_m from 50.5 Hz to 200.5 Hz while spindle frequency and phase angle were set constant at $f_w = 1$ Hz and $\varphi = \pi$. From the panel of plots, increasing the f_m/f_w yields an increased number of sinusoidal cycles along the circumference of the workpiece in a single pass, effectively reducing the relative length of the surface features along the workpiece circumference. Further, a direct relationship between the ratio f_m/f_w and the length of the surface features can be found. The wavelength of the sinusoidal toolpath (and therefore feature length) is inversely related to the ratio f_m/f_w. It should be noted that this trend also holds across all phase shift conditions.
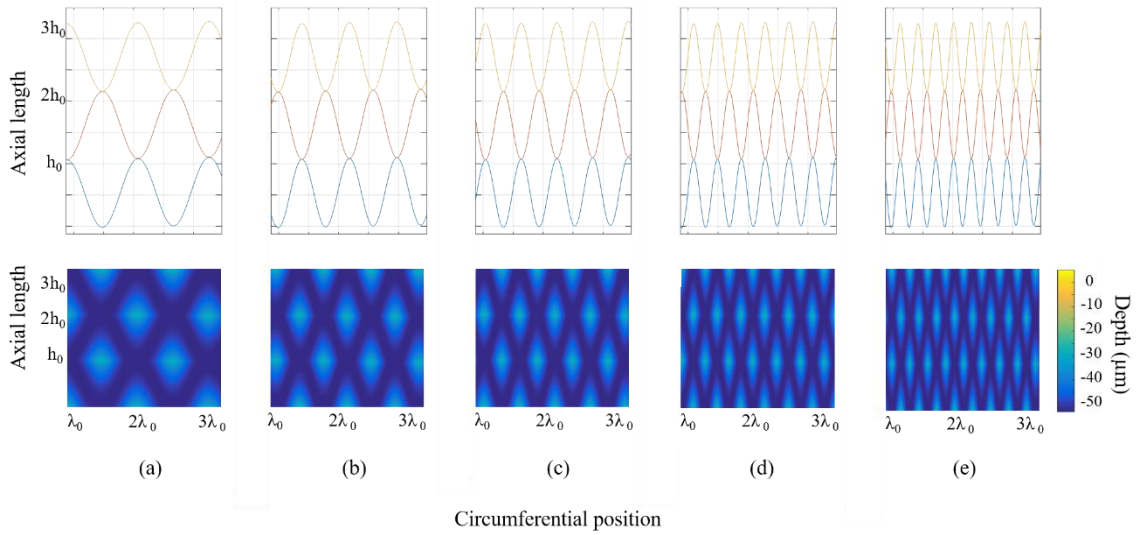
Figure 35: Effects of f_m/f_w changes on toolpaths and resulting 3D textures when $h_0 = 2A$. (a) f_m/f_w=50.5/1, (b) f_m/f_w=75.5/1, (c) f_m/f_w=100.5/1, (d) f_m/f_w=150.5/1, (e) f_m/f_w=200.5/1; A=21.75 μm, h_0 =43.5 μm, d=7.62 mm, a_p=58.1 μm

Figure 36 shows the effects of phase shift φ and ratio f_m/f_w on feature height h. From the figure, there are two notable trends observed between these parameters. First, the ratio f_m/f_w is seen to affect the relative lengths of the features. As the ratio is increased

72

from 50 to 200, the feature length is shortened proportionately. Further, the ratio f_m/f_w does not affect the feature height across the range of phase shift φ used. Second, it is observed that the phase shift φ directly influences the feature height. In this regard, the height of the features varies from h = [11.4, 43.0, 58.1, 43.0] μm as the phase shift angle changes from φ = [0, $\pi/2$, π, $3\pi/2$], respectively. In this regard, the highest features correspond to out-of-phase conditions and the shortest features correspond to in-phase conditions.
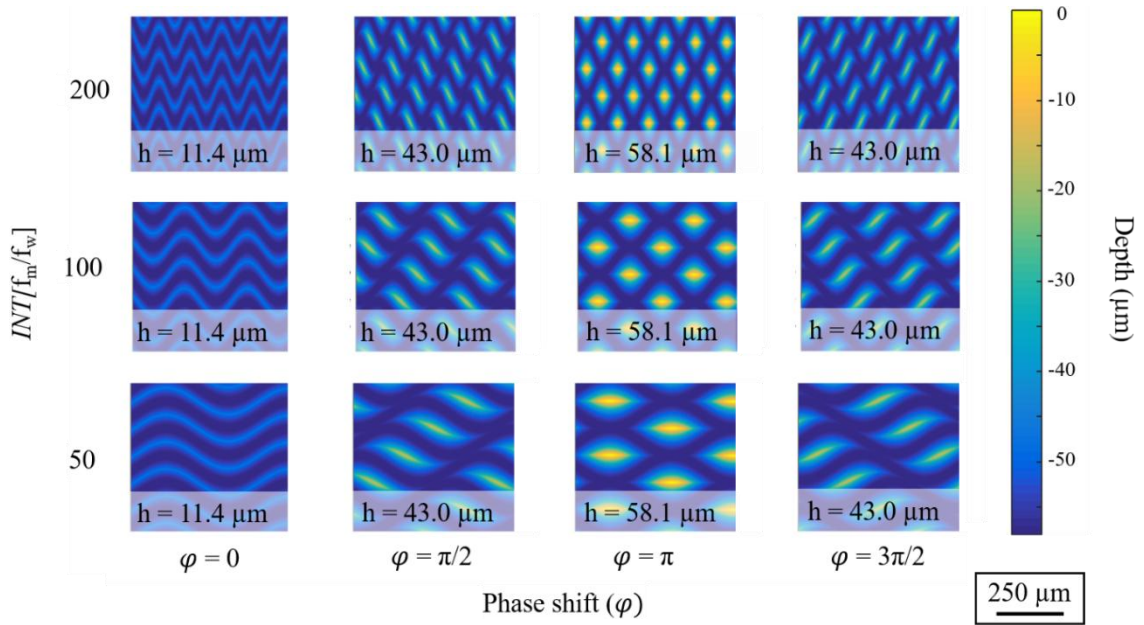
Figure 36: The effects of phase and frequency ratio on feature height (h) for an example texture with f_w=1, f_m as specified above, A=31 μm, h_0=63.5 μm, d=7.62 mm, a_p=-58.1 μm

The general effects of controllable texturing parameters (e.g., φ, A/h_0) and the surface topography are summarized in Figure 37, where φ is given by the ratio f_m/f_w. Also superimposed on the figure is a boundary indicating the critical conditions for

intersection of successive toolpaths given by $A/h_0 = 1/2 \sin\left(\frac{\varphi}{2}\right)$. The boundary shows that the minimum A/h_0 ratio needed for intersection of successive toolpaths occurs for out-of-phase conditions given by $\varphi = \pi$. As the phase deviates from this inflection point, the critical A/h_0 ratio increases and is infinite at in-phase conditions given by $\varphi = [0, 2\pi]$. 3D surface plots are overlaid on the intersection criterion plot to show the relationship between φ (e.g., f_m/f_w) and A/h_0 for a range of inputs and the implications of the intersection of the successive toolpaths. At conditions below and outside the boundary, toolpaths do not fully intersect with subsequent passes and result in the creation of semi-continuous surface textures. For parameter combinations of f_m/f_w and A/h_0 coincident or above the boundary, successive toolpaths intersect and result in the creation of discrete surface textures. At more aggressive texturing conditions characterized by larger A/h_0 result in the generation of somewhat more complex geometries due to the impact of having multiple toolpaths overlap on the work surface. It should be noted that, from a practical perspective, physical system limitations preclude the use of amplitudes that are larger than of the maximum travel of actuators or exceed performance capability of the amplifier system, as well as spindle frequencies wherein adequate precision of rotational position cannot be maintained.
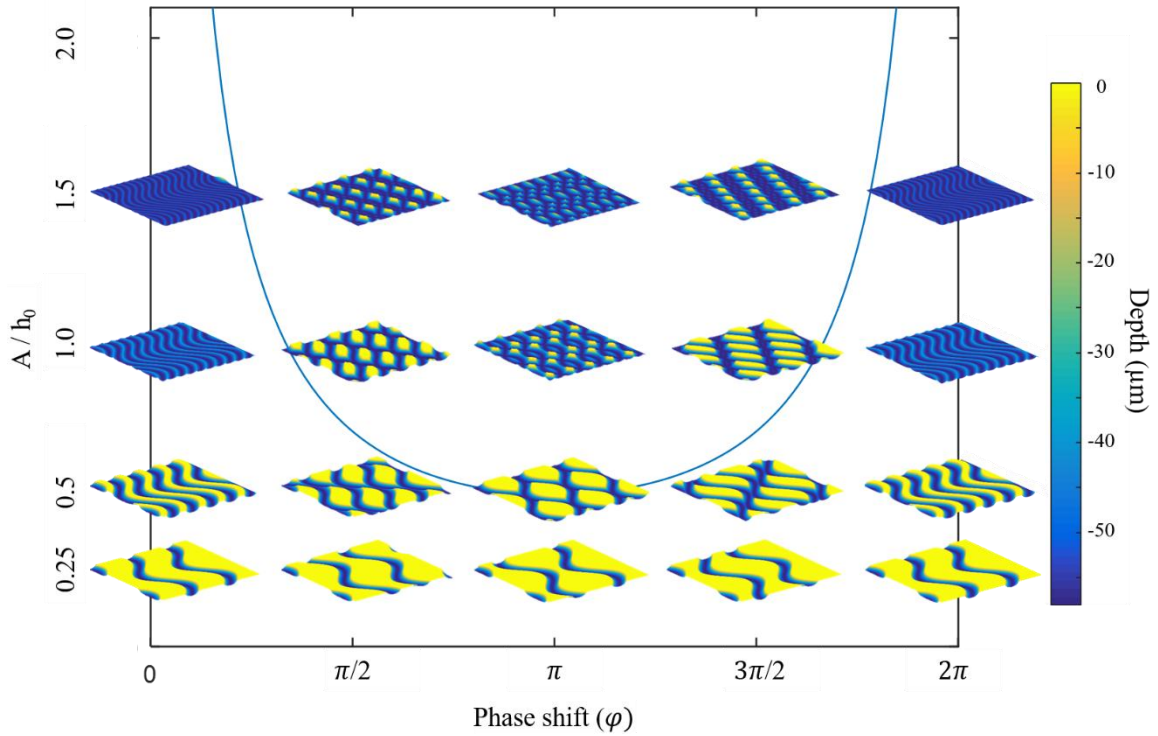
Figure 37: Tool path intersection conditions for outer diameter sliding samples. Parameters were chosen for visual clarity and the constants are as follows: $f_w=2$ Hz, A=75 µm, d=17.5 mm, $a_p=-44$ µm. The variables were $f_m=60$, 60.5, 61, 61.5, 62 Hz; and $h_0=300$, 150, 75, 50 µm.

Variability in input modulation and machining parameters also can affect characteristics of the resulting surface textures. Table 10 provides measurements of the mean and standard deviation of modulation frequency and amplitude. The effects of this input variability on texture morphology were simulated and compared below to determine the predictive capability of the developed MATLAB model. Table 11 - Table 14 show the effects of variability in modulation system inputs (e.g., amplitude, frequency) on the resultant distribution of geometric parameters (e.g., length, width, and height) of the surface textures. In the tables, ideal values represent parameter inputs with

75

exact mean values with zero deviation. In contrast, the recorded values were obtained from actual measurement data fitted using a normal distribution. These data points constitute the simulated values and are randomly drawn and used as inputs for calculations.

Table 10: Mean and standard deviation of modulation frequency and amplitude measurements

Sample (φ)	Frequency ($\mu \pm \sigma$, Hz)	Amplitude ($\mu \pm \sigma$, μm)
1 ($\varphi = 0$)	100.00 ± 0.19	31.40 ± 0.04
2 ($\varphi = \pi/2$)	100.25 ± 0.19	30.18 ± 0.03
3 ($\varphi = \pi$)	100.50 ± 0.18	31.12 ± 0.04
4 ($\varphi = 3\pi/2$)	100.75 ± 0.16	30.3 ± 0.06

Table 11: Inputs for mathematical $\varphi = 0$ (in phase) model and resulting output comparisons. Note that all length dimensions are in microns.

	Inputs		**Outputs**		
Sample type	Amplitude ($\mu \pm \sigma$, μm)	f_m ($\mu \pm \sigma$, Hz)	Length ($\mu \pm \sigma$, μm)	Width ($\mu \pm \sigma$, μm)	Height ($\mu \pm \sigma$, μm)
Ideal values	31.40 ± 0	100.00 ± 0		62.80 ± 0	11.37 ± 0
Recorded values	31.40 ± 0.04	100.00 ± 0.19		62.80 ± 0.08	11.37 ± 0
Simulated values	31.40 ± 0.04	100.00 ± 0.19		62.80 ± 0.08	11.37 ± 0

Table 12: Inputs for mathematical, phase = π/2, model and resulting output comparisons. Note that all length dimensions are in microns.

	Inputs		Outputs		
Sample type	Amplitude (μ ± σ, μm)	f_m (μ ± σ, Hz)	Length (μ ± σ, μm)	Width (μ ± σ, μm)	Height (μ ± σ, μm)
Ideal values	30.18 ± 0	100.25 ± 0	298.49 ± 0	123.86 ± 0	41.96 ± 0
Recorded values	30.18 ± 0.03	100.25 ± 0.19	299.05 ± 0.46	123.85 ± 0.06	42.23 ± 0.23
Simulated values	30.18 ± 0.03	100.25 ± 0.19	298.58 ± 4.60	123.86 ± 0.06	41.79 ± 2.09

Table 13: Inputs for mathematical, phase = π (out-of-phase) model and resulting output comparisons. Note that all length dimensions are in microns.

	Inputs		Outputs		
Sample type	Amplitude (μ ± σ, μm)	f_m (μ ± σ, Hz)	Length (μ ± σ, μm)	Width (μ ± σ. μm)	Height (μ ± σ, μm)
Ideal values	31.12 ± 0	100.50 ± 0	238.20 ± 0	125.74 ± 0	58.89 ± 0
Recorded values	31.12 ± 0.04	100.50 ± 0.18	238.19 ± 0.40	125.74 ± 0.07	58.89 ± 0.06
Simulated values	31.12 ± 0.04	100.50 ± 0.18	238.21 ± 6.35	125.74 ± 0.08	58.82 ± 0.12

Table 14: Inputs for mathematical, phase = 3π/2, model and resulting output comparisons. Note that all length dimensions are in microns.

	Inputs		Outputs		
Sample type	Amplitude (μ ± σ, μm)	f_m (μ ± σ, Hz)	Length (μ ± σ, μm)	Width (μ ± σ. μm)	Height (μ ± σ, μm)
Ideal values	30.63 ± 0	100.75 ± 0	297.01 ± 0	124.78 ± 0	42.51 ± 0
Recorded values	30.63 ± 0.06	100.75 ± 0.16	296.69 ± 0.76	124.77 ± 0.12	42.26 ± 1.81
Simulated values	30.63 ± 0.06	100.75 ± 0.16	296.93 ± 8.79	124.76 ± 0.12	42.30 ± 1.95

From the measured and simulated data, several observations can be made regarding influence of parameter variability on the resulting textures. First, while under identical conditions of V_{pp}=112 V, amplitude measurement is seen to vary up to 1 μm between test conditions (30.18 μm for φ=π/2 to 31.12 μm for φ=π), which can lead to width inaccuracies of up to 2% throughout the four simulated conditions. However, the standard deviation of recorded amplitudes within each particular condition never exceeds 0.1% of the mean values across the conditions investigated, resulting in absolute amplitude errors of approximately 0.05 microns. For the most variable φ=3π/2 texture, this variability in amplitude translates to width deviations of no more than 0.12 μm. As the texture height is also directly related to the width of the texture, this small variability in amplitude also explains the observed small deviations in texture height. The modulation frequency errors were observed to have standard deviations less than 0.2%. While the phase of textures does not depend on the magnitude of the frequency ratio and rather depends on the fractional portion of the ratio, the ~0.2% deviations in frequency ratios have little ramification on total feature length. Table 15 summarizes the ideal verse simulated measurements and calculates the percent error, showing that the errors in all geometric characteristics (e.g., length, width, height) due to expected variation in modulation parameters can be expected to be less than 0.5% for all feature geometries. It is interesting to note that the error in height for φ = π/2 and φ = 3π/2 are larger than the other conditions. Height is a function of vertical distance between consecutive toolpaths, which is a result of amplitude and phase shift. It is simplest to explain this finding by explaining why height shows less error in the other test cases. Complete in-phase height shows no variation because the width of the feature (machine feed) is assumed to be ideal in this simulation. Complete out-of-phase heights, however exhibit minimal height errors

compared to the other out-of-phase conditions. This is because the minimum rate of change (slope) of a toolpath occurs at the inflection points of the sinusoidal toolpath (i.e. max/min of sine wave). These inflection points correspond with the maximum vertical distance in each surface feature. The height values of these complete out-of-phase features as a result are more resistant to inaccuracies in phase (f_m/f_w) compared to the intermediate out-of-phase textures ($\varphi = \pi/2$, $\varphi = 3\pi/2$).

Table 15: Percent error of mean values of normal fit verses ideal values

Sample (φ)	Ideal length (µm)	Simulated length (µm)	Ideal width (µm)	Simulated width (µm)	Ideal height (µm)	Simulated height (µm)
1 ($\varphi = 0$)			62.80	62.80	11.37	11.37
% error			0.00%		0.00%	
2 ($\varphi = \pi/2$)	298.49	298.58	123.86	123.86	41.96	41.79
% error	0.03%		0.00%		0.41%	
3 ($\varphi = \pi$)	238.20	238.21	125.74	125.74	58.89	58.82
% error	0.00%		0.00%		0.10%	
4 ($\varphi = 3\pi/2$)	297.01	296.93	124.78	124.76	42.51	42.30
% error	0.00%		0.02%		0.49%	

The statistical distributions for the surface texture geometry (e.g., length, width, height) from Table 11 - Table 14 is presented graphically for each of the four experimental conditions in Figure 38. Note that the height does not have a variation in Table 11 because the only variable in the study that affects height for in-phase textures is feed, which is assumed to hold ideal values, with accuracy much greater than that of the modulation device. These histograms use the measured modulation frequencies as inputs, as opposed to the fitted normal distribution of the frequencies. It is first important to note

that the frequency distribution, while showing accurate means, is rejected at the 5%
significance level in a one-sample Kolmogorov-Smirnov normality test. Frequencies are
biased towards either side of the mean by about 0.25 Hz and show a relative minimum at
the target frequency value. As expected with a non-normally distributed input, the outputs
are also rejected by the Kolmogorov-Smirnov test at the 5% significance level. In spite of
this observation, the relative spread of data for each of the simulated conditions can be
observed. Here it is apparent that length, width, and height deviations of the $\varphi=3\pi/2$ case
is larger than the other conditions. Saying that, standard deviations of the simulated data
represent 0.3%, 0.1%, and 4.3% of the mean length, width, and height values,
respectively, as reported in Table 16. This relatively larger variation in output values is
caused by the marginally larger amplitude deviation (0.2%) compared to other samples
(~0.1%).
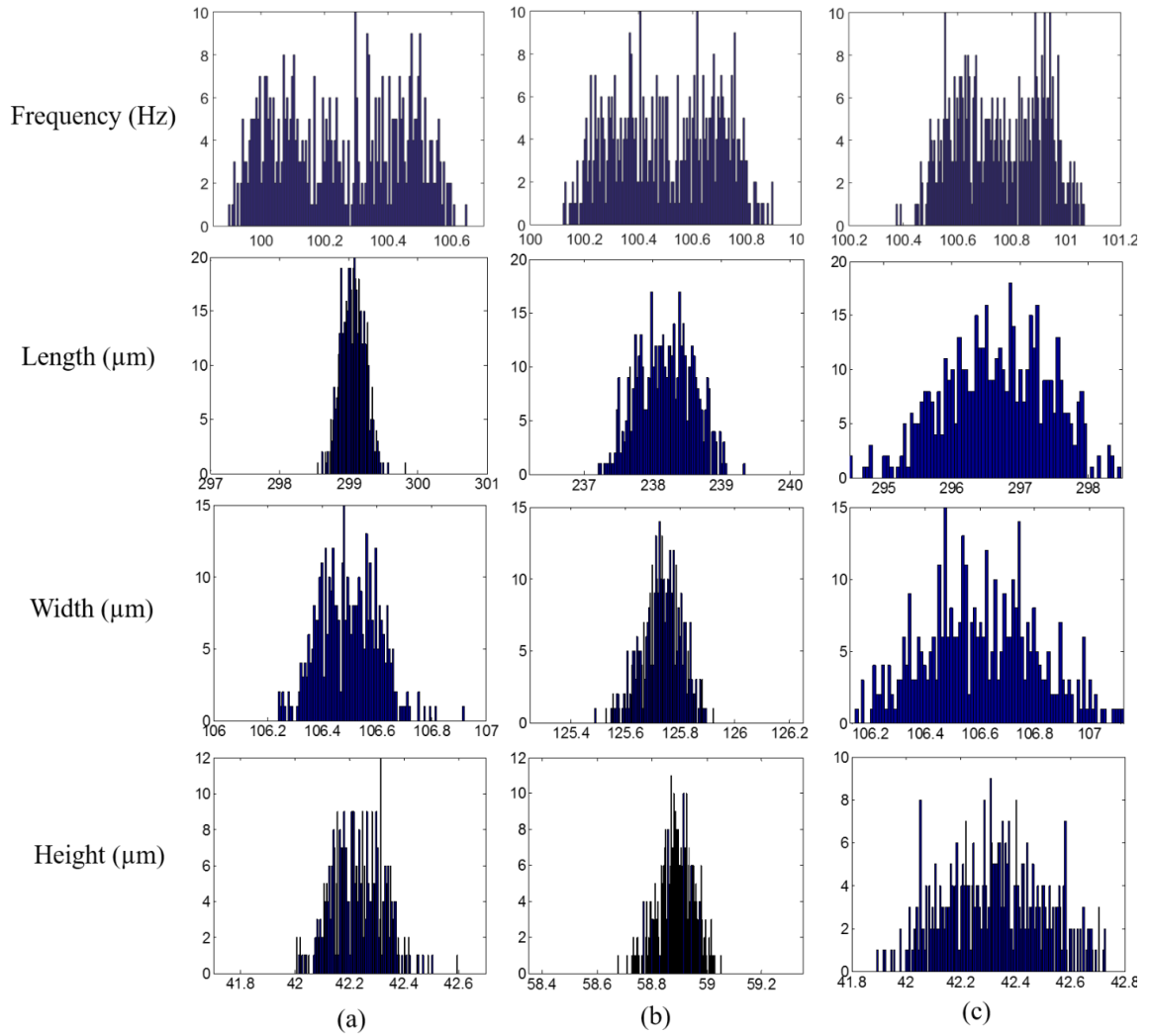
Figure 38: Recorded frequency, resulting length, width, and height distributions for phase shifts (a) $\pi/2$, (b) π, and (c) $3\pi/2$. Y-axis values are quantity, while x-axis values are labeled in the left-most column.

Table 16: Mean, standard deviation, and standard deviation as percent of mean of simulated measurements using recorded f_m and A data

Sample (φ)	mean length (µm)	std length (µm)	mean width (µm)	std width (µm)	mean height (µm)	std height (µm)
1 (φ = 0)			62.80	0.08	11.37	0.00
% of mean			0.13%		0.00%	
2 (φ = π/2)	299.05	0.46	123.85	0.06	42.23	0.23
% of mean	0.15%		0.05%		0.54%	
3 (φ = π)	238.19	0.40	125.74	0.07	58.89	0.06
% of mean	0.17%		0.06%		0.10%	
4 (φ = 3π/2)	296.69	0.76	124.77	0.12	42.26	1.81
% of mean	0.26%		0.10%		4.28%	

4.1.2 Sliding-type MAT configuration experimental results

The experimental measurements of the machined feature morphology are shown in the interferometer scans provided in Figure 39. Panels (a) – (d) show a representative scan for each of the features, with blue representing into the page and green representing out of the page. Macroscopically, the features do not exhibit high levels of variation and show the uniformity of the toolpaths on the circumference of machined samples. Features are discrete and clearly show differences upon changing the phase. In terms of individual features on the work surface, burr formation was observed for each of the test conditions. The effects of burr are most apparent near the peaks of the surface features, presumably due to fact that these peaks represent the extremities of the tool-work contact. Another

observation that can be seen in panel (a) are three banded high segments oriented along the workpiece axial direction near the peaks of each sinusoidal pass. Periodicity of these regions are consistent with tool deflection occurring when the tool is fully extended on the forward advance of its sinusoidal motion.
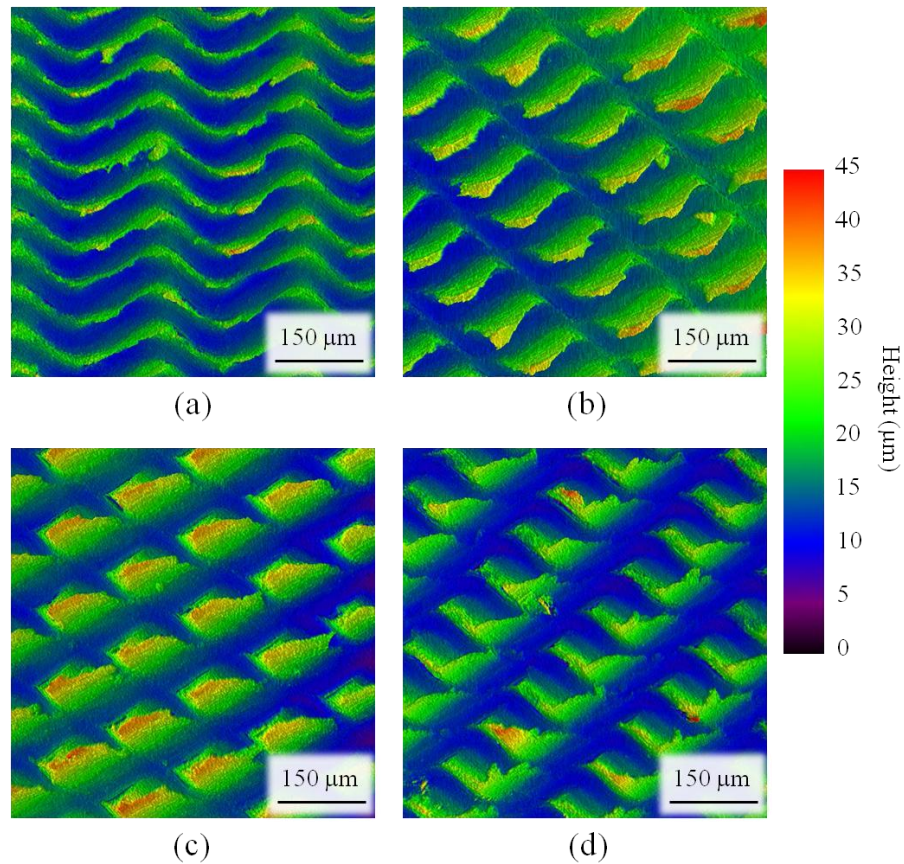
Figure 39: Stereoscopic scans of sliding textures of varying phase: (a) φ=0, (b) φ=π/2, (c) φ=π, (d) φ=3π/2

Figure 40 compares optical images with simulated textures under the same conditions. Qualitatively, the machined textures show quite similar characteristics as predicted by the MATLAB simulations. Table 17 summarizes the measured and predicted geometric characteristics of these textures and Table 18 summarizes the relative error in the predicted values. In general, the experimental measurements match well with predicted simulations for length and width measurements with errors approximately equal to or less than 5% of the mean value. However, the predicted values differ greatly from the experimental measurements regarding texture height. For all samples, the measured height was less than the expected height and for samples 2-4 (with height errors greater than 40%), the maximum measured height achieved was limited to between $20 - 25$ µm. This maximum feature height is likely seen because at a certain height, the discrete features no longer are able to withstand the side-flow from the cutting tool, causing the micro-feature to yield and ultimately fracture. The disparity between the width and height values signifies a limitation of the proposed geometric model that can be explained by the deformation process occurring at the peaks of the surface texture. An improved model that accounts for material properties is necessary prior to the successful simulation of texture behavior.
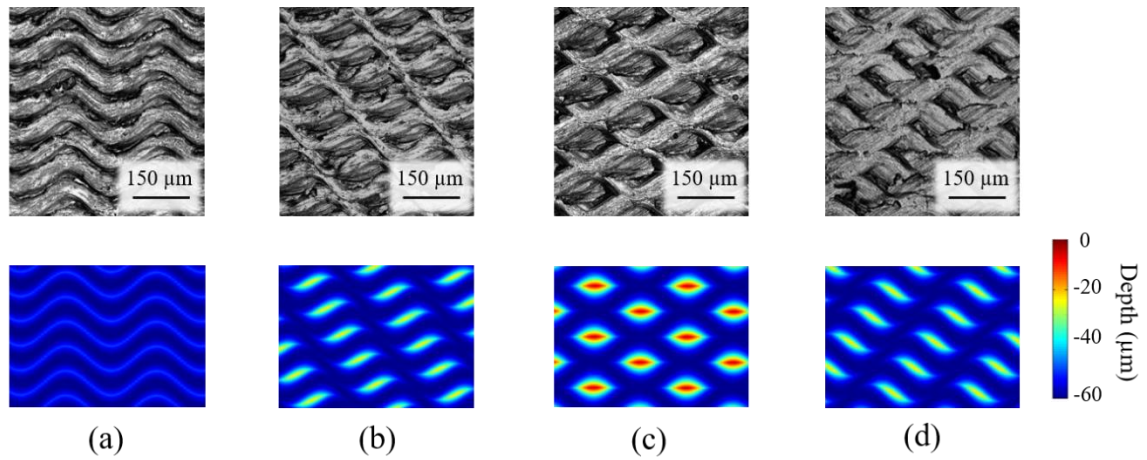
Figure 40: Comparison of experimental sliding samples and simulated samples under 4 phase transformations. The simulated samples use the recorded f_m and A values, and use ideal values for f_w=1 Hz, h_0=63.5 μm, d=7.62 mm, a_p=-63.5 μm. Each panel corresponds to a separate phase shift with separate conditions: (a) φ=0, f_m=100.0000 Hz, A=31.432 μm, (b) φ=π/2, f_m=100.2472 Hz, A=30.197 μm, (c) φ=π, f_m=100.5036 Hz, A=31.095 μm, (d) φ=3π/2, f_m=100.7508 Hz, A=31.631 μm

Table 17: Expected verses actual measurements of 4 representative MAM sliding samples

Sample (φ)	Expected Length (μm)	Measured Length ± σ (μm)	Expected Width (μm)	Measured Width ± σ (μm)	Expected Height (μm)	Measured Height ± σ (μm)
1 (φ = 0)			62.80	62.84 ± 1.49	11.37	10.95 ± 1.75
2 (φ = π/2)	298.49	295.73 ± 7.53	123.86	116.78 ± 2.10	41.96	17.99 ± 3.69
3 (φ = π)	238.20	234.02 ± 4.62	125.74	127.19 ± 3.21	58.89	22.60 ± 1.49
4 (φ = 3π/2)	297.01	292.34 ± 3.29	124.78	129.04 ± 6.70	42.51	25.83 ± 1.26

85

Table 18: Percent error of expected verse actual measurements of 4 representative MAM sliding samples

Sample (φ)	% Error		
	Length	Width	Height
1 (φ = 0)		0.06%	3.69%
2 (φ = π/2)	0.92%	5.72%	57.1%
3 (φ = π)	1.75 %	1.15%	61.6%
4 (φ = 3π/2)	1.57%	3.41%	39.2%

Parameter selection and machinability

An infinite number of parameter combinations can be selected in the developed MATLAB model, however transitioning from computer simulations to physical experiments opens a number of discussions. Tools used for sliding-type MAT, for example, have inherent limitations because of flank drag (back angle drag) issues and because cuts are often not deep enough to allow for ideal cutting conditions. Figure 41 shows one example of the effects of the flank drag. Flank drag occurs when modulation causes tools to have feed-direction displacement at an angle greater than the tool clearance angle. This undesirable machining condition is characterized by difficult to predict, sawtooth-like features with substantial burr formation caused from tool ploughing. Though custom tools may be made, large clearance angles (i.e. greater than 75°) are impractical even for research purposes because of the negative effects that such large clearance has on tool strength. This physical limitation may be alleviated in the future with specialized tooling using stronger materials, including specially-ground PCD and diamond tools as opposed to the currently-used carbide threading insert. In terms of machinability, the relatively low speed of the texturing operation may contribute to burr formation on the surface textures. Low spindle rotation frequencies in the range of 1-2 Hz

were utilized in the present work due to the limited frequency response of the motion control platform. Figure 42 shows the effects of roll-over burr formation in the case of an out-of-phase modulation condition with f_m=100 Hz, f_w=4 Hz, h_0=0.071 mm/rev, V_{pp}=112 V for a workpiece with 2 mm diameter, resulting in a surface cutting speed of 1.5 m/min. This behavior may be addressed by using increased surface cutting speed which would theoretically decrease burr formation.
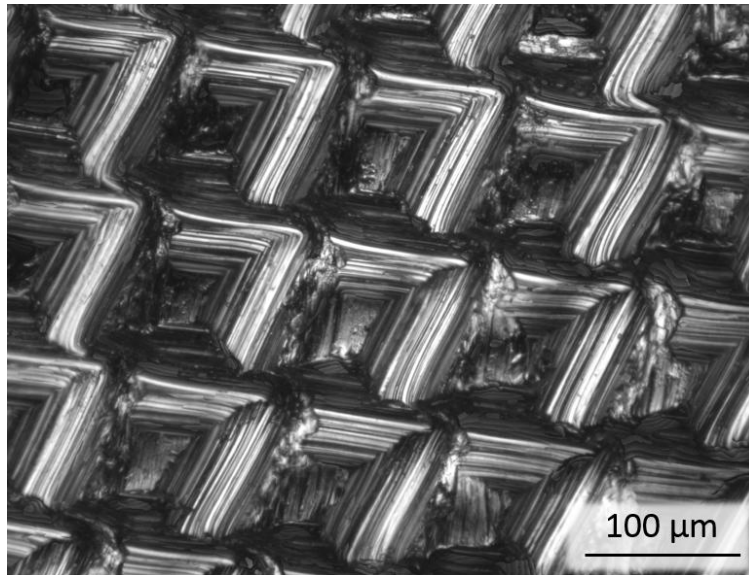
Figure 41: Relief angle drag example during complete out-of-phase machining of 2 mm diameter CP Ti with f_m=121.5 Hz, f_w=3Hz, h_0 = 0.076 mm/rev, Vpp=130 V at 0.076 mm depth-of-cut
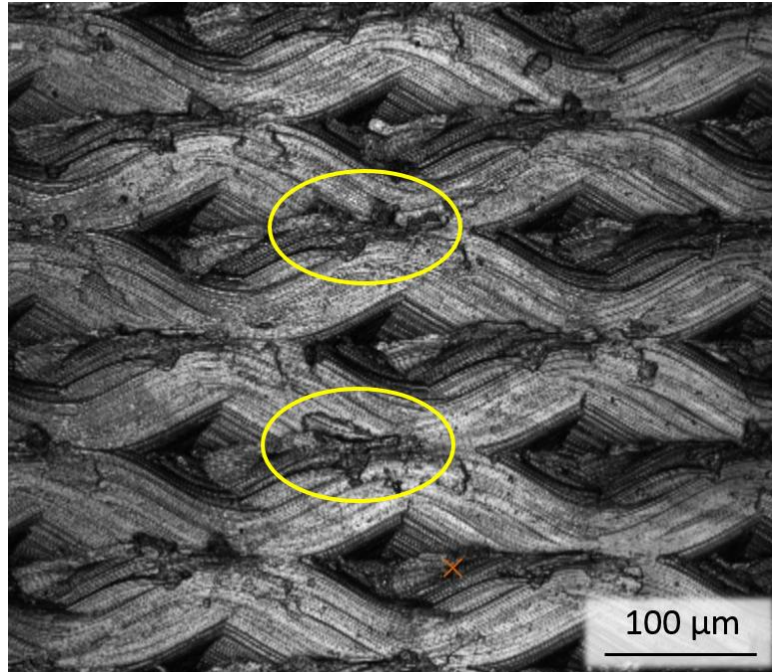
Figure 42: Burr formation during the complete out-of-phase machining of CP Ti with f_m=100 Hz, f_w=4 Hz, h_0=0.071 mm/rev, V_{pp}=112 V, and 0.056 mm depth-of-cut for a workpiece with 2 mm diameter. Two representative roll-over burrs are circled in yellow.

4.2 Sliding-type MAT for orthopedic applications

As discussed in Chapter 2, the addition of micro-features and micro-surface roughness to bone implants has been shown to enhance bone integration performance. The biointegration performance of implant samples processed using modulation-assisted texturing was tested using both *in vitro* and *in vivo* testing protocols. The *in vitro* testing methods involved introduction of MC3T3-E1 cells on the implant surface and provides a baseline understanding of cellular response. In comparison, the *in vivo* testing methods provide a more accurate depiction of the holistic success of the implant. The results from these experiments are described below.

To allow for comparisons between *in vitro* samples and *in vivo* samples, the samples in both of the studies were manufactured to have as similar of textures as possible. While texture geometries were not able to be identical between *in vitro* and *in vivo* samples because of amplifier power limitations, the *in vivo* samples differ from *in vitro* samples by 7% in length (~20 µm) and 2% in width (~2 µm).

4.2.1 *In vitro* results

Curved, 1 x 1 x 0.5 cm, commercially pure titanium specimens were created for *in vitro* testing. As detailed in the Materials and Methods section, four groups were tested of different morphology to evaluate the effects of surface texturing on osseointegration. Untextured (TT1) samples of 0.28 µm Ra and sandblasted (TT2) samples of 0.64 µm Ra are evaluated against modulation-assisted textures. In-phase ($\varphi = 0$, TT3) textures with parallel grooves of width 72 µm and height 15 µm; and out-of-phase ($\varphi = \pi$, TT4) textures with intersecting grooves of length 251 µm, width 108 µm, and height 25 µm are used in this study.

In vitro viability effects of sample curvatures

Figure 43 shows the effects of radius of curvature for untextured Ti samples seeded with MC3T3-E1 cells. A live / dead assay was performed to determine the viability of cells on the sample surface, with green signifying *live* cells with proper morphology and red signifying *dead* cells. From the figure, while cell growth has not reached a confluent monolayer on any of the sample surfaces, each sample has sufficient cell growth for further assays. Also evident in the figure is that the smaller radius samples may potentially have enhanced cell adhesion, however the natural variability of the *in vitro* cell tests prevents discernable differences to be established from the images themselves.

From these results, these sample dimensions were considered appropriate for further *in vitro* testing and a radius of 0.25" was used for subsequent samples.
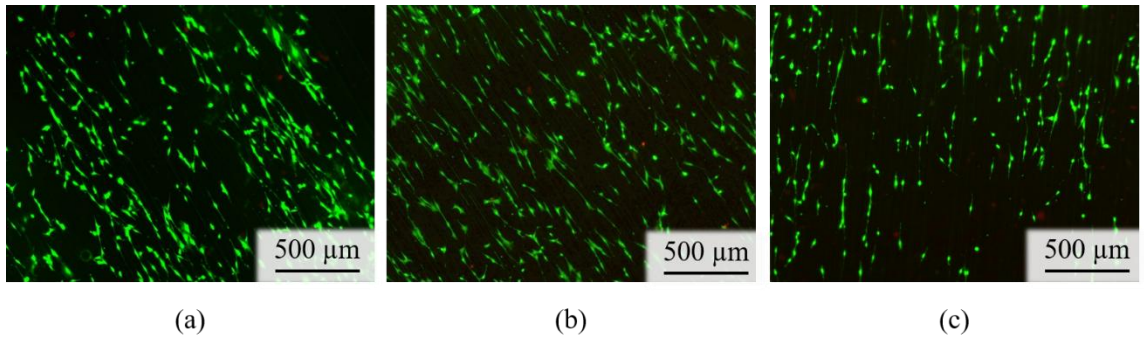
Figure 43: Adhesion study on three radii of curvature: (a) R = 0.2", (b) R = 0.2625", and (c) R = 0.325"

In vitro viability effects of surface textures

The effects of surface textures produced by modulation-assisted texturing on biointegration performance were tested *in vitro* using the above protocol with seeding of MC3T3-E1 cells. Figure 44 displays the results for cell attachment performance of the untextured sample (TT1) and the in-phase MAT sample (TT3). From the figure, the untextured sample (TT1) showed evidence of loosely attached cells sparsely populating the specimen surface. Relative to the untextured sample (TT1), the attachment for the in-phase MAT sample (TT3) was increased but did not form a fully confluent monolayer. While difficult to compare to the results of the untextured samples of different radii of curvature, this does suggest that the surface textures of the in-phase MAT sample (TT3) does encourage cell adhesion. Close examination of the in-phase textured sample (panel b) reveals that not only are there more localized colonies of MC3T3 cells that cover the

entire surface, but there are cells that have grown into the grooves of the micro-scale textures itself. Compared to the untextured sample (TT1), the surface textures encouraged cells to adhere to the workpiece. A similar phenomenon was observed in studies that evaluated cell growth characteristics in micro-grooved channels, which encouraged cell attachment and proliferation [143-145]. Extracellular matrices were found to be deposited parallel to the grooves themselves, with cells aligned in the direction of the groove. Matsuzaka et al. showed through measurements of cell activity that these micro-grooves aid in the differentiation of osteoblast-like cells [144]. The role of enhanced surface roughness on bioadhesion has been documented elsewhere [26-29] and the present results suggest that that micro-textures created by modulation-assisted texturing have similar biological influences as conventional surface texturing methods, such as sandblasting or etching.
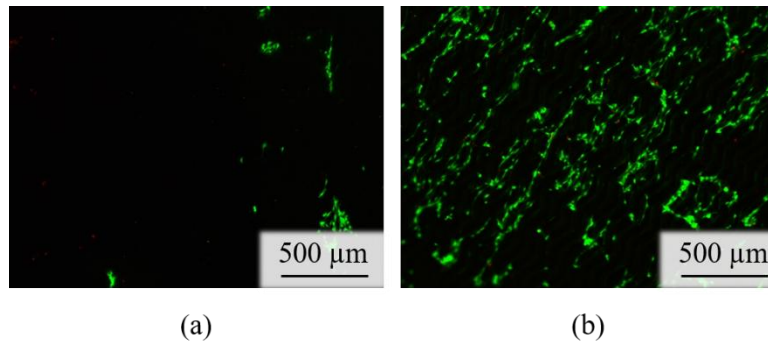
Figure 44: Attachment assay for texture (a) untextured (TT1) and (b) in-phase MAT (TT3)

It should be noted that the variability of adhesion between the untextured samples in Figure 43 and Figure 44 implies that it is solely not the sample curvature itself that is causing the variability in adhesion studies but rather it is the seeding process itself. While

panel (b) of Figure 44 shows a similar amount of cell attachment as seen on the samples from the first trial, these cells in the second trial were much more loosely attached and began detaching when handling samples for imaging.

In vitro cell responses to anodized surfaces and surface textures

To improve surficial adhesion for direct imaging, samples were anodized after surface texturing. Live / dead adhesion assays were performed on a set of anodized samples and images of the resulting surface adhesion characteristics are provided in Figure 45. From the figure, despite the large increase in cell attachment, various areas on the work surface have virtually no cell growth, especially for the untextured (TT1) and sandblasted (TT2) samples. These zones with low cell adherence were found closer to the edges of the specimens and may be associated with curvature-related effects. With anodization, adherence is greatly increased compared to the non-anodized trials, with cell growth on all surfaces. In panels (c) and (d) of the figure, distinct surface textures can be observed clearly from the cell growth. This is expected as may be unable to adhere to steep peaks found on the surfaces produced by sliding-type modulation assisted surface texturing. From the imaging results in Figure 45, more of the feature peaks of the in-phase MAT sample (TT3) remain uncovered with cells, as cells migrated into the channel surrounding each peak. In the in-phase MAT sample (TT3), feature peaks are roughly 60% the height of those in the out-of-phase MAT sample (TT4), which allows for enhanced cell adhesion.
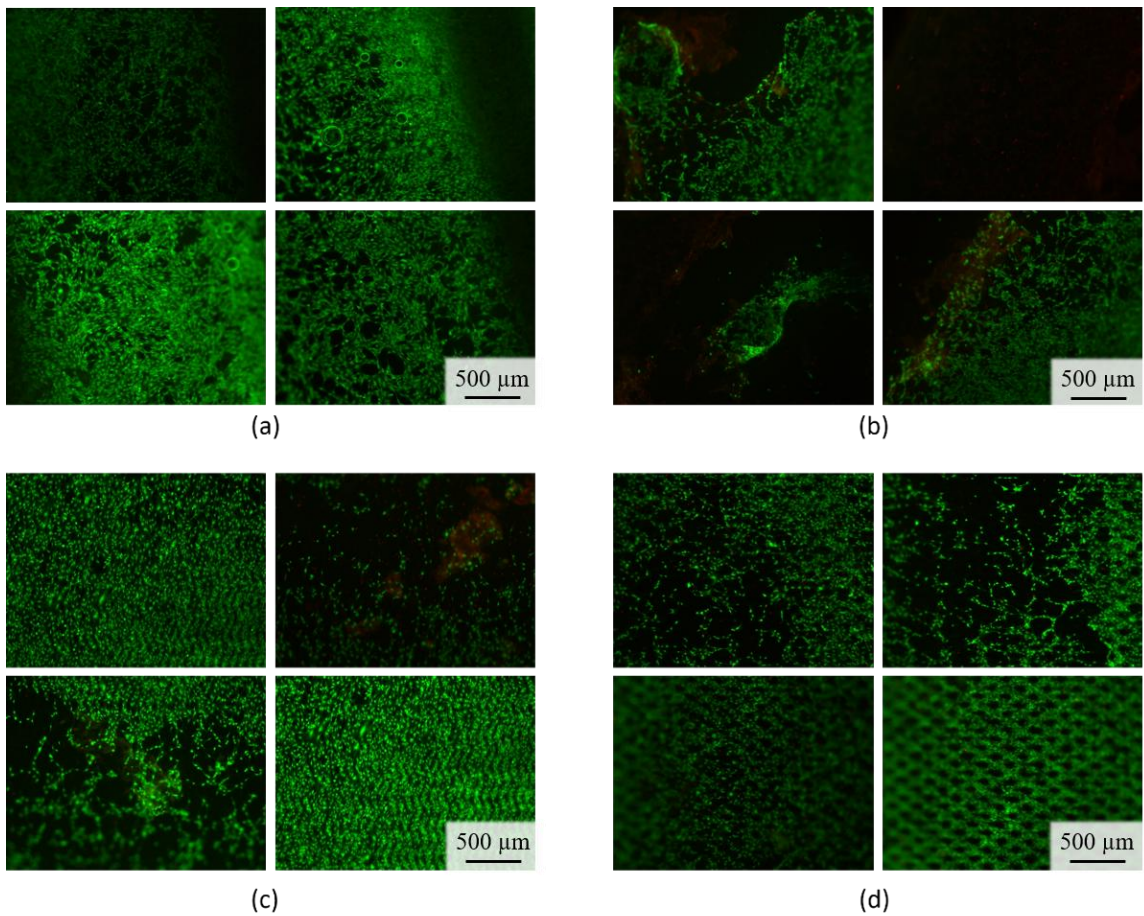
Figure 45: Live/dead assay for in vitro samples after anodization. All images use a 4x magnification objective. (a) untextured (TT1) (b) sandblasted (TT2) (c) in-phase MAT (TT3) (d) out-of-phase MAT (TT4)

For the purpose of quantifying cell adhesion, the same set of surface textures were produced without anodization treatment. Cells were trypsinized (removed using trypsin) from the sample surfaces and counted in solution to assess the viability of each of the surface texture conditions, and these measurements are summarized in Figure 46. In order of most viable to least: the in-phase MAT sample (TT3) was seen to have a mean cell count of 116,175 (σ = 81,340), the untextured sample (TT1) with mean of 67,875 (σ =

57,665), the out-of-phase textured sample (TT4) with mean of 27,000 (σ = 48,526), and the sandblasted sample (TT2) with mean of 15,375 (σ = 6,197). One-way ANOVA showed a significant (p<0.001) difference in population means, with a post-hoc Bonferroni test showing at the 95% confidence level significant difference in means between the various treatments of TT2 and TT3, and TT3 and TT4.
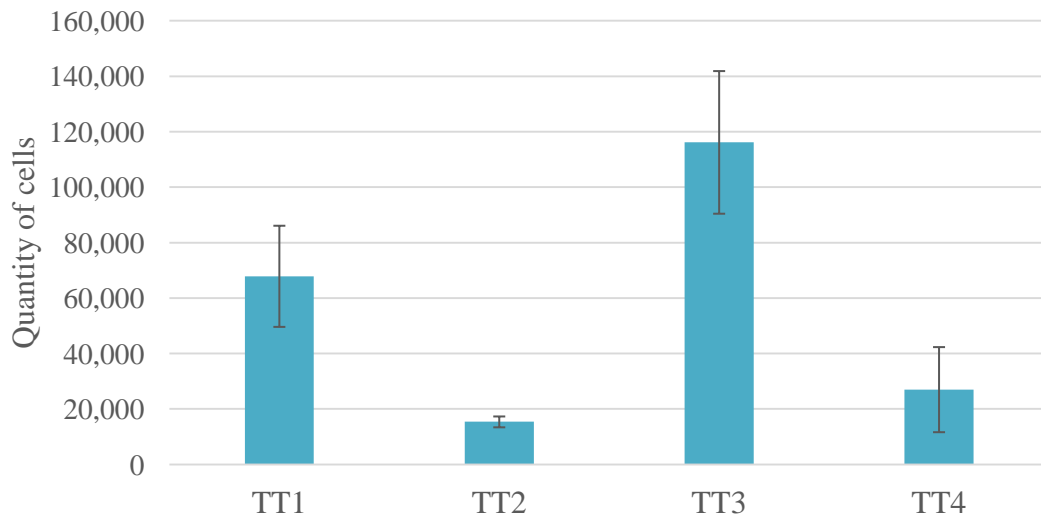
Figure 46: Adhesion study of all *in vitro* samples after one week culture; n=10 samples / group.

The in-phase MAT sample (TT3) exhibited increased cell-adhesion compared to all other samples, including the control untextured and sandblasted samples. This is likely due to its increased surface roughness and the effects of the micro-scale grooves which have been shown in the literature and the qualitative tests of Figure 45 to encourage cell growth. Surprisingly, its mean number of adhered cells is more than four times that of the out-of-phase MAT sample (TT4). The relatively lower performance of the out-of-phase

textured sample (TT4) may be explained by the relative difference in feature height of the TT4 sample compared to that of the TT3 sample.

It is also apparent from the present results that the untextured sample (TT1) exhibited increased cellular adhesion compared to the sandblasted sample (TT2). This is also clear for the anodized samples in Figure 45, wherein the TT1 sample showed presence of a near confluent monolayer while the TT2 sample exhibited large areas with low cell adherence. With a mean cell count value of 15,375 cells, which is roughly 20% of the smooth control (67,875 cells), the sandblasted sample (TT2) signifies that surface roughness was not dominant in determining cell adhesion performance. While it is difficult to conclusively determine the root cause of the increased surface adhesion, possible theories may be extrapolated from previous *in vitro* studies. Many studies show that increasing surface roughness enhances *in vitro* cellular adhesion, however studies typically refer to micron-level surface roughnesses [3, 26-31] (see Background). In this regard, the untextured sample (TT1) sample was turned to a mirror-finish (~ 0.25 μm Ra), a regime wherein the effects of nano roughness becomes a significant modulator of osteoblast adhesion [146] and may explain the increased cell adhesion seen for the untextured sample (TT1). Regardless, the interpretation of the present results should also acknowledge the uncertainty regarding use of *in vitro* tests for signaling cellular adhesion. In this regard, cells may not actually be adhered to surfaces, but are merely proliferated, leading to uncertainty in the signaling of actual cellular adhesion levels [147-150].

In vitro effects of surface texturing on DNA and ALP content

Cell count measurements were verified by testing the DNA content of well plates for each sample and are summarized in Figure 47. From the figure, the proportions of DNA

content from each sample condition are similar to the trends seen in the cell count measurements. These measurements show that the untextured sample (TT1) and the in-phase textured sample (TT3) facilitated greater cell attachment and proliferation after the week of culture. A one-way ANOVA shows that modulation-assisted texturing significantly ($p < 0.0001$) changes the mean DNA content when compared to the control groups. A post-hoc Bonferroni's multiple comparisons test showed that TT1 and TT3 had significantly more ($p < 0.05$) DNA content than the other samples (but not compared to each other).
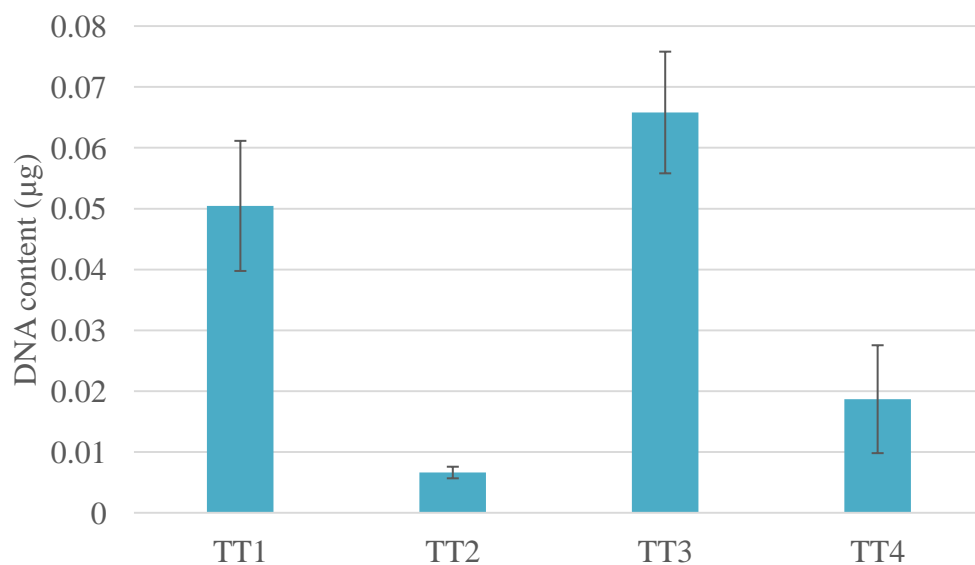
Figure 47: DNA activity of all *in vitro* samples after one week of culture; n=10 samples / group

Figure 48 shows the ALP content normalized to the DNA concentration to eliminate the confounding effects of variable cell seeding. After normalization,

sandblasted TT2 and out-of-phase TT4 samples showed mean ALP activity of 1714 and 1164 nmol/hr/µg DNA, respectively, showing a facilitation of early osteogenic response compared to untextured (TT1, 297) and in-phase (TT3, 639). A one way ANOVA showed that the surface textured samples (TT2 – TT4) caused significant shifts in mean ALP activity ($p < 0.0001$). More specifically, Bonferroni's multiple comparisons post-test showed the sandblasted TT2 and out-of-phase TT4 textures being significantly different ($p < 0.05$) from the other samples, but not from each other. Since samples are in growth medium (as opposed to osteogenic medium), this experiment shows the ability of sandblasting and modulation-assisted textures to facilitate osteogenic differentiation.
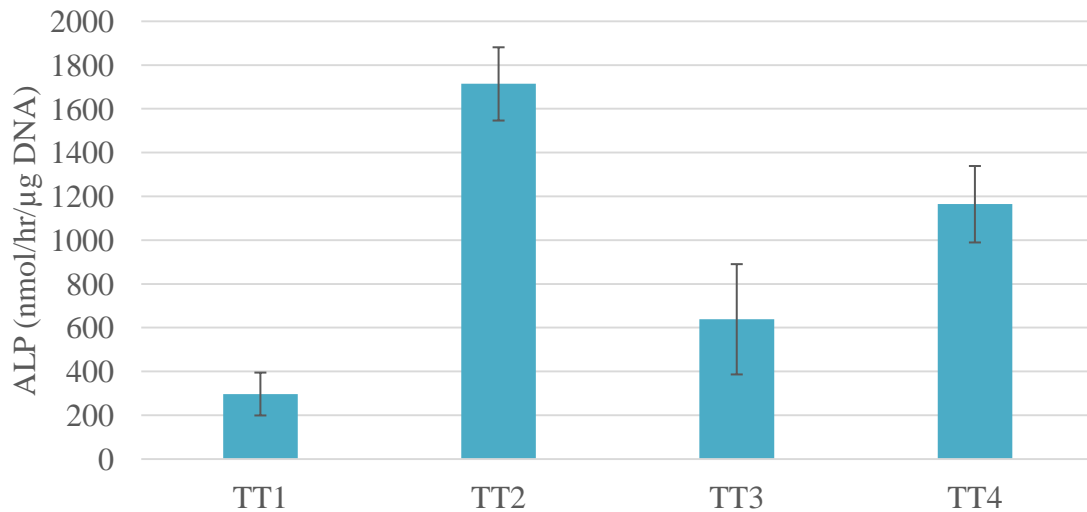
Figure 48: ALP activity of all *in vitro* samples normalized to DNA content after one week of culture; n=10 samples / group

4.2.2 *In vivo* results

The results from *in vitro* studies, while integral for understanding mechanisms that drive osseointegration, only elucidate biological responses on a cellular level. *In vivo* biointegration testing involving bone volume and pull-out were performed to aid in the understanding of osseointegration effects on a macroscopic implant fixation level. Because of the multiple and complex interactions that occur during bone reconstruction, results from *in vivo* tests are well known to be a better indicator of implant effectiveness [151]. 2 mm, commercially pure titanium specimens were created for *in vivo* testing. As in *in vitro* testing and detailed in the Materials and Methods section, four groups were once again tested of different morphology to evaluate the effects of surface texturing on osseointegration. Untextured (TT1) samples of 0.28 μm Ra and sandblasted (TT2) samples of 0.49 μm Ra are evaluated against modulation-assisted textures. In-phase (φ = 0, TT3) MAT samples with parallel grooves of width 71 μm and height 13 μm; and out-of-phase ($\varphi = \pi$, TT4) MAT samples with intersecting grooves of length 233 μm, width 106 μm, and height 24 μm are used for *in vivo* testing.

Aside from one rat that was lost under anesthesia during surgery, all rats healed without complications until the end of the study. Figure 49 shows average bone volume over total volume (volume of interest: VOI) and accompanying standard deviations for the *in vivo* samples. This morphometric measurement is also referred to as bone volume density and quantifies the percentage of bone that surrounds the implant. The in-phase MAT sample (T3) had the highest bone volume density, with 48.6% of the total volume filled with mineralized bone (σ = 20.4%). The sandblasted sample (T2) had a bone volume density of 37.5% (σ = 18.9%). The out-of-phase MAT sample (T4) had a mean bone volume density of 32.9% (σ = 13.3%). Finally, the untextured sample (T1) had the

lowest bone volume density of 30.9% ($\sigma = 25.3\%$). A one-way ANOVA analysis showed that at a 95% confidence level, the population means are not significantly different ($p = 0.39$). Nevertheless, the in-phase MAT sample (T3) showed more mineralized bone in the VOI compared to the out-of-phase MAT sample (T4), similar to the observations made in the *in vitro* cell culture tests. However, unlike the prior results, the untextured sample (T1) showed less bone mineralization compared to all other sample conditions. This is consistent with other reports of low bone volume densities for smooth verses roughened surfaces [152-154].
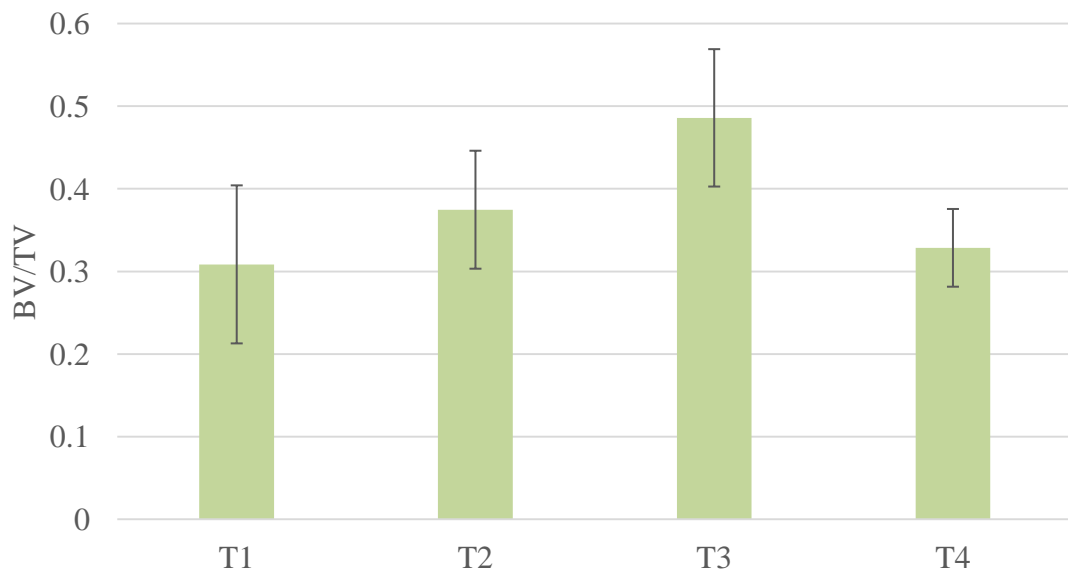
Figure 49: Bone volume over total volume (bone volume density) for *in vivo* samples; n=8 samples / group

While average bone volume to total volume values give insight on how specific textures influence peri-implant bone growth, it does not directly reveal the amount of

load that an implant can undertake, which is directly related to an implant's structural integrity and mechanical failure limit. Figure 50 shows representative load curves for each of the textured samples tested, and Figure 51 summarizes the results of the implant pull-out tests and directly shows the mean maximum load at fracture. The out-of-phase MAT samples (T4) had the largest strength with a mean pull-out force of 24.7 N (σ = 14.1 N), compared to the in-phase MAT samples (T3) with a pull-out force of 22.3 N (σ = 11.6 N). The conventional sandblasted sample (T2) and untextured sample (T1) required pull-out forces of 9.0 N (σ = 7.5 N), and 4.3 N (σ = 1.2 N), respectively. A one-way ANOVA test showed that means are significantly different ($p<0.01$) with Bonferroni's multiple comparisons post-hoc test showing at the 95% confidence level that T1 vs. T3 and T1 vs. T4 were significantly different.
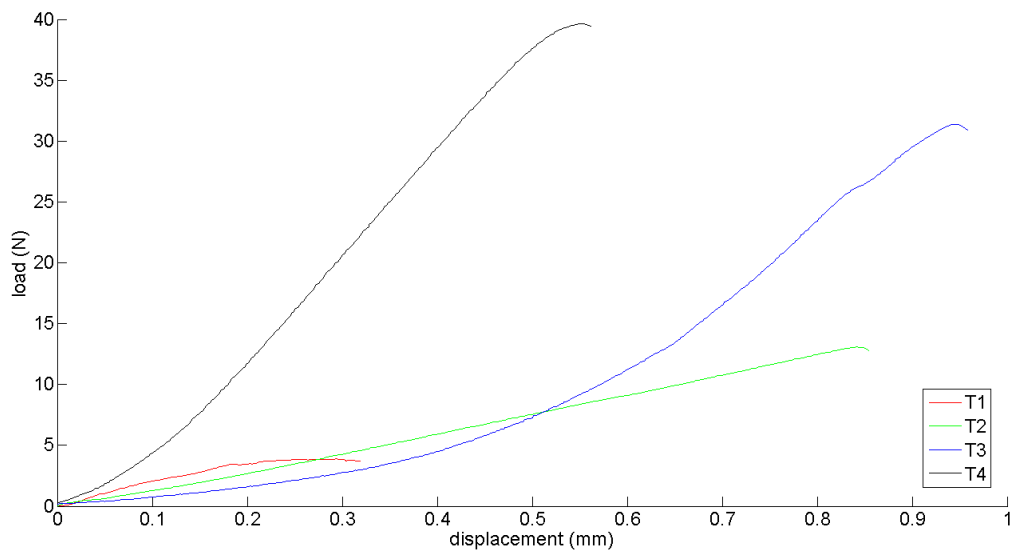
Figure 50: Representative pull-out testing load curves
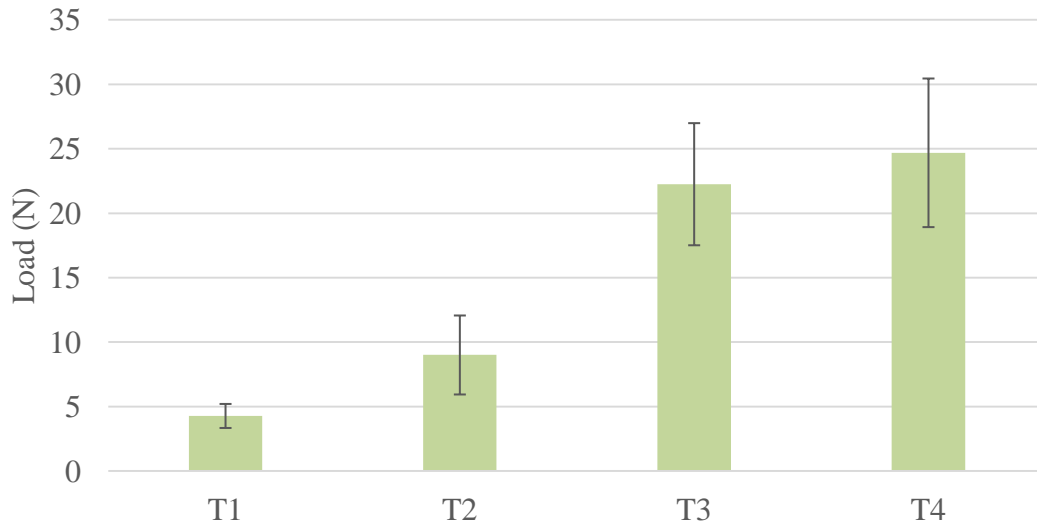
Figure 51: Pull-out strength per test condition for *in vivo* implants

While the high pull-out strength of the in-phase MAT sample (T3) and lower pull-out strengths of the untextured (T1) and sandblasted (T2) samples are expected from the previous BV/TV and cell adhesion studies, the high value for strength of the out-of-phase MAT sample (T4) stands apart from the trend. This can be explained by the effects of the effects of mechanical interlocking on interfacial strength [67]. As the out-of-phase textured sample (T4) had the tallest micro-textures among the tested conditions, it is plausible that these textures increased the strength of the bone-implant interface through additional bone ingrowth and mechanical interlocking. This stabilization could increase the load-bearing area, ultimately leading to a larger pull-out force [3, 10-12]. Future studies may be conducted to establish confirmation of this theory using FEA. Bone density also may provide further evidence to understand why the out-of-phase MAT sample (T4) strength was enhanced, however excessive beam hardening in the μCT images prevented extraction of density data.

4.2.3 Summary and additional discussions

These measurements showed the effects that surface textures have on *in vitro* and *in vivo* osseointegration measures. The ability for cells to adhere to curved surfaces was first established, however data was ultimately normalized because of the lack of confluence on sample surfaces. While untextured (TT1) and in-phase ($\varphi=0$, TT3) MAT samples showed increased levels of adhesion and proliferation, Sandblasted (TT2) and complete out-of-phase ($\varphi=\pi$, TT4) MAT samples showed increased levels of ALP activity, which is a direct sign of pre-osteoblastic differentiation. Understanding a surface texture's ability to encourage differentiation serves as a precursor to higher fidelity *in vivo* studies, as the successful differentiation of osteoblasts is directly related to bone growth on the surface of textures [155]. μCT scans and pull-out tests were used to quantifiably measure the relative effects texture has on bone integration. Bone volume densities were measured, and while more textured samples are necessary to achieve greater statistical significance, there appeared to be a positive effect of surface modification on bone mineralization. More specifically, in-phase ($\varphi=0$) modulation textures have been shown to increase bone mineralization by about 60% and 30% compared to untextured and sandblasted samples, respectively. A more convincing measurement of osseointegration was made through pull-out tests, which showed a statistically significant difference in means between the samples processed using modulation-assisted texturing and the conventional turned and sandblasted samples.

These findings clearly show the holistic benefits of modulation-assisted texturing in improving relative osseointegration levels compared to controls. Additionally, these findings open continuing research questions to precisely understand the interactions of multiple parameters and their effects on bone integration. To clarify, the modulation

texturing processes used in the present study simultaneously affect surface geometries, roughness values, and grain orientations, among other characteristics. The coupling of these output variables provides an understanding of how modulation-assisted textures behave in clinical applications, however hinders the ability to specifically attribute increased osseointegration to single characteristics (i.e. increased roughness). Carefully designed studies aimed towards understanding the underlying reasons for improved performance can allow for increased optimization of surface textures in future studies to further improve the osseointegration capability of modulation-assisted textures.

4.3 Plunging-type MAT for tribological applications

The tribological performance of surfaces processed using plunging-type modulation-assisted texturing was tested to understand the effects of textured textures on interfacial wear. For this purpose, aluminum 6061T6 textured disks were tested using a pin-on-disk wear configuration to explore effects of texture geometry on coefficient of friction and surface wear. The below data summarizes the experimental measurements.

4.3.1 Face texturing effects on interface friction

The coefficient of friction μ_f for the textured and untextured samples was measured during the pin-on-disk testing experiment for a range of sliding speeds by adjusting the rotational speed from 100 to 400 RPM. These measurements are summarized in Table 19 and are plotted as a function of the dimensionless Hersey number nv/p in the Stribeck curve shown in Figure 52. The Hersey number (also referred to as the bearing or Stribeck number) is defined as the absolute viscosity (n) multiplied by the rotational speed (v) divided by the pressure. From the results, the coefficient of friction falls from $\mu_f = 0.23$ to $\mu_f = 0.08$ for the untextured samples as the Hersey number increases from $nv/\rho = 12.8$ to $nv/\rho = 51.2$. The rapid decrease in the coefficient of friction from $nv/\rho = 12.8$ to $nv/\rho =$

25.6 is indicative of transition from boundary lubrication to mixed lubrication. At larger values of $nv/\rho = 25.6$ to $nv/\rho = 51.2$, the coefficient of friction stabilizes to $\mu_f = 0.08$, this indicative of hydrodynamic lubrication.
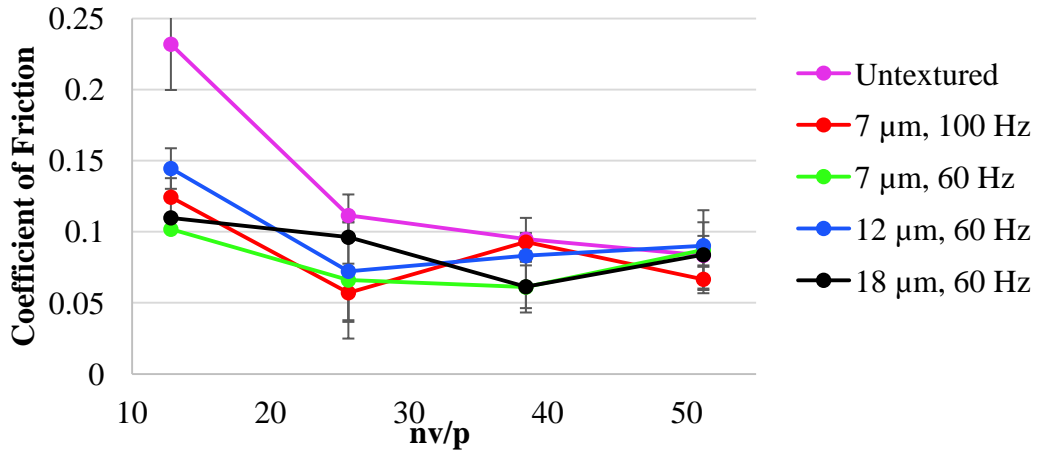
Figure 52: Stribeck curve at $nv/\rho = 12.8$, 25.6, 38.4, and 51.2.

Table 19: Coefficient of friction (μ_f) measurements and accompanying standard deviations for pin-on-disk testing experiments

Sample Type	RPM	Normal Load (N)	Contact Pressure (MPa)	Viscosity (cm^2/s)	nv/p	μ_f	std of μ_f
	100	9.81	3.123	0.4	12.81	0.23	0.03
	200	9.81	3.123	0.4	25.62	0.11	0.01
	300	9.81	3.123	0.4	38.42	0.09	0.02
Untextured	400	9.81	3.123	0.4	51.23	0.08	0.02
	100	9.81	3.123	0.4	12.81	0.12	0.01
	200	9.81	3.123	0.4	25.62	0.06	0.02
7 µm, 100	300	9.81	3.123	0.4	38.42	0.09	0.01
Hz	400	9.81	3.123	0.4	51.23	0.07	0.01
7 µm, 60	100	9.81	3.123	0.4	12.81	0.10	0.00

Hz	200	9.81	3.123		0.4	25.62	0.07	0.04
	300	9.81	3.123		0.4	38.42	0.06	0.02
	400	9.81	3.123		0.4	51.23	0.09	0.03
	100	9.81	3.123		0.4	12.81	0.14	0.01
	200	9.81	3.123		0.4	25.62	0.07	0.03
12 µm, 60	300	9.81	3.123		0.4	38.42	0.08	0.00
Hz	400	9.81	3.123		0.4	51.23	0.09	0.01
	100	9.81	3.123		0.4	12.81	0.11	0.00
	200	9.81	3.123		0.4	25.62	0.10	0.00
18 µm, 60	300	9.81	3.123		0.4	38.42	0.06	0.02
Hz	400	9.81	3.123		0.4	51.23	0.08	0.01

The tribological performance of the MAT dimpled samples show markedly lower friction especially at lower Hersey number from $nv/\rho = 12.8$ to $nv/\rho = 25.6$. At $nv/\rho = 12.8$, the average coefficient of friction of the four textured samples is $\mu_f = 0.12$, compared to $\mu_f = 0.23$ for the untextured samples. At higher nv/ρ, the coefficient of friction drops slightly into the range of $\mu_f = 0.07$ to $\mu_f = 0.09$. The smaller decrease in coefficient of friction compared to the untextured samples implies that the untextured samples may initially start either in a boundary or mixed lubrication regime compared to the textured samples which may already be within the elasto-hydrodynamic regime. It should be noted that the Stribeck curves reported in Figure 52 for the various textured conditions tested, including increasing texture depth and increasing texture density, do not clarify any significant effects of texture morphology on wear performance for these wear conditions. A likely source of this lack of sensitivity is that even at these low speeds, the sample could potentially be well into the elasto-hydrodynamic regime, leaving challenges in differentiating frictional performance of these multiple texture configurations.

The minimum coefficient of friction for the system appears to be in the range of $\mu_f = 0.05$ to $\mu_f = 0.1$ for nv/ρ between 25 and 40. Where the minima occurs indicates the ideal combination of normal force, lubrication level (and type), and surface speed for each sample. While boundary layer lubrication was not observed in the textured samples, a small region of mixed lubrication was observed for textured samples at lower sliding speeds. Under these conditions, surface asperities for each interface are in direct contact and hydrodynamic forces are insufficient to maintain a consistent lubrication layer, which leads to the high frictional coefficient seen during metal on metal contact. Limitations of the current testing equipment prevented lower rotational speeds to be tested, however it is presumed that the μ_f for the textured samples would increase to that observed by the untextured samples at sufficiently low speed because of the similar asperity contact conditions under insufficient lubrication.

4.3.2 Face texturing effects on interface wear

The effects of the surface texturing process on cross-sectional wear area were also evaluated from the pin-on-disk testing. Figure 53 shows representative microscopy images of the five test conditions and their representative wear tracks. Images show textures centered in wear tracks and do not show gross texture deformities post-testing. Wear debris is not observed within textures themselves, as reported in a number of studies [1, 13-18], however the lack of particles may be a result of reduced interfacial wear compared to previous studies.
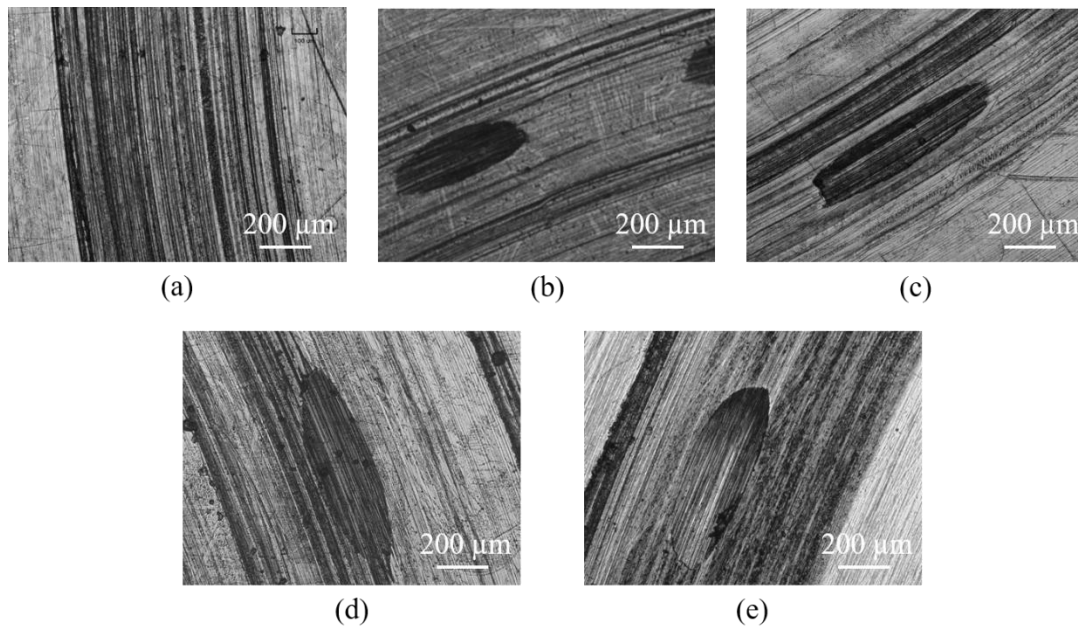
Figure 53: Representative microscopy images of wear tracks for (a) untextured, (b) 7 µm, 100 Hz, (c) 7 µm, 60 Hz, (d) 12 µm, 60 Hz, and (e) 18 µm, 60 Hz samples

Representative profilometer traces that were used to calculate cross-sectional wear area are shown in Figure 54. In general, wear profiles showed discrete wear regions, with the remainder of the sample unaffected by testing. Side-flow that resulted in ~ 2 µm increases in surface height is seen in panel (b) for the 18 µm sample. More significant height increases (5-7 µm) occur in the 7 µm (100 Hz) and 12 µm (60 Hz) samples of panel (c). This change to the sample surface does not affect friction or wear area measurements, but are noted to show variations that occurred during testing. In panels (a) – (d) it can be seen that wear varies in width from about 1 mm for untextured samples at $nv/\rho = 26$ to about 0.2 mm for the 7 µm (100 Hz) sample at the same RPM. Wear profiles are also of varying morphology, with most profiles showing symmetric wear on both sides of the maximum wear depth. This is expected by nature of the testing procedure.

107

From the wear profiles, it appears that increases in texture depth reduce the width of wear, however lead to larger maximum depths. In panel (a), for instance, the wear width of the untextured sample is about 0.6 mm, however the 18 µm surface texture exhibits a wear width of about 0.3 mm. The maximum depth of these wear profiles for the untextured verses 18 µm samples is about 7 µm and 15 µm, respectively. Though multiple reasons may explain this phenomenon, this increased depth is likely due to two reasons. First, in the process of texturing samples, side-flow causes the surface of the material to bulge from the cutting surface (similar to the outcome of the 7 and 12 µm surfaces in panel c). As this bulging material protrudes from the surface of the sample, it exhibits increased wear and as a result, increased wear debris that can accelerate the rate of wear in that radial region. Second, and likely far more significant, is that the plunging-type MAT process leaves small burrs on the workpiece surface itself (usually on the sides and at the ends of textures). While samples were blown with compressed air and rinsed with acetone, small burrs were likely still attached to the sample itself, causing regions of increased depth. To alleviate this issue in future testing, a final finishing pass with the PCD tool may be used in a phantom pass to remove burrs and bulging material.
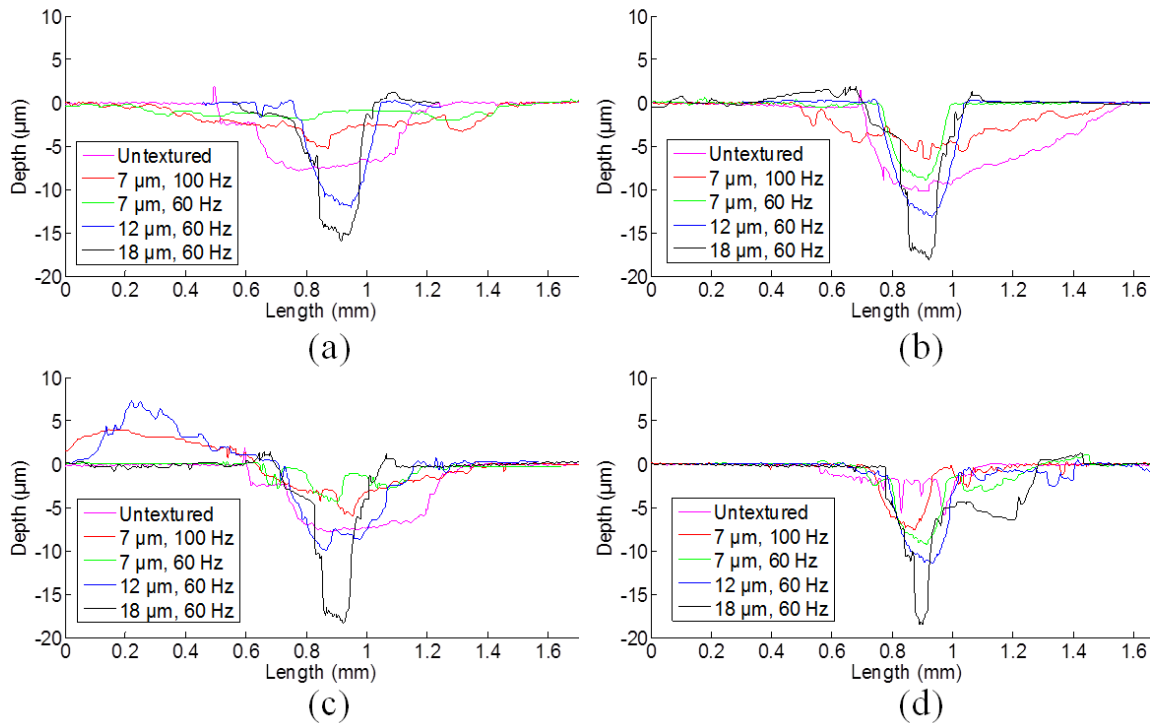
Figure 54: Representative profilometer measurements of wear tracks of textured samples at nv/ρ = 12.8, 25.6, 38.4, and 51.2.

Figure 55 shows the average cross-sectional wear area of the tested samples over the range of conditions tested. From these findings, it is seen that any amount of surface texturing improves the wear resistance for all cases except for the 18 μm sample at nv/ρ = 51 RPM. Further, a few additional observations can be made. First, though coefficient of friction for the two 7 μm samples were similar to each other (7 μm, 100 Hz: ~0.1; 7 μm, 60 Hz: ~0.13; verse untextured: ~0.24 at nv/ρ = 13), the increase in texture density greatly varied the wear area for all testing below nv/ρ = 51. At nv/ρ = 13, the 100 Hz sample had worn four times more than the 60 Hz sample (2716 μm^2 verse 505 μm^2). At nv/ρ = 26, this difference is more apparent, with the increase in texture density leading to

almost five times as much wear. Across all RPMs, the 7 µm and 12 µm (60 Hz) samples consistently reduced the amount of cross-sectional wear area. Second, considering each panel, it is seen that as the Hersey number increases from (a) to (d), the average wear decreases for all samples. This is expected when in the elasto-hydrodynamic regime, as faster surface speed translates to additional separation force and reduces contact between surfaces. As surface velocity increases from panels (a) to (d), the decrease in surface asperity interaction results in decreased wear (also confirmed by the decreasing coefficient of friction on the Stribeck curve). Finally, it is interesting to observe the wear behavior of the 18 µm textured sample, which removes approximately 2400-3400 µm^2 of material and does not decrease in wear as sharply as the other sample types. This signifies that the interfacial hydraulic force is insufficient in decreasing the surface asperity interactions at these speeds and larger Hersey numbers are necessary prior to observing decreases in wear and friction for these textured samples.
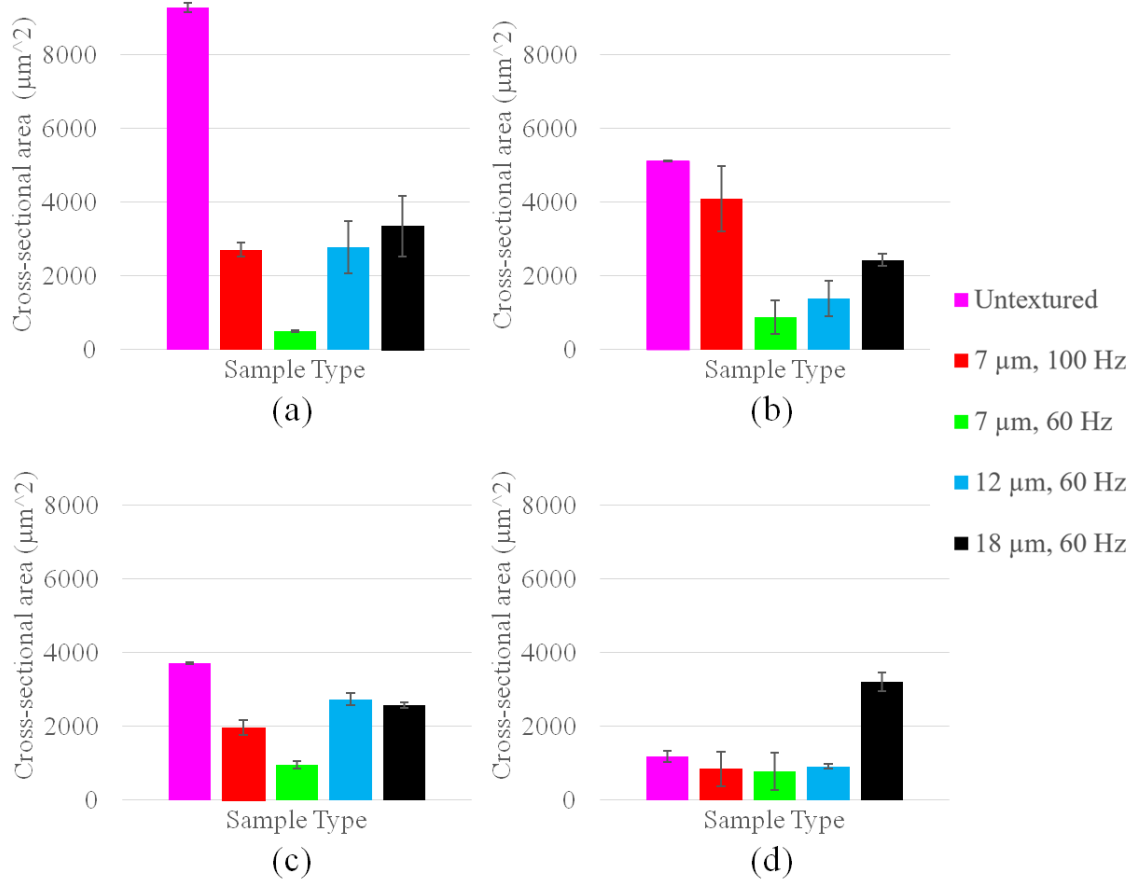
Figure 55: Average cross-sectional wear area of samples for four RPM conditions: nv/ρ = (a) 12.8, (b) 25.6, (c) 38.4, and (d) 51.2.

CHAPTER 5

CONCLUSION

This research study has focused on understanding a novel manufacturing technique and investigating its potential applications. The sliding-type modulation-assisted texturing process has been shown to be controllable and flexible in creating surface textures of varying morphology. The modeled effects of input parameters on resulting surfaces were compared to machined samples, and showed not only the versatility of the process, but also the closeness of fit between modeled and physical experiments. The study first developed a sliding-type MAT model, which had not been previously accomplished. This model allows for the prediction of machined surface geometries and indicates parameter effects prior to machining. When compared to fabricated specimens of phase shift $\varphi = [0,$ $\pi/2, \pi, 3\pi/2]$, the sliding-type MAT model has been shown to predict length measurements with errors of less than 2% and width errors that do not exceed 6%. Height values, however, differed from expected values by up to 60%, and expose a deviation of the sliding-type MAT process from a purely geometric model. As a geometric model, this computer simulation serves as a building block for more advanced models that can more closely predict sliding-type surface geometries and better understand phenomena such as the height deviations currently seen. Model development naturally leads to understanding the deformation characteristics and resulting surface material properties.

After establishing sliding-type MAT as a controllable and predictable surface texturing technique, this research study shows applications of modulation-created textured samples for orthopedic and tribological applications. In terms of orthopedic

112

testing, sliding-type MAT was used for *in vitro* and *in vivo* tests, showing the improved osseointegration capacity of textured bone implants when compared to controls. For *in vitro* studies, textured and complete in-phase samples showed increased levels of cell adhesion and proliferation, while sandblasted and complete out-of-phase samples showed increased levels of ALP activity, which is a direct sign of pre-osteoblastic differentiation. Most significant, however, are the marked benefits of sliding-type MAT textures *in vivo*. Here, in-phase modulation textures have shown to increase bone mineralization by 60% and 30% compared to untextured and sandblasted samples, while both in-phase and out-of-phase textures were shown to increase mean pull-out force by about 2.5 times compared to sandblasted samples and 7 times compared to smooth samples. This research has shown the increased osseointegration capability of textured samples and serves as the precursor to more comprehensive studies that investigate the underlying mechanisms of bone integration. This study has also opened modulation-assisted texturing to the field of bone implant development and allows for additional avenues of interdisciplinary research.

The previously established plunging-type MAT technique was utilized to create samples for tribological testing to show that micron-scale surface textures can improve frictional properties by delaying the onset of the boundary lubrication regime. These pin-on-disk tribological tests suggest that in the parameter range tested, the addition of textures decrease friction coefficients when compared to untextured controls. While at larger surface speeds, differences in friction coefficients are relatively small, the friction coefficient is decreased by about 50% at lower surface speeds. The amount of material wear was quantified by measuring the cross-sectional area removed during testing, and showed decreases in material wear across all textured samples when compared to smooth

controls. The largest amount of wear reduction was seen at $nv/\rho = 13$ when comparing the untextured sample and the 7 µm sample machined at a modulation frequency of 100 Hz. In this case, the addition of surface texturing is shown to have decreased cross-sectional area wear by about 18 times. While the wear reductions were not typically this substantial, the decrease in wear rate signifies the improvements in wear resistance for MAT textured samples when compared to untextured controls.

In the present study, the controllability of surface morphology was established. The benefits of surface modification were seen in both orthopedic and tribological applications, but the study focused primarily on the benefits of surface geometry. Since modulation-assisted texturing modifies multiple parameters simultaneously (i.e. surface geometry, microstructure, surface roughness, etc.), further research is necessary to comprehensively understand the precise parameters that are responsible for the encouraging results. By decoupling and understanding the relative effects of input parameters, optimization of the modulation-assisted texturing process will be possible for future studies.

APPENDIX A

```
%% length_width_calc.m
%In length_width_calc.m fm, fw, δ, A, and h0 %values are inputted and
the mean and standard deviation is outputed for %length, width, and
height. fm and A values in this simulation may either %be constant
values, which simulates textures under ideal conditions (i.e. %no
variation in modulation parameters), or the values may be an array of
%values that simulate the variations seen in real-life experiments.
This %simulation was created to understand the effects of input
parameters on %surface textures. When the script is used with
conjunction          with          %MAMlathe_freqdist_finder.m          and
MAMlathe_Asave_finder.m, measured frequency and amplitude values may be
%inputted into the script, giving modeled measurements of the actual
%cutting experiment. Frequency and amplitude values may also be
simulated by using number distribution generators.

% Ryan Liu
% 3/11/16


clearvars -except freq_dist A_save, close all, clc

mean_fm = 100.5; %hz
mean_fw = 1; %hz




sample_fm = [freq_dist]; %      normrnd(100.25, 0.19, 1, 50000); %;

R = 3810; %um
f =63.5; %um
   lambda = 2*pi*R * (mean_fw / mean_fm);

for count = 1:max(size(sample_fm))

% if sample_fm(count)/mean_fw < mean_fm/mean_fw
length(count)      =      2*pi*R      *      1/      (mean_fm/mean_fw)      +
abs(abs(sample_fm(count)/mean_fw  -  floor(sample_fm(count)/mean_fw))-
.5)*lambda; %if it's 100.6, then we will have to add a (.6-.5 = )
                                                                %.1
wavelength in. so lenght =  2piR / (100.5) + amount offset
                                                                %
amount offset = (.6-.5 = .1), so we add .1 lambda length to the total
length.
```

```matlab
end
 close all

%hist(length,10000)

%% width

A =  normrnd(30.63, 0.06, 1, 50000); % A_save; %
count_width = max(size(A));

for position = 1:count_width
w(position) = 2 * A(position) + f;

end

close all
%hist(w,1000)

%given w, what is the height?
%% height

%w = f * ones(1,500); %for complete in phase, width is equal to the
feed

x = w/2 * 10^-6; %[m]
ap = 63.5 * 10^-6; %depth of cut [m]

height = @(x)  (-sqrt(3)*x - .1*(10^-3))  .*(x<= -.025.*(10^-3)*sqrt(3))
...
             +  (-sqrt((.05*(10^-3))^2  -  x.^2))    .*(x  >-.025*(10^-
3)*sqrt(3)).*(x < .025*(10^-3)*sqrt(3)) ...
             + (sqrt(3)*x -.1*(10^-3))*  (x >=  .025*(10^-3)*sqrt(3));
%equation of tip geometry (make it have a minimum). put in meters, get
out meters

height(0) %min height

for count_height = 1:max(size(x))
 height_calc(count_height) =  height(x(count_height)); % [m]
end

height_calc = height_calc - height(0); %so the minimum is at zero
height_calc(height_calc>ap) = ap; %anything taller than the depth of
cut is equal to the max depth of cut

hist(height_calc, 1000)
```

116

```
mean_freqdist = mean(freq_dist)
std_freqdist = std(freq_dist)
mean_length = mean(length)
std_length = std(length)
mean_width = mean(w)
std_width = std(w)
mean_height = mean(height_calc)*10^6
std_heat = std(height_calc)*10^6


%{
Explicit solution


fm = 100.5; %hz
fw = 1; %hz



R = 3810; %um
f =-63.5; %inches


lambda = 2*pi*R * (fw / fm);

A = 1 - cos(4*(pi^2)*R / lambda);
B = sin(4*(pi^2)*R / lambda);
C = 2*f*pi*R;

length  =  2*((lambda  /  (2*pi))  *atan(2*A*B  +  sqrt(4*(A^2)*(B^2)  -
4*(A^2-C^2) ...
    * (B^2 - C^2) / (2*(A^2 - C^2)))) - (lambda / (2*pi)) *atan(2*A*B -
sqrt(4*(A^2)*(B^2) - 4*(A^2-C^2) ...
    * (B^2 - C^2) / (2*(A^2 - C^2)))))

%}

%assume f = 2A

%{
this is if the fm/fw is contant throughout hte entire sweep. i.e. if
fm/fw
= 100.6 for 1 sine wave, this sim says that's what it is for hte entire
rev


fm = 100.5; %hz
fw = 1; %hz
```

```matlab
R = 3810; %um
f =-63.5; %inches


lambda = 2*pi*R * (fw / fm);


length  =  2*pi*R  *  1/  (fm/fw)  +  abs(abs(fm/fw  -  floor(fm/fw))  -
.5)*lambda %if it's 100.6, then we will have to add a (.6-.5 = )
                                                            %.1
wavelength in. so lenght =  2piR / (100.5) + amount offset
                                                            %
amount offset = (.6-.5 = .1), so we add .1 lambda length to the total
length.
%}
%this is for if the freq is equal to the mean all hte way around, and
hten
%the  particular  textur  eof  question  has  variability.  i.e  if  mean  =
100.5,
%and the fm/fw that we pulled is 100.6, we assume that it is 100.5 all
the
%way around, until the texture in question.
%%%%note. the -.5 is for comlete out of phase. use -.75 or -.



------




%% sliding_circumference_MAM_surface_model_V1_1_1.m

%The  kinematic  equations  of  motion  detailed  in  the  previous  section
also %informed  the  creation  of  a  3D  MATLAB  simulation.  This  simulation
is %intended to provide a holistic understanding of input parameters on
%overall  texture  morphology.  While  analysis  on  texture  sizes  is  not
%provided,  the  model  provides  a  representation  of  how  intersecting
%toolpaths  appear  in  3D  space.  The  script  for  this  code  is  provided  as
%sliding_circumference_MAM_surface_model_V1_1_1.m in the Appendix.

%Ryan Liu
%3/11/16
%
%coordinate definition: per lathe conventions: +x is up, +z is right,
+y is out of page
%first  machined  point  is  at  z  =  -1  and  x  =  1,  as  the  bit  machines
towards
%-z


clear all; clc; close all
```

118

```matlab
A = .075*10^-3; %amplitude [m]
d = 1.5 * 10^-3; %diameter of part [m]
offset = -.0381*10^-3;  % mam device offset (depth of cut) [m]
z_length = .85*10^-3; %z-length of part to be turned [m]
f_w = 3; %frequency of spindle [Hz]
f_m = f_w*30.5; %frequency of modulation [Hz]
h_0 = A/1.5; %.175 *10^-3; %z-direction velocity [m/rev]
res = .000005; %resolution [m]

tip_geometry_equation  =  @(x)  (-sqrt(3)*x  -  .1*(10^-3))  .*(x<=  -
.025.*(10^-3)*sqrt(3)) ...
            + (-sqrt((.05*(10^-3))^2 - x.^2))    .*(x >-.025*(10^-
3)*sqrt(3)).*(x < .025*(10^-3)*sqrt(3)) ...
            + (sqrt(3)*x -.1*(10^-3))* (x >= .025*(10^-3)*sqrt(3));
%equation of tip geometry (make it have a minimum)


tip_geometry_limits = [-.0001, .0001];  %domain over  which  we  want  to
model tip [m]


%% code


x_vel = (f_w) * pi * d; %velocity in x direction [m/s]
z_vel = (h_0) * f_w; %velocity in z (feed) direction [m/s]
delta_t = min(res / x_vel, res / z_vel); %max time increment allowed to
maintain resolution
x_res_temp = x_vel * delta_t; %temp                               x
resolution
x_units = round(pi * d / x_res_temp); %x_units is the rounded number of
x_res's that can fit in the x direction
x_res = pi * d / x_units; %this is the rounded x_resolution, to allow
for a full x_units in the x direction
z_res_temp = z_vel * delta_t; %temp z resolution [m] -- each increase
in z_res_temp corresponds to increases in time steps
z_units = round(z_length / z_res_temp); %z equivalent of x_units --
each z_unit is the amount that it feeds forward in 1 time step
z_res = z_length / z_units; %z equivalent of x_res


lambda = pi * d * (f_w / f_m);


[z0, minVal] = fminbnd(tip_geometry_equation, tip_geometry_limits(1),
tip_geometry_limits(2)); %finds min value and location of tip function
w_R_units = floor((tip_geometry_limits(2) - z0) / z_res); %number of
subdivisions that 'fit' to right of z0
w_L_units = floor((z0 - tip_geometry_limits(1)) / z_res); %number of
subdivisions that 'fit' to left of z0


tip_geometry(1,:) = [[-w_L_units : -1] [0] [1 : w_R_units]]; %row 1 of
tip geometry is hte number of 'units' width that are on the bit
```

```matlab
%'0' demarcates the point on the bit that first touches the machined
part

temp = 1;
while temp <= max(size(tip_geometry(1,:)))
tip_geometry(2,temp) = tip_geometry_equation(z0 + tip_geometry(1,temp)
* z_res) - minVal;
%row 2 of tip_geometry is the corresponding distance from the outermost
%part of the bit (point '0' above)
temp = temp + 1;
end

plot((tip_geometry(1,:) * z_res) + z0, tip_geometry(2,:)); %plots tip
geometry vs the the width of the bit
xlabel('width [m]'); ylabel('height [m]'); title('tip shape')

%initialize
x_cumulative = 0;
z = -1;
y = zeros(x_units, z_units); %initialize y, starting all heights of
machined piece at '0'
z_feed = 0;

%% loops
while z >= -z_units
    for x = 1 : x_units
        x_cumulative = (x_cumulative + x_res); % [m] this cumulative x
is used as an input into sine wave, so continuous
        for n = 1 : length(tip_geometry) %this loop checks for cutting
that happens on any part of tool bit
            z_temp = z + tip_geometry(1,n); %z is the part of the bit
that touches the part first. z_temp is the surrounding parts of the
tool that correspond with existing data points
            if -z_units <= z_temp && z_temp <= -1 && ... %if z_temp is
still on range of workpiece
                    tip_geometry(2,n) + offset < y(x,-z_temp)    %if
value is less than former value  **note, i flipped the z direction on
this one

                y(x,-z_temp) = tip_geometry(2,n) + offset; %then y(x,z)
has new minimum
            end
        end
            z_feed = z_feed - 1; %
            z = z_feed - round(A*sin(2*pi*x_cumulative/lambda) / z_res)
;  %z is in 'units' so we need to /z_res to change the amplitude (m) to
units
    end
end
```

```matlab
%% plot on plane
figure
subplot(1,2,1)
x_plot = x_res : x_res : x_res * x_units;
z_plot = z_res : z_res : z_res * z_units;
%mesh(z_plot, x_plot, y)

%f = figure('visible','off');

fig = figure; set(fig, 'Visible', 'off');

set(surf(z_plot(1 : end - 1), x_plot, y(1 : end, 1 : end -
1)),'LineStyle','none') %update this so the z direction is flipped
set(gcf,'color','w');
%colorbar


%axis equal

 zlim([-1*10^-3 0])  %height
 xlim([1*10^-4 8*10^-4])  %z
 ylim([0*10^-3 .25*10^-3])  %x

%view(0,90)
xlabel('z [m]')
ylabel('x [m]')
title(['fw=' num2str(f_w) ' fm=' num2str(f_m) ' A=' num2str(A) ' h0='
num2str(h_0)])

c=clock; temp = fix(c);

saveas(fig, [num2str(temp(1)) '_' num2str(temp(2)) '_' num2str(temp(3))
'_' num2str(temp(4)) '_' num2str(temp(5)) '_' num2str(temp(6))
'radial_MAM_plane_surface.tif'],'tif');


A = .05*10^-3; %amplitude [m]
d = 1.5 * 10^-3; %diameter of part [m]
offset = -.0381*10^-3;  % mam device offset (depth of cut) [m]
z_length = .85*10^-3; %z-length of part to be turned [m]
f_w = 3; %frequency of spindle [Hz]
f_m = f_w*30.5; %frequency of modulation [Hz]
h_0 = A/.5; %.175 *10^-3; %z-direction velocity [m/rev]
res = .00001; %resolution [m]



%{
```
121

```matlab
close all
x_cum_prac  = [0:x_res:x_cumulative];
y = (A*sin(2*pi*x_cum_prac/lambda) / z_res_temp);
plot(x_cum_prac,  y*z_)  %%%%%%%%%%%%%%%  i'm  stuck  here.  I  think  the
issue has to do with
%x_res and z_res being differnet. I need to dig through more and think
%to test, keep changing 'res' up top and see how the amplitude changes
%}

%% plot on cylinder
%{
subplot(1,2,2)
theta=0:2*pi/size(y,1):2*pi-2*pi/size(y,1);

x_plot_cylindrical=(d/2)*sin(theta);
x_plot_cylindrical=x_plot_cylindrical'*ones(1,size(y,2));
y_plot_cylindrical=(d/2)*cos(theta);
y_plot_cylindrical=y_plot_cylindrical'*ones(1,size(y,2));
z_plot=ones(size(y,1),1)*z_plot;

% play with the scale parameters to make features more subtle or
evident
scale=40;
for row=1:size(y,1)
    for col=1:size(y,2)

x_plot_cylindrical(row,col)=x_plot_cylindrical(row,col)+scale*y(row,col
)*sin(theta(row));

y_plot_cylindrical(row,col)=y_plot_cylindrical(row,col)+scale*y(row,col
)*cos(theta(row));
    end
end

surf(x_plot_cylindrical,y_plot_cylindrical,z_plot,y,'EdgeColor','none')
;
axis equal
 zlim([.01 .011])
% keyboard
% axis off
%saveas(gcf,'cylindrical_plot.tif','tif');


%}
```

122

REFERENCES

1. Moore, D.F., *A history of research on surface texture effects.* Wear, 1969. **13**(6): p. 381-412.

2. Chang, P.-C., N.P. Lang, and W.V. Giannobile, *Evaluation of Functional Dynamics during Osseointegration and Regeneration Associated with Oral Implants: A Review.* Clinical oral implants research, 2010. **21**(1): p. 1-12.

3. Cooper, L.F., *A role for surface topography in creating and maintaining bone at titanium endosseous implants.* The Journal of Prosthetic Dentistry, 2000. **84**(5): p. 522-534.

4. Gravesen, P., J. Branebjerg, and O.S. Jensen, *Microfluidics-a review.* Journal of Micromechanics and Microengineering, 1993. **3**(4): p. 168.

5. Ziaie, B., et al., *Hard and soft micromachining for BioMEMS: review of techniques and examples of applications in microfluidics and drug delivery.* Advanced Drug Delivery Reviews, 2004. **56**(2): p. 145-172.

6. Kasemo, B., *Biocompatibility of titanium implants: surface science aspects.* J Prosthet Dent, 1983. **49**(6): p. 832-7.

7. Vasconcellos, L.M., et al., *Design of dental implants, influence on the osteogenesis and fixation.* Journal of Materials Science: Materials in Medicine, 2008. **19**(8): p. 2851-2857.

8. Wang, K., *The use of titanium for medical applications in the USA.* Materials Science and Engineering: A, 1996. **213**(1): p. 134-137.

9. Sumner, D.R. and J.O. GALANTE, *Determinants of stress shielding: design versus materials versus interface.* Clinical orthopaedics and related research, 1992. **274**: p. 202-212.

10. Simmons, C.A., N. Valiquette, and R.M. Pilliar, *Osseointegration of sintered porous-surfaced and plasma spray-coated implants: An animal model study of early postimplantation healing response and mechanical stability.* J Biomed Mater Res, 1999. **47**(2): p. 127-38.

11. Le Guéhennec, L., et al., *Surface treatments of titanium dental implants for rapid osseointegration.* Dental Materials, 2007. **23**(7): p. 844-854.

12.   Hoch, H.C., L.W. Jelinski, and H.G. Craighead, *Nanofabrication and Biosystems: Integrating Materials Science, Engineering, and Biology*. 1996: Cambridge University Press.

13.   Borghi, A., et al., *Tribological effects of surface texturing on nitriding steel for high-performance engine applications*. Wear, 2008. **265**(7-8): p. 1046-1051.

14.   Koura, M.M., *The effect of surface texture on friction mechanisms*. Wear, 1980. **63**(1): p. 1-12.

15.   Buscaglia, G.C., I. Ciuperca, and M. Jai, *On the optimization of surface textures for lubricated contacts*. Journal of Mathematical Analysis and Applications, 2007. **335**(2): p. 1309-1327.

16.   Wang, X., et al., *Optimization of the surface texture for silicon carbide sliding in water*. Applied Surface Science, 2006. **253**(3): p. 1282-1286.

17.   Ibatan, T., M.S. Uddin, and M.A.K. Chowdhury, *Recent development on surface texturing in enhancing tribological performance of bearing sliders*. Surface and Coatings Technology, 2015. **272**: p. 102-120.

18.   Huffington, J.D., *The topography of abraded surfaces in relation to contact area and mechanism of abrasion*. Wear, 1980. **58**(1): p. 117-136.

19.   Etsion, I., *State of the Art in Laser Surface Texturing*. Journal of Tribology, 2005. **127**(1): p. 248.

20.   Ryk, G., Y. Kligerman, and I. Etsion, *Experimental Investigation of Laser Surface Texturing for Reciprocating Automotive Components*. Tribology Transactions, 2002. **45**(4): p. 444-449.

21.   Madou, M.J., *Fundamentals of Microfabrication: The Science of Miniaturization, Second Edition*. 2002: Taylor & Francis.

22.   Davis, J.R., *Handbook of thermal spray technology*. 2004: ASM international.

23.   German, R.M., *Sintering theory and practice*. Solar-Terrestrial Physics (Solnechno-zemnaya fizika), 1996: p. 568.

24.   Schey, J., *Introduction to manufacturing processes*. McGraw-Hill Book Co, 1221 Avenue of the Americas, New York, New York 10020, USA, 1987., 1987.

25.   Qin, D., et al., *Microfabrication, microstructures and microsystems*, in *Microsystem technology in chemistry and life science*. 1998, Springer. p. 1-20.

26. Bowers, K.T., et al., *Optimization of surface micromorphology for enhanced osteoblast responses in vitro.* Int J Oral Maxillofac Implants, 1992. **7**(3): p. 302-10.

27. Wennerberg, A., et al., *A histomorphometric evaluation of screw-shaped implants each prepared with two surface roughnesses.* Clin Oral Implants Res, 1998. **9**(1): p. 11-9.

28. Boyan, B.D., et al., *Titanium surface roughness alters responsiveness of MG63 osteoblast-like cells to 1 alpha,25-(OH)2D3.* J Biomed Mater Res, 1998. **39**(1): p. 77-85.

29. Gittens, R.A., et al., *The effects of combined micron-/submicron-scale surface roughness and nanoscale features on cell proliferation and differentiation.* Biomaterials, 2011. **32**(13): p. 3395-3403.

30. Lipski, A.M., et al., *The effect of silica nanoparticle-modified surfaces on cell morphology, cytoskeletal organization and function.* Biomaterials, 2008. **29**(28): p. 3836-3846.

31. Curtis, A., et al., *Cells react to nanoscale order and symmetry in their surroundings.* NanoBioscience, IEEE Transactions on, 2004. **3**(1): p. 61-65.

32. Kovalchenko, A., et al., *The effect of laser surface texturing on transitions in lubrication regimes during unidirectional sliding contact.* Tribology International, 2005. **38**(3): p. 219-225.

33. Boothroyd, G., *Fundamentals of Metal Machining and Machine Tools, Third Edition.* 1988: Taylor & Francis.

34. Oberg, E., et al., *Machinery's handbook.* Vol. 200. 2004: Industrial Press New York.

35. Noiles, D.G., *Metallic prosthetic devices having micro-textured outer surfaces.* 1989, Google Patents.

36. May, D.R., et al., *Apparatus for single-sided, cold mechanical knurling.* 1997, Google Patents.

37. Grewal, N.S. and S.C. Saxena, *Effect of Surface Roughness on Heat Transfer from Horizontal Immersed Tubes in a Fluidized Bed.* Journal of Heat Transfer, 1979. **101**(3): p. 397-403.

38. Coban, H., A.K.M. De Silva, and D.K. Harrison, *Mill-knurling as an alternative to laser welding for automotive drivetrain assembly.* CIRP Annals - Manufacturing Technology, 2009. **58**(1): p. 41-44.

39. Uh, J., et al., *Laser Engraving of Micro-patterns on Roll Surfaces.* ISIJ international, 2002. **42**(11): p. 1266-1272.

40. Bourassa, P.L., S. Yue, and J.D. Bobyn, *The effect of heat treatment on the fatigue strength of microknurled Ti-6Al-4V.* Journal of Biomedical Materials Research, 1997. **37**(2): p. 291-300.

41. Piotter, V., et al., *Injection molding and related techniques for fabrication of microstructures.* Microsystem Technologies, 1997. **3**(3): p. 129-133.

42. Ruprecht, R., et al., *Various replication techniques for manufacturing three-dimensional metal microstructures.* Microsystem Technologies, 1997. **4**(1): p. 28-31.

43. Piotter, V., et al., *Metal and ceramic micro components made by powder injection molding.* Progress in Powder Metallurgy, Pts 1 and 2, 2007. **534-536**: p. 373-376.

44. Wei, Y., et al., *Theoretical and experimental researches of size effect in micro-indentation test.* Science in China Series A: Mathematics. **44**(1): p. 74-82.

45. Pettersson, U. and S. Jacobson, *Tribological texturing of steel surfaces with a novel diamond embossing tool technique.* Tribology International, 2006. **39**(7): p. 695-700.

46. Bhushan, B., *Handbook of Micro/Nano Tribology, Second Edition*. 1998: Taylor & Francis.

47. Usama, M.A. and R.A. Jeffrey, *A review of micro-powder injection moulding as a microfabrication technique.* Journal of Micromechanics and Microengineering, 2011. **21**(4): p. 043001.

48. Yan-qing, W., et al., *Tribological properties of surface dimple-textured by pellet-pressing.* Procedia Earth and Planetary Science, 2009. **1**(1): p. 1513-1518.

49. Wakuda, M., et al., *Effect of surface texturing on friction reduction between ceramic and steel materials under lubricated sliding contact.* Wear, 2003. **254**(3-4): p. 356-363.

50. Meguid, S.A., et al., *Three-dimensional dynamic finite element analysis of shot-peening induced residual stresses.* Finite Elements in Analysis and Design, 1999. **31**(3): p. 179-191.

51. Meguid, S.A., G. Shagal, and J.C. Stranart, *Finite element modelling of shot-peening residual stresses.* Journal of Materials Processing Technology, 1999. **92–93**: p. 401-404.

52. Majzoobi, G.H., R. Azizi, and A. Alavi Nia, *A three-dimensional simulation of shot peening process using multiple shot impacts.* Journal of Materials Processing Technology, 2005. **164–165**: p. 1226-1234.

53. Oliveira, J.F.G., A.C. Bottene, and T.V. França, *A novel dressing technique for texturing of ground surfaces.* CIRP Annals - Manufacturing Technology, 2010. **59**(1): p. 361-364.

54. Graham, E., C. Park, and S. Park, *Fabrication of micro-dimpled surfaces through micro ball end milling.* International Journal of Precision Engineering and Manufacturing, 2013. **14**(9): p. 1637-1646.

55. Masuzawa, T., *State of the Art of Micromachining.* CIRP Annals - Manufacturing Technology, 2000. **49**(2): p. 473-488.

56. Mann, J.B., et al., *Enhancing material removal processes using modulation-assisted machining.* Tribology International, 2011. **44**(10): p. 1225-1235.

57. Mann, J.B., et al., *Metal particulate production by modulation-assisted machining.* Scripta Materialia, 2007. **57**(10): p. 909-912.

58. Schneider, Y.G., *Formation of surfaces with uniform micropatterns on precision machine and instruments parts.* Precision Engineering, 1984. **6**(4): p. 219-225.

59. Hong, M.S. and K.F. Ehmann, *Generation of engineered surfaces by the surface-shaping system.* International Journal of Machine Tools and Manufacture, 1995. **35**(9): p. 1269-1290.

60. Greco, A., et al., *Surface Texturing of Tribological Interfaces Using the Vibromechanical Texturing Method.* Journal of Manufacturing Science and Engineering, 2009. **131**(6): p. 061005.

61. Kurniawan, R. and T.J. Ko, *A study of surface texturing using piezoelectric tool holder actuator on conventional CNC turning.* International Journal of Precision Engineering and Manufacturing, 2013. **14**(2): p. 199-206.

62. Brehl, D.E. and T.A. Dow, *Review of vibration-assisted machining.* Precision Engineering, 2008. **32**(3): p. 153-172.

63. Hench, L.L., *Biomaterials: a forecast for the future.* Biomaterials, 1998. **19**(16): p. 1419-1423.

64. Becker, W., et al., *Osteoporosis and implant failure: an exploratory case-control study.* J Periodontol, 2000. **71**(4): p. 625-31.

65. Brånemark, P.-I., *Osseointegrated implants in the treatment of the edentulous jaw : experience from a 10-year period : a description of a new procedure for rehabilitation of the edentulous patient and a clinical report of 235 jaws in 211 consecutive cases treated during 1965-1975 with installation of 1618 titanium fixtures supporting permanently bone anchored bridges.* 1977, Stockholm: Distributed by Almqvist & Wiksell.

66. Oshida, Y., et al., *Dental Implant Systems.* International Journal of Molecular Sciences, 2010. **11**(4): p. 1580-1678.

67. Hansson, S. and M. Norton, *The relation between surface roughness and interfacial shear strength for bone-anchored implants. A mathematical model.* Journal of Biomechanics. **32**(8): p. 829-836.

68. Wong, M., et al., *Effect of surface topology on the osseointegration of implant materials in trabecular bone.* J Biomed Mater Res, 1995. **29**(12): p. 1567-75.

69. Feighan, J.E., et al., *The influence of surface-blasting on the incorporation of titanium-alloy implants in a rabbit intramedullary model.* J Bone Joint Surg Am, 1995. **77**(9): p. 1380-95.

70. Bianco, P.D., P. Ducheyne, and J.M. Cuckler, *Titanium serum and urine levels in rabbits with a titanium implant in the absence of wear.* Biomaterials, 1996. **17**(20): p. 1937-42.

71. Smith, D.C., et al., *Systemic metal ion levels in dental implant patients.* Int J Oral Maxillofac Implants, 1997. **12**(6): p. 828-34.

72. Becker, W., et al., *A Prospective Multicenter Clinical Trial Comparing One- and Two-Stage Titanium Screw-Shaped Fixtures with One-Stage Plasma-Sprayed Solid-Screw Fixtures.* Clinical Implant Dentistry and Related Research, 2000. **2**(3): p. 159-165.

73. Albrektsson, T. and A. Wennerberg, *The impact of oral implants - past and future, 1966-2042.* J Can Dent Assoc, 2005. **71**(5): p. 327.

74. Eriksson, C., H. Nygren, and K. Ohlson, *Implantation of hydrophilic and hydrophobic titanium discs in rat tibia: cellular reactions on the surfaces during the first 3 weeks in bone.* Biomaterials, 2004. **25**(19): p. 4759-4766.

75. Bornstein, M.M., et al., *Bone apposition around two different sandblasted and acid-etched titanium implant surfaces: a histomorphometric study in canine mandibles.* Clin Oral Implants Res, 2008. **19**(3): p. 233-41.

76. Murray, D., T. Rae, and N. Rushton, *The influence of the surface energy and roughness of implants on bone resorption.* Bone & Joint Journal, 1989. **71-B**(4): p. 632-637.

77. Gittens, R.A., et al., *A review on the wettability of dental implant surfaces II: Biological and clinical aspects.* Acta Biomaterialia, 2014. **10**(7): p. 2907-2918.

78. Frank Schwarz, D.R., Anton Sculean, Thomas Georg, Werner Scherbaum, Jurgen Becker, *Effects of an Er: YAG laser and the Vector ultrasonic system on the biocompatibility of titanium implants in cultures of human osteoblast-like cells.*

79. Vologin, G.A., *METHODS OF THE DENTAL IMPLANT SURFACE MODIFICATION*, in *Guident*. 2014, Guident: Bljnor. p. 31-32,34-36,38-40,42-44.

80. Zhao, G., et al., *Osteoblast-like cells are sensitive to submicron-scale surface structure.* Clin Oral Implants Res, 2006. **17**(3): p. 258-64.

81. Kubo, K., et al., *Cellular behavior on TiO2 nanonodular structures in a micro-to-nanoscale hierarchy model.* Biomaterials, 2009. **30**(29): p. 5319-5329.

82. Michelson, G.K., *Method for forming a spinal implant surface configuration.* 2007, Google Patents.

83. Amrich, M., et al., *Textured surface having undercut micro recesses in a surface.* 2006, Google Patents.

84. Chehroudi, B., T.R. Gould, and D.M. Brunette, *Effects of a grooved epoxy substratum on epithelial cell behavior in vitro and in vivo.* J Biomed Mater Res, 1988. **22**(6): p. 459-73.

85.   Chehroudi, B., T.R. Gould, and D.M. Brunette, *Titanium-coated micromachined grooves of different dimensions affect epithelial and connective-tissue cells differently in vivo.* J Biomed Mater Res, 1990. **24**(9): p. 1203-19.

86.   Drummond, J.F., et al., *A light and scanning electron microscopic evaluation of electro-discharge-compacted porous titanium implants in rabbit tibia.* J Oral Implantol, 1995. **21**(4): p. 295-303.

87.   Dominici, J.T., et al., *An evaluation of electrodischarged prototype implants in rabbit tibia: a preliminary study.* J Oral Implantol, 1994. **20**(4): p. 299-306.

88.   Prakash, C., et al., *Electric discharge machining–A potential choice for surface modification of metallic implants for orthopedic applications: A review.* Proceedings of the Institution of Mechanical Engineers, Part B: Journal of Engineering Manufacture, 2015: p. 0954405415579113.

89.   Jemat, A., et al., *Surface Modifications and Their Effects on Titanium Dental Implants.* BioMed Research International, 2015. **2015**: p. 11.

90.   Stangl, R., et al., *Influence of pores created by laser superfinishing on osseointegration of titanium alloy implants.* Journal of Biomedical Materials Research Part A, 2004. **69A**(3): p. 444-453.

91.   Götz, H.E., et al., *Effect of surface finish on the osseointegration of laser-treated titanium alloy implants.* Biomaterials, 2004. **25**(18): p. 4057-4064.

92.   Klenke, F.M., et al., *Impact of pore size on the vascularization and osseointegration of ceramic bone substitutes in vivo.* Journal of Biomedical Materials Research Part A, 2008. **85A**(3): p. 777-786.

93.   Itälä, A.I., et al., *Pore diameter of more than 100 μm is not requisite for bone ingrowth in rabbits.* Journal of Biomedical Materials Research, 2001. **58**(6): p. 679-683.

94.   Li, J., et al., *Surface-dimpled commercially pure titanium implant and bone ingrowth.* Biomaterials, 1997. **18**(9): p. 691-696.

95.   Mour, M., et al., *Advances in porous biomaterials for dental and orthopaedic applications.* Materials, 2010. **3**(5): p. 2947-2974.

96.   Perez, R.A. and G. Mestres, *Role of pore size and morphology in musculo-skeletal tissue regeneration.* Materials Science and Engineering: C, 2016. **61**: p. 922-939.

97. Mendonca, G., et al., *Advancing dental implant surface technology--from micron-to nanotopography.* Biomaterials, 2008. **29**(28): p. 3822-35.

98. Zinger, O., et al., *Differential regulation of osteoblasts by substrate microstructural features.* Biomaterials, 2005. **26**(14): p. 1837-1847.

99. Levitin, M. and B. Shamshidov, *A laboratory study of friction in hip implants.* Tribotest, 1999. **5**(4): p. 361-369.

100. Zinger, O., et al., *Time-dependent morphology and adhesion of osteoblastic cells on titanium model surfaces featuring scale-resolved topography.* Biomaterials, 2004. **25**(14): p. 2695-2711.

101. Bruzzone, A.A.G., et al., *Advances in engineered surfaces for functional performance.* CIRP Annals - Manufacturing Technology, 2008. **57**(2): p. 750-769.

102. Hutchings, I.M., *Tribology: friction and wear of engineering materials.* 1992.

103. Sasaki, S., *Environmentally friendly tribology (Eco-tribology).* Journal of Mechanical Science and Technology, 2010. **24**(1): p. 67-71.

104. Cai, M., et al., *Lubricating a bright future: Lubrication contribution to energy saving and low carbon emission.* Science China Technological Sciences, 2013. **56**(12): p. 2888-2913.

105. Hamrock, B.J., et al., *Minimum film thickness in elliptical contacts for different regimes of fluid-film lubrication.* 1978: National Aeronautics and Space Administration, Scientific and Technical Information Office.

106. Guangteng, G., P.M. Cann, and H.A. Spikes, *A study of parched lubrication.* Wear, 1992. **153**(1): p. 91-105.

107. Hooke, C.J., *The Elasto-Hydrodynamic Lubrication of Soft, Highly Deformed Contacts Under Conditions of Nonuniform Motion.* Journal of Tribology, 1986. **108**(4): p. 545-550.

108. Kaneta, M., *Effects of Surface Roughness in Elastohydrodynamic Lubrication.* JSME international journal. Ser. 3, Vibration, control engineering, engineering for industry, 1992. **35**(4): p. 535-546.

109. Larsson, R., *Modelling the effect of surface roughness on lubrication in all regimes.* Tribology International, 2009. **42**(4): p. 512-516.

131

110.   Gelinck, E.R.M. and D.J. Schipper, *Calculation of Stribeck curves for line contacts.* Tribology International, 2000. **33**(3–4): p. 175-181.

111.   Lugt, P.M. and G.E. Morales-Espejel, *A Review of Elasto-Hydrodynamic Lubrication Theory.* Tribology Transactions, 2011. **54**(3): p. 470-496.

112.   Shen, C. and M.M. Khonsari, *Texture Shape Optimization for Seal-like Parallel Surfaces: Theory and Experiment.* Tribology Transactions, 2016: p. 1-32.

113.   Hsu, S.M., et al., *Friction reduction using discrete surface textures: principle and design.* Journal of Physics D: Applied Physics, 2014. **47**(33): p. 335307.

114.   Saka, N., M.J. Liou, and N.P. Suh, *The role of tribology in electrical contact phenomena.* Wear, 1984. **100**(1–3): p. 77-105.

115.   Saka, N., H. Tian, and N.P. Suh, *Boundary Lubrication of Undulated Metal Surfaces at Elevated Temperatures.* Tribology Transactions, 1989. **32**(3): p. 389-395.

116.   Tian, H., N. Saka, and N.P. Suh, *Boundary Lubrication Studies on Undulated Titanium Surfaces.* Tribology Transactions, 1989. **32**(3): p. 289-296.

117.   Wang, X., et al., *The effect of laser texturing of SiC surface on the critical load for the transition of water lubrication mode from hydrodynamic to mixed.* Tribology International, 2001. **34**(10): p. 703-711.

118.   Bulatov, V.P., V.A. Krasny, and Y.G. Schneider, *Basics of machining methods to yield wear- and fretting-resistive surfaces, having regular roughness patterns.* Wear, 1997. **208**(1–2): p. 132-137.

119.   Levitin, M. and B. Shamshidov, *A disc‑on‑flat wear test under starved lubrication.* Tribotest, 1997. **4**(2): p. 159-166.

120.   Greco, A., et al., *Rolling Contact Fatigue Performance of Vibro-Mechanical Textured Surfaces.* Tribology Transactions, 2010. **53**(4): p. 610-620.

121.   Gandhi, R., et al., *Surfaces by vibration/modulation-assisted texturing for tribological applications.* The International Journal of Advanced Manufacturing Technology, 2015: p. 1-12.

122.   Mitrofanov, A.V., V.I. Babitsky, and V.V. Silberschmidt, *Finite element simulations of ultrasonically assisted turning.* Computational Materials Science, 2003. **28**(3–4): p. 645-653.

123.   Nath, C. and M. Rahman, *Effect of machining parameters in ultrasonic vibration cutting.* International Journal of Machine Tools and Manufacture, 2008. **48**(9): p. 965-974.

124.   Ding, H., S. Chen, and K. Cheng, *Two-dimensional vibration-assisted micro end milling: cutting force modelling and machining process dynamics.* Proceedings of the Institution of Mechanical Engineers, Part B: Journal of Engineering Manufacture, 2010. **224**(12): p. 1775-1783.

125.   Shen, X.-H., et al., *A study of surface roughness variation in ultrasonic vibration-assisted milling.* The International Journal of Advanced Manufacturing Technology, 2012. **58**(5-8): p. 553-561.

126.   Toews Iii, H.G., W.D. Compton, and S. Chandrasekar, *A Study of the Influence of Superimposed Low-Frequency Modulation on the Drilling Process.* Precision Engineering, 1998. **22**(1): p. 1-9.

127.   Shamoto, E. and T. Moriwaki, *Study on Elliptical Vibration Cutting.* CIRP Annals - Manufacturing Technology, 1994. **43**(1): p. 35-38.

128.   Zhang, C., et al., *Modeling and simulation of micro-groove topography on cylindrical surface by elliptical vibration-assisted turning.* The International Journal of Advanced Manufacturing Technology, 2016: p. 1-18.

129.   Zhiwei, Z., et al., *A novel diamond micro-/nano-machining process for the generation of hierarchical micro-/nano-structures.* Journal of Micromechanics and Microengineering, 2016. **26**(3): p. 035009.

130.   Mann, J.B., et al., *Effects of Controlled Modulation on Interface Tribology and Deformation in Machining.* Tribology Letters, 2009. **35**(3): p. 221-227.

131.   Schubert, A., et al., *Influence of ultrasonic vibration assistance on the surface integrity in turning of the aluminium alloy AA2017*

Beeinflussung der Oberflächenfeingestalt durch Ultraschallüberlagerung beim Drehen der Aluminiumlegierung EN AW-2017. Materialwissenschaft und Werkstofftechnik, 2011. **42**(7): p. 658-665.

132.   Guo, Y., et al., *Enhancing Tool Life in High-Speed Machining of Compacted Graphite Iron (CGI) Using Controlled Modulation.* Tribology Letters, 2012. **47**(1): p. 103-111.

133. Suzuki, H., et al., *Design and implementation of a non-resonant vibration-assisted machining device to create bespoke surface textures.* Proceedings of the Institution of Mechanical Engineers, Part C: Journal of Mechanical Engineering Science, 2016: p. 0954406215625087.

134. Denkena, B., et al., *Efficient machining of microdimples for friction reduction.* Journal of Micro and Nano-Manufacturing, 2013. **1**(1): p. 011003.

135. Zhang, C., et al., *Effects of ultrasonic vibrations in micro-groove turning.* Ultrasonics, 2016. **67**: p. 30-40.

136. Mann, J., et al., *Effects of controlled modulation on surface textures in deep-hole drilling.* SAE Int. J. Mater. Manf, 2013. **6**(1).

137. Gandhi, R., et al., *Surfaces by vibration/modulation-assisted texturing for tribological applications.* The International Journal of Advanced Manufacturing Technology, 2015: p. 1-12.

138. Mann, J.B., C.J. Saldana, and W. Moscoso, *Control systems and methods for machining operations.* 2014, Google Patents.

139. *ISCAR cutting tools.*

140. Norman, J.M., *Understanding the Influence of Parameter Modulation in Machining-based Processing.* 2013: Pennsylvania State University.

141. Yao, C., E.B. Slamovich, and T.J. Webster, *Enhanced osteoblast functions on anodized titanium with nanotube-like structures.* J Biomed Mater Res A, 2008. **85**(1): p. 157-66.

142. Chen, Z.X., et al., *Surface characteristics and in vitro biocompatibility of titanium anodized in a phosphoric acid solution at different voltages.* Biomed Mater, 2009. **4**(6): p. 065003.

143. Lu, Q., A. Simionescu, and N. Vyavahare, *Novel capillary channel fiber scaffolds for guided tissue engineering.* Acta Biomaterialia, 2005. **1**(6): p. 607-614.

144. Matsuzaka, K., et al., *The effect of poly-L-lactic acid with parallel surface micro groove on osteoblast-like cells in vitro.* Biomaterials, 1999. **20**(14): p. 1293-301.

145. Miller, C., et al., *Oriented Schwann cell growth on micropatterned biodegradable polymer substrates.* Biomaterials, 2001. **22**(11): p. 1263-1269.

146. Biggs, M.J., et al., *Interactions with nanoscale topography: adhesion quantification and signal transduction in cells of osteogenic and multipotent lineage.* Journal of Biomedical Materials Research Part A, 2009. **91**(1): p. 195-208.

147. Linez-Bataillon, P., et al., *In vitro MC3T3 osteoblast adhesion with respect to surface roughness of Ti6Al4V substrates.* Biomolecular Engineering, 2002. **19**(2–6): p. 133-141.

148. Degasne, I., et al., *Effects of Roughness, Fibronectin and Vitronectin on Attachment, Spreading, and Proliferation of Human Osteoblast-Like Cells (Saos-2) on Titanium Surfaces.* Calcified Tissue International, 2014. **64**(6): p. 499-507.

149. Yun, K.-D., et al., *Effect of nanotubular-micro-roughened titanium surface on cell response in vitro and osseointegration in vivo.* Materials Science and Engineering: C, 2010. **30**(1): p. 27-33.

150. Kunzler, T.P., et al., *Systematic study of osteoblast and fibroblast response to roughness by means of surface-morphology gradients.* Biomaterials, 2007. **28**(13): p. 2175-2182.

151. Bilezikian, J.P., L.G. Raisz, and T.J. Martin, *Principles of Bone Biology: Two-Volume Set*. 2008: Academic Press.

152. Trisi, P., W. Rao, and A. Rebaudi, *A histometric comparison of smooth and rough titanium implants in human low-density jawbone.* Int J Oral Maxillofac Implants, 1999. **14**(5): p. 689-98.

153. Suzuki, K., K. Aoki, and K. Ohya, *Effects of surface roughness of titanium implants on bone remodeling activity of femur in rabbits.* Bone, 1997. **21**(6): p. 507-514.

154. Grizon, F., et al., *Enhanced bone integration of implants with increased surface roughness: a long term study in the sheep.* Journal of Dentistry, 2002. **30**(5–6): p. 195-203.

155. Deligianni, D.D., et al., *Effect of surface roughness of the titanium alloy Ti–6Al–4V on human bone marrow cell response and on protein adsorption.* Biomaterials, 2001. **22**(11): p. 1241-1251.